University of California
Santa Barbara

O-band QPSK Transmitter and Analog Coherent Receiver for Data Center Links

A dissertation submitted in partial satisfaction
of the requirements for the degree

Doctor of Philosophy
in
Electrical and Computer Engineering

by

Yujie Xia

Committee in charge:

Professor Clint Schow, Chair
Professor James Buckwalter
Professor Larry Coldren
Professor Adel Saleh

December 2022

The Dissertation of Yujie Xia is approved.

Professor James Buckwalter

Professor Larry Coldren

Professor Adel Saleh

Professor Clint Schow, Committee Chair

December 2022

O-band QPSK Transmitter and Analog Coherent Receiver for Data Center Links

by

Yujie Xia

To see a World in a Grain of Sand

And a Heaven in a Wild Flower

Hold Infinity in the palm of your hand

And Eternity in an hour

William Blake, *Auguries of Innocence*

Acknowledgements

Doing a Ph.D. is easy, says no one ever. As for me, I find it to be a particularly challenging and difficult period of my life. However, for this very reason, the experience is truly valuable and impactful, and shapes me into who I am today. I could not have made it through without a lot of people I've been fortunate to interact with.

I would like to thank my advisor, Prof. Clint Schow, for giving me the opportunity to join his group at its early stage, and providing a lively, cooperative working environment. I would like to thank him for his support and patience, especially when things are not going smoothly in the lab. It has been a wonderful experience to see the group growing, empty test benches getting busy, and results coming from assemblies which used to be layouts.

I would also like to thank my other committee members for providing guidance on our project from different aspects and taking time out of their busy schedule to help me with my dissertation and defense. Prof. Jim Buckwalter has always been helping with bridging the gap between the electronic and photonic designers; with a lot of valuable insights from him, we were able to build many assemblies consisting of electronic and photonic chips. Prof. Larry Coldren has a lot of experience in different areas, especially III-V processes. I could always learn a great deal from him not only at the time when I was working in the cleanroom, but also on device design on different platforms. His textbook is also loaded with nice stuff. Prof. Adel Saleh always gives us detailed explanation on network architecture, which is an area that we don't get much exposure to in our regular experiments. With his information, we have a deeper understanding on the big picture of our work and the motivation behind it. Adel is also very knowledgeable in polarization control, and provided a lot of insight in understanding the theory of polarization recovery section.

Being one of the first students in an experimental research lab can be difficult at times, so I would like to thank the people who have given me enormous support at the starting stages of my research activities. Takako, who joined the group before I did, gave me valuable advice from choosing classes to equipment usage in the lab, and also helped a lot with my first tapeout submission. Sarvagya guided me through the simulation and design process of my first tapeout, and Sergio provided a great amount of help with test structure characterization and the process of setting up coherent testing. I would also like to thank my undergrad final year project advisor, Prof. Linjie Zhou, and all the master and Ph.D. students in his group at that time, especially Rui, Yanyang and Minjuan, for introducing me to the wonderful world of integrated photonics. With their guidance and help, I already had some theoretical and experimental knowledge in integrated photonics when joining UCSB and wasn't totally lost.

I would like to thank the fellow graduate students who I work together with on our electronic-photonic integration projects: Luis, Hector and Aaron M. Luis and I worked through a lot of technical details during the lonely and confusing period of COVID shut down, and we managed to demonstrate the first working EIC-PIC coherent receiver in our lab. Hector taught me the skills in different steps of building assemblies, and his wire bonding skills always save the day. Aaron M gave me lots of training on lab equipment covering different aspects, and provided a great amount of support in understanding the coherent system and optimizing the experiment setup. I would also like to thank Yuan, who always shows interests in my measurements and offers valuable and thoughtful suggestions for debugging and optimization; and Steven, for the expertise on general knowledge in coherent testing and scripting.

The time I spent working in the cleanroom was not very long, but it has been an unforgettable learning experience. I am very grateful to many people I worked with during that time: Biljana, who kindly taught all the cleanroom skills to a nervous cleanroom

newbie under tight time limits; Stephen, who has been a trustworthy and competent cleanroom work partner; Demis, who has always been helping us passionately, offering so much wisdom on cleanroom techniques as well as navigating through grad school; Brian T, who took time from his busy schedule to walk us through processing steps; Brian L and Don, who gave me support and encouragement when I felt stressed out; Hongwei, who always shared her experience on every step of processing and all the tips and tricks; and Shamsul, who explained the process flow patiently and guided us through the beginning steps of processing. Also, I would like to thank all other cleanroom staff for keeping the tools up and running: Mike D, Aidan, Tom, Tino, Luis Z, Tony, Bill, Ning, and Mike S. I would also like to thank Fengqiao, Victoria and Fabrizio, who not only have been great cleanroom companions, but also helped me with lab measurements.

I would like to thank other people that I have worked together with: JQ, Xinhong, Viviana, Evan, Aaron W, Ghazal and Amalu. Thanks for giving me suggestions in the lab and bringing so much positive vibe, making the lab and the office fun places to work at. And I would like to thank so many people that I interacted with who have helped and supported me: Paolo, Diya, Olga, Bowen, Simone, Navid, Mitra, Paul V, Michael, Panpan, Hongjian, Jianfeng, Tyler, Brandon, Joe, Takahiro, Weiqiang, Kaiyin, Andy N, Lei, Ke... I'm very grateful for your help in different aspects of my grad school journey and your friendship.

In addition to fellow students and postdocs, collaborators in the industry have also offered much help and support through the whole process of design and measurement. I would like to thank Roshi, Guomin, Adam, Bruce and Aaron Z at Rockley Photonics, and Andy S at GlobalFoundries, for discussions and support on design, measurement and debugging.

I would like to thank Val, Amanda, Paul G and Chris, who did a lot of hard work so that we can have less things to worry about as grad students; and Alethea, who always

managed to finish my weird wire bonding requests successfully.

In addition, I would like to thank Dr. Dias and Dr. Rainer at UCSB CAPS for helping me through difficult times. I would also like to thank my violin teacher Valerie for creating happiness through music and adding vibrant color to my life as an engineering graduate student. With their help and support outside of the lab, I always gained the energy and courage to get back into it.

Last but not the least, I'm deeply in debt to my family. I would like to thank my parents for putting up with my mental breakdowns, having faith in me when I didn't, and reassuring me that I still have a home to go back to even if everything fails. You have always been asking me when I would be able to go back and visit, and I hope that I can have an answer soon. And I would like to thank my cousins for rooting for me from two different continents by sharing music, memes, and updates on pets.

It's impossible to thank all the people that have helped me in this journey, and I certainly have not made it here all by myself. I hope that I have also helped some people at a certain point; and that I can pass on the help and support that has been given to me.

Curriculum Vitæ

Yujie Xia

Education

2022	Ph.D. in Electrical and Computer Engineering (Expected), University of California, Santa Barbara.
2018	M.S. in Electrical and Computer Engineering, University of California, Santa Barbara.
2016	B.S. in Electronic Science and Technology, Shanghai Jiao Tong University.

Publications

1. L. A. Valenzuela, **Xia, Yujie**, A. Maharry, H. Andrade, C. L. Schow, and J. F. Buckwalter, *A 50-gbaud qpsk optical receiver with a phase/frequency detector for energy-efficient intra-data center interconnects*, *IEEE Open Journal of the Solid-State Circuits Society* **2** (2022) 50–60
2. **Xia, Yujie**, L. Valenzuela, A. Maharry, S. Pinna, S. Dwivedi, T. Hirokawa, J. Buckwalter, and C. Schow, *A fully integrated o-band coherent optical receiver operating up to 80 gb/s*, in *2021 IEEE Photonics Conference (IPC)*, pp. 1–2, 2021
3. H. Andrade, **Xia, Yujie**, A. Maharry, L. Valenzuela, J. F. Buckwalter, and C. L. Schow, *50 gbaud qpsk 0.98 pj/bit receiver in 45 nm cmos and 90 nm silicon photonics*, in *2021 European Conference on Optical Communication (ECOC)*, pp. 1–4, 2021
4. T. Hirokawa, S. Pinna, N. Hosseinzadeh, A. Maharry, H. Andrade, J. Liu, T. Meissner, S. Misak, G. Movaghar, L. A. Valenzuela, **Xia, Yujie**, S. Bhat, F. Gambini, J. Klamkin, A. A. M. Saleh, L. Coldren, J. F. Buckwalter, and C. L. Schow, *Analog coherent detection for energy efficient intra-data center links at 200 gbps per wavelength*, *Journal of Lightwave Technology* **39** (2021), no. 2 520–531
5. A. S. P. Khope, M. Saeidi, R. Yu, X. Wu, A. M. Netherton, Y. Liu, Z. Zhang, **Yujie Xia**, G. Fleeman, A. Spott, S. Pinna, C. Schow, R. Helkey, L. Theogarajan, R. C. Alferness, A. A. M. Saleh, and J. E. Bowers, *Multi-wavelength selective crossbar switch*, *Opt. Express* **27** (Feb, 2019) 5203–5216
6. A. S. P. Khope, T. Hirokawa, A. M. Netherton, M. Saeidi, **Yujie Xia**, N. Volet, C. Schow, R. Helkey, L. Theogarajan, A. A. M. Saleh, J. E. Bowers, and R. C. Alferness, *On-chip wavelength locking for photonic switches*, *Opt. Lett.* **42** (Dec, 2017) 4934–4937
7. Y. Zhong, L. Zhou, Y. Zhou, **Yujie Xia**, S. Liu, L. Lu, J. Chen, and X. Wang, *Microwave frequency upconversion employing a coupling-modulated ring resonator*, *Photon. Res.* **5** (Dec, 2017) 689–694

8. Y. Zhong, L. Zhou, Y. Zhou, **Yujie Xia**, M. Wang, and J. Chen, *Microwave frequency-doubling based on a coupling-modulated silicon ring resonator*, in *Conference on Lasers and Electro-Optics*, p. SM1O.8, Optica Publishing Group, 2017
9. L. Zhou, Y. Zhou, M. Wang, Y. Zhong, **Yujie Xia**, and J. Chen, *Microwave signal processing using high speed silicon optical modulators*, in *Asia Communications and Photonics Conference 2016*, p. AS2E.2, Optica Publishing Group, 2016
10. Y. Zhou, L. Zhou, M. Wang, **Xia, Yujie**, Y. Zhong, X. Li, and J. Chen, *Linearity characterization of a dualparallel silicon machzehnder modulator*, *IEEE Photonics Journal* **8** (2016), no. 6 1–8

Abstract

O-band QPSK Transmitter and Analog Coherent Receiver for Data Center Links

by

Yujie Xia

Data centers around the globe are hosting many applications and services that are increasingly integrated into everyday lives. As data center traffic continues to grow, there is a great demand for high-speed, scalable, and power efficient intra-data center links. With scalability on multiple dimensions, higher spectral efficiency, and improved sensitivity compared with its intensity-modulation and direct detection (IM-DD) counterpart, coherent technology is a promising solution for intra-data center links ($<$ 2km). Conventional coherent links based on digital signal processing (DSP) require high sampling rate analog-to-digital converters (ADC), significantly degrading energy efficiency. An analog coherent scheme performs carrier recovery and phase detection functions using an electronic integrated circuit (EIC) to implement an optical phase locked loop (OPLL) that provides carrier frequency and phase tracking, thereby, eliminating the need for ADCs and improving the energy efficiency.

The focus of this work is to develop high speed O-band QPSK transmitter and coherent receivers to be integrated with energy efficient EICs. O-band QPSK coherent receivers consisting of custom EICs and coherent optical front-end photonic integrated circuit (PIC) fabricated in two different silicon photonic (SiP) platforms are demonstrated at 100 Gb/s per polarization. An EAM-based QPSK transmitter with custom EIC driver is also presented with up to 64 Gb/s operation below SD-FEC BER limit. In addition, QPSK coherent link performance with the EAM-based transmitter and one of the custom EIC-PIC receivers is characterized, showing operation up to 64 Gb/s below

SD-FEC BER limit. Discussions on polarization recovery and pros and cons of different photonic technology for data center application are also provided.

Contents

Chapter 1

Introduction

1.1 History of Coherent Optical Systems

The research and development in optical fiber communication systems started in the first half of the 1970s. Such a system utilizes an electrical bit stream to modulate the intensity of the optical carrier inside the optical transmitter, and the transmitter signal is detected by a square-law detector. Such a scheme is referred to as intensity modulation with direct detection (IM/DD). An alternative scheme, well known in the context of radio and microwave communication systems, transmits information by modulating the frequency or the phase of the optical carrier and detects the transmitted signal by using homodyne or heterodyne detection techniques. Since phase coherence plays an important role in such schemes, such communication systems are called coherent systems.

Coherent optical communication systems have attracted a lot of research interest in the 1970s-1980s. Research activities on different aspects of the coherent optical system have been conducted.

For the IM/DD scheme, the signal is detected simply by a photodiode, which converts the optical power into photocurrent. The process can be expressed by

$$I \propto E_S \cdot E_S^* = (A_S \exp(-j(\omega_0 t + \phi_S)))(A_S \exp(j(\omega_0 t + \phi_S))) = A_S^2 \tag{1.1}$$

where

$$E_S = A_S \exp[-j(\omega_0 t + \phi_S)] \tag{1.2}$$

It can be seen that the phase information of the signal is completely lost in the IM/DD scheme. A technique to solve this problem is to measure not the absolute phase, but the phase relative to a known reference signal. That is where a local oscillator (LO) is introduced, which in general is a continuous-wave (CW) narrow linewidth laser. The schematic of coherent detection is shown in Fig. 1.1 and the mixing of the signal and LO can be observed.

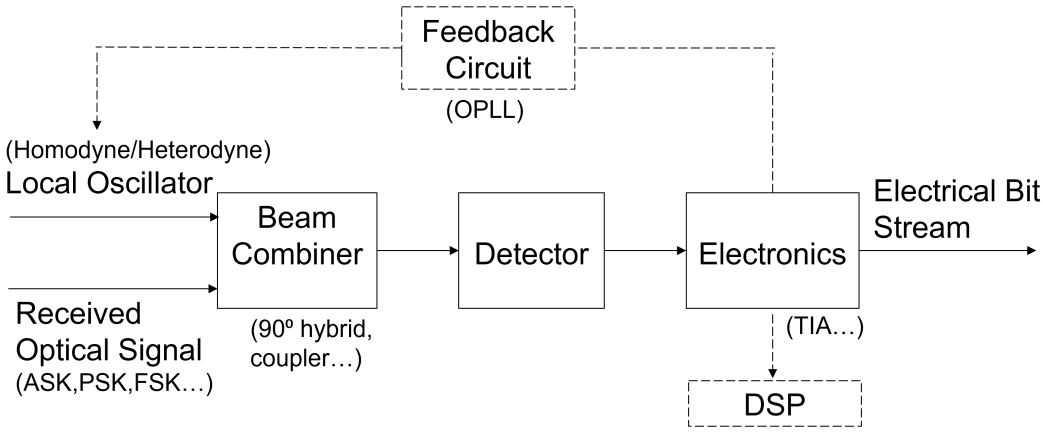

Figure 1.1: Schematic of coherent detection

In order to see the result of mixing the signal and LO, we can start the derivation by expressing the signal as

$$E_S = A_S \exp[-j(\omega_0 t + \phi_S)] \tag{1.3}$$

where ω_0, A_S and ϕ_S are the carrier frequency, amplitude, and phase, respectively;

and the LO as

$$E_{LO} = A_{LO} \exp[-j(\omega_{LO}t + \phi_{LO})] \tag{1.4}$$

where ω_{LO}, A_{LO} and ϕ_{LO} are the frequency, amplitude, and phase of the LO, respectively. Since the photocurrent is proportional to the optical power, it can be expressed as

$$I \propto (E_S + E_{LO})(E_S + E_{LO})^* = A_S^2 + A_{LO}^2 + 2A_S A_{LO} cos(\Delta\omega t + \Delta\phi) \tag{1.5}$$

where $\Delta\omega = \omega_0 - \omega_{LO}$ and $\Delta\phi = \phi_S - \phi_{LO}$

In this way, the phase information is shown explicitly in the equation. The frequency associated with $\Delta\omega$ is the intermediate frequency: $\nu_{IF} = \Delta\omega/2\pi$. When the ω_{LO} is chosen to be equal to ω_0 so that $\omega_{IF} = 0$, the beating of the signal and the LO is called a homodyne scheme. Otherwise, the ω_{LO} can be chosen to differ from ω_0 such that ν_{IF} is in the microwave region, and this is referred to as the heterodyne scheme.

In this stage of research activities, the primary motivation for developing coherent optical communication systems is the improved receiver sensitivity. As can be seen in the time-varying part of Eq. 1.5, the A_{LO} can be chosen so that $A_{LO} \gg A_S$. In this way, the LO can amplify the receiver signal by a large factor. According to the derivation in [1], the power of the LO can be controlled at the receiver and be made large enough so that the receiver noise is dominated by shot noise. The receiver sensitivity can be improved by up to 20 dB compared with that of IM/DD systems.

The homodyne scheme has a couple of advantages over the heterodyne scheme. In homodyne receivers, the baseband signal is directly obtained, unlike the heterodyne receivers which require an intermediate frequency. And in terms of sensitivity improvement, the SNR improvement of homodyne scheme is higher by a factor of 2 compared with the

heterodyne scheme. However, homodyne demonstration is more difficult than heterodyne since the linewidth requirement is the most stringent for homodyne receivers.

Research activities have been conducted on the system level of coherent scheme. In [2], a frequency-division multiplexing heterodyne scheme is discussed, and calculation and derivation for frequency modulation format is provided. Although homodyne receivers are more difficult to implement, there have also been a lot of research activities centered around it. For example, in [3], the authors focused on developing broad bandwidth Costas loops to relax the linewidth requirement of lasers in the homodyne application.

The demonstrations above were accomplished using discrete optical components, which lead to complexity and reliability issues. For this reason, there have also been many research activities focusing on the integration of different required components such as lasers, optical hybrids, and photodetectors. Integration of a DFB laser as the LO laser, a direction coupler, and photodetectors is shown in [4], and preliminary experiment result of optical heterodyne detection is presented, with a beat note being generated. The first integrated heterodyne receiver PIC capable of actual heterodyne data reception is claimed in [5], where system performance is demonstrated with FSK modulation format. Similar to [4], the device integrates a MQW-DBR laser, a directional coupler, and balanced photodetectors. An integrated optical front-end for balanced, polarization-diversity coherent lightwave reception is presented in [6], where waveguides, MMIs and dual polarization selective coupler/PD pairs are integrated. Device characterization results such as loss and polarization dependence are presented, but no data transmission and detection are demonstrated. All those devices are fabricated on InP platform and designed for C-band operation.

The early stage of the development of coherent optical systems were targeted for long-haul transmission, as can be seen in the demonstrations in [7] and [8].

In the 1990s, the invention of erbium-doped fiber amplifiers (EDFAs) made the shot-

noise-limited receiver sensitivity of the coherent receiver less significant. The rapid advance in high-capacity wavelength-division multiplexing (WDM) technology also increased the transmission capacity. The combination of these two offered great capacity increase for IM/DD systems. Since coherent systems also have more technical difficulties to overcome compared with IM/DD systems, further research and development in coherent optical system was essentially paused for almost 20 years.

1.2 Recent Development on Coherent Optical Systems

As the demand for transmission capacity continued to increase, the research activities on coherent optical technology have restarted in recent years, but this time the motivation has shifted to scalability and spectral efficiency. By using complex modulation formats and encoding more bits in one symbol, the data rate can be increased while keeping the occupied optical bandwidth constant. This technique increases the spectral efficiency and thus the transmission capacity. Detailed analysis is provided in [9], showing that coherent reception offers increased spectral efficiency compared with IM/DD. The research activity that triggered the revival of interest in coherent optical communication is the demonstration in [10], where differential quadrature phase-shift keying (DQPSK) transmission and detection is demonstrated using discrete components. Since then, increasing research activities have been conducted to explore the application of the coherent scheme, while utilizing the advantages of integration at the same time. At this point, with the onset of research on silicon photonics platform [11], there are more material and platform options for different application requirements and settings.

A monolithic InP dual-pol QPSK coherent receiver has been demonstrated, where

polarization splitters, 90-degree hybrids, and balanced PDs are integrated on InP. The system level measurement is done with two C-band external cavity lasers (ECL) for signal and LO, and the system operates up to 112 Gb/s data rate [12]. Monolithic coherent receiver has also been demonstrated on silicon photonics platform. In [13], dual-pol integrated coherent receiver shows operation at 43 and 112 Gb/s. Two polarization beam splitters (PBS), two 90-degree hybrids, and four pairs of balanced germanium PDs are integrated on one chip, and the demonstration is done using two C-band ECLs for the signal and LO.

In addition to system level integration and characterization, much effort has been put into developing individual devices needed in coherent systems for better overall performance. For example, one of the key components in the QPSK coherent receiver is the 90-degree hybrid. There are two major types of 90-degree hybrids: one type is based on a combination of components such as 3-dB couplers and phase shifters, and the other type is based on 4×4 multimode interference (MMI) couplers. In [14], the authors propose a novel design of the first type of 90-degree hybrid. The topology of the layout enables the functionality of 90-degree hybrid with purely passive components, which means phase shifters are not needed, and the device turns out to be very compact. In [15], the authors show a 90-degree hybrid design with a 2×4 MMI based on paired interference combined with a phase shifter and a 2×2 MMI, so that waveguide crossings needed for a typical 4×4 MMI can be eliminated, and loss and crosstalk can be reduced. In [16], the authors take one step further and demonstrate a 90-degree hybrid based on a linear-tapered 2×4 MMI and a 2×2 MMI coupler, where the phase shifter can also be removed when designed properly. The design does not require waveguide crossings and is even more compact compared with [15].

The availability of high-speed DSP also contributed to the renewal of interest in coherent technology. The concept of DSP utilization was already discussed in the 1990s

[17]. Because of the difficulty in OPLL realization as well as the stringent linewidth requirement for homodyne detection, using DSP algorithms for phase recovery can be an intuitive way to avoid those difficulties. Several demonstrations of long-haul transmission with homodyne detection came out around the year 2000. For example, in [18], the authors demonstrated 210 km 20 Gb/s QPSK transmission with digital signal processing for phase estimation. DSP also offers possibilities for the compensation of additional impairments such as polarization mode dispersion and inter symbol interference (ISI), therefore, digital coherent receivers are widely used in long-haul applications.

1.3 Research Activities on Coherent Technology for Data Center Applications

The concept of the data center first appeared in mid 1950. Since then, data centers have continued to shrink in size and scale up in capacity. The appearance of the internet gave rise to global interconnection, and smart phones and social network apps further increase the data traffic dramatically. All these applications and services are hosted by data centers around the globe. Initially, most of the connections performed in a data center were based on copper links dues to their low price. However, copper induces large losses and distortions, and optical technologies started to be utilized in data centers to overcome those limitations.

Fig. 1.2 shows the cloud data center traffic growth from 2016 to 2021. The growth trend is going to continue in to 2022 and the years after. Fig. 1.3 shows the data center traffic by destination in 2021. The data traffic inside the data center is much greater than that between the user and the data center. Together with the increasing data volume, it shows that it is vital to develop an intra-data center link technology that is scalable,

high-speed, and energy efficient.

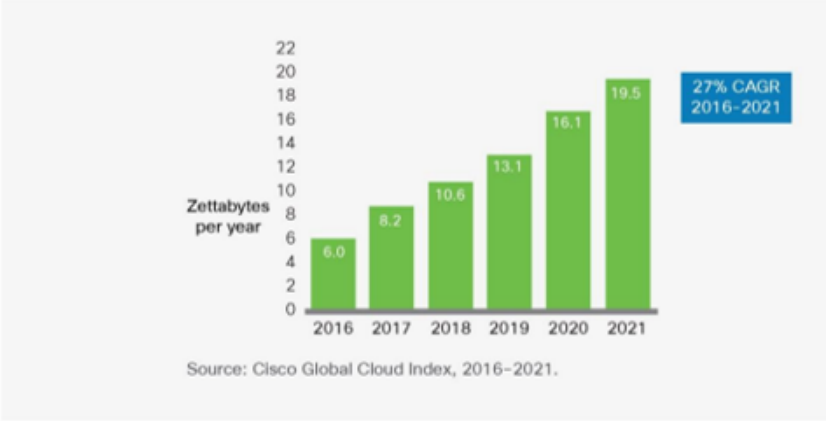

Figure 1.2: Cloud data center traffic growth

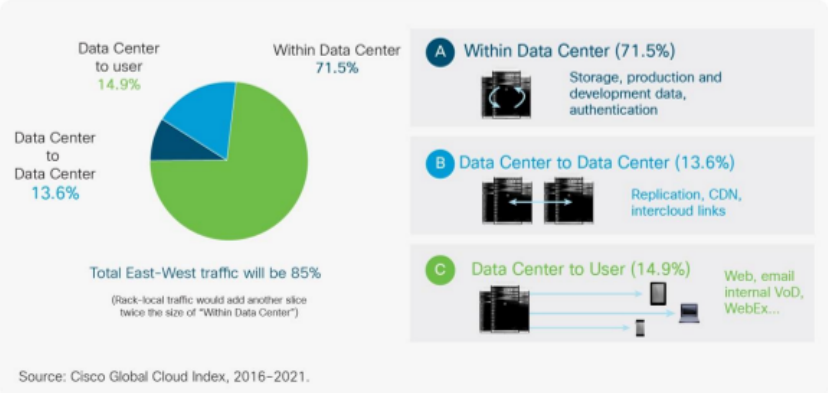

Figure 1.3: Global data center traffic by destination in 2021

As mentioned previously, there have been significant research activities on coherent technology applied to long-haul systems. At the same time, the bandwidth efficiency advantage of coherent technology also makes it beneficial in data center applications. Also, while a couple of demonstrations of IM/DD links operating above 200 Gb/s have been made [19], the IM/DD technique faces the fundamental challenge that it only utilizes the amplitude dimension, which can be a limiting factor for scaling up the data rate. For this reason, alternative solutions including coherent techniques are being explored to

meet the increasing data rate demands of data center interconnects.

Intra-data center links with up to 10 km reach typically operate near 1310 nm to minimize chromatic dispersion (CD), and research activities on O-band coherent systems have started to emerge during recent years. Coherent modulator and receiver that work from 1260 to 1630 nm based on Si photonics are presented in [20], and 200 Gb/s QPSK transmission and long-range optical coherence tomography have been demonstrated. In [21], the authors claim the first performance evaluation of a monolithic silicon-based coherent O-band receiver in a fiber transmission. The receiver consists of a 90-degree hybrid based on 4 × 4 MMI, photodetectors, and an EIC receiver. The recorded data is processed with software using standard DSP algorithms, and QPSK detection up to 56 GBaud is achieved.

1.4 Limitations of DSP and Advantages of QPSK Analog Coherent in Intra-Data Center Links

Although DSP technologies played an important role in the revival of the research activities on coherent optical systems, and digital coherent detection became a mature technology in long-haul systems, it may be less suitable for data center links. Data center applications have different priorities, such as cost, power consumption, and port density. Also, they face fewer propagation impairments, as PMD and nonlinearities are negligible [22].

Analog coherent technology, on the other hand, can offer a significant power saving advantage for data center links. Much of the complexity of traditional coherent DSP can be removed from data center application because it has fewer fiber impairments, and for this reason, the biggest power savings offered by analog coherent arises not

from eliminating DSP, but from removing the linear RX frontends and analog to digital converters (ADCs) [23]. In [24], the power consumption of ADCs based on a couple of different modulation formats and technologies are provided. The power consumption is at least 165 mW per ADC for 112 Gb/s DP-16QAM transmission. The two polarizations each needs two ADCs, so four ADCs are needed in total, and the power consumption is higher than 5 pJ/bit.

Since coherent technology can utilize the phase, frequency and polarization of the signal in addition to amplitude, many modulation formats have been employed over the years. Some of the most commonly utilized formats are quadrature phase shift keying (QPSK), and quadrature amplitude modulation (QAM), such as 16-QAM. Fig. 1.4 shows constellation diagrams of QPSK and 16-QAM. All constellation points on the QPSK modulation format have the same amplitude, whereas 16-QAM incorporates both phase and amplitude modulation.

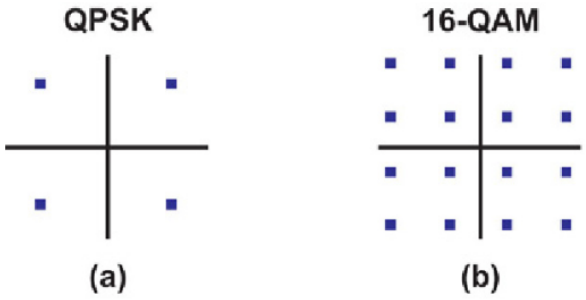

Figure 1.4: Constellation diagrams of QPSK and 16-QAM

It can be seen from the QPSK constellation diagram that when the I and Q signals are separated at the optical front end, unlike 16-QAM modulation format, the electronics only need to make a binary decision. For this reason, low-power electronics using limiting amplifiers can be used and there is no need for A/D conversion required for higher QAM modulation formats, which have multiple decision thresholds. With QPSK-based analog coherent technology, we have demonstrated receiver power consumption as low as 1pJ/bit,

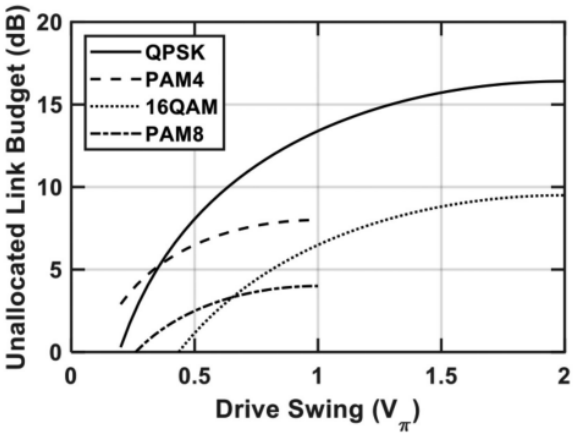

Figure 1.5: Comparison of unallocated link budget

which is discussed in Chapter 4.

Another advantage of the QPSK modulation format is that it increases unallocated link budget. A comparison of unallocated link budget at different modulation drive swing levels for QPSK, PAM4, 16QAM and PAM8 based on the same link assumption is offered by [23], as shown in Fig. 1.5. The analysis shows that QPSK modulation format offers an increased unallocated link budget at a reasonable modulator drive swing ($< V_\pi$) compared with IM/DD and higher order QAM. The higher unallocated link budget can help to enable optical switching in data center applications, and it also increases the system robustness by making the system less sensitive to loss while allowing the laser and driver to operate at lower power.

1.5 Dissertation Outline

The work discussed in the dissertation targets 200 Gbps/λ operation with dual-pol QPSK at 56 GBaud. Towards this goal, the work demonstrates transmitter integrated with driver, and photonic receiver (RX) frontends integrated with electronics RX. There is no on-chip laser and OPLL demonstration in the work discussed in the dissertation,

but that is part of the goal in the future.

In this first chapter the dissertation has given a brief overview of research activities on coherent optical systems and their potential application in data center links. The challenges faced by digital coherent systems in data center application are analyzed, and O-band analog coherent links based on QPSK modulation format and limiting electronics is proposed as an energy saving solution. Along the dissertation, transmitter and receivers based on different silicon photonics platforms with EICs integrated on the same PCB are explored.

In Chapter 2, the process of obtaining a constellation diagram from the measurement setup and calculating the BER is explained in detail. Chapter 3 provides a demonstration of a coherent receiver fabricated in GlobalFoundries 90WG platform, and two EIC-PIC integrated receivers based on two different EIC designs are built and characterized in system level measurements. Chapter 4 discusses a coherent receiver based on a unique silicon photonics platform developed by Rockley Photonics, and its performance is again characterized with EIC integration. In Chapter 5, an EAM-based QPSK modulator integrated with EIC driver is demonstrated, and link measurement with transmitter and receiver based on Rockley Photonics platform is accomplished. Chapter 6 provides a summary of the work covered in the previous chapters and gives some discussions on future work based on some challenges and thoughts encountered in the process of hardware characterization.

Bibliography

[1] G. P.Agrawal, *Chapter 10 - coherent lightwave systems*, in *Fiber-Optic Communication Systems (Third Edition)*, pp. 478–517. John Wiley Sons, Inc., third edition ed., 2002.

[2] O. DeLange, *Wide-band optical communication systems: Part iifrequency-division multiplexing*, *Proceedings of the IEEE* **58** (1970), no. 10 1683–1690.

[3] S. Norimatsu, K. Iwashita, and K. Sato, *Psk optical homodyne detection using external cavity laser diodes in costas loop*, *IEEE Photonics Technology Letters* **2** (1990), no. 5 374–376.

[4] H. Takeuchi, K. Kasaya, Y. Kondo, H. Yasaka, K. Oe, and Y. Imamura, *Monolithic integrated coherent receiver on inp substrate*, *IEEE Photonics Technology Letters* **1** (1989), no. 11 398–400.

[5] T. Koch, U. Koren, R. Gnall, F. Choa, F. Hernandez-Gil, C. Burrus, M. Young, M. Oron, and B. Miller, *Gainas/gainasp multiple-quantum-well integrated heterodyne receiver*, *Electronics Letters* **24** (1989), no. 25 1621–1623.

[6] R. Deri, E. Pennings, A. Scherer, A. Gozdz, C. Caneau, N. Andreadakis, V. Shah, L. Curtis, R. Hawkins, J. Soole, and J.-I. Song, *Ultracompact monolithic*

integration of balanced, polarization diversity photodetectors for coherent lightwave receivers, *IEEE Photonics Technology Letters* **4** (1992), no. 11 1238–1240.

[7] M. Brain, M. Creaner, R. Steele, N. Walker, G. Walker, J. Mellis, S. Al-Chalabi, J. Davidson, M. Rutherford, and I. Sturgess, *Progress towards the field deployment of coherent optical fiber systems*, *Journal of Lightwave Technology* **8** (1990), no. 3 423–437.

[8] Y. Park, J.-M. Delavaux, R. Tench, and T. Cline, *1.7 gb/s-419 km transmission experiment using a shelf-mounted fsk coherent system and packaged fiber amplifier modules*, *IEEE Photonics Technology Letters* **2** (1990), no. 12 917–919.

[9] J. Kahn and K.-P. Ho, *Spectral efficiency limits and modulation/detection techniques for dwdm systems*, *IEEE Journal of Selected Topics in Quantum Electronics* **10** (2004), no. 2 259–272.

[10] R. Griffin and A. Carter, *Optical differential quadrature phase-shift key (odqpsk) for high capacity optical transmission*, in *Optical Fiber Communications Conference*, p. WX6, Optica Publishing Group, 2002.

[11] R. Soref, *The past, present, and future of silicon photonics*, *IEEE Journal of Selected Topics in Quantum Electronics* **12** (2006), no. 6 1678–1687.

[12] C. R. Doerr, L. Zhang, P. J. Winzer, N. Weimann, V. Houtsma, T.-C. Hu, N. J. Sauer, L. L. Buhl, D. T. Neilson, S. Chandrasekhar, and Y. K. Chen, *Monolithic inp dual-polarization and dual-quadrature coherent receiver*, *IEEE Photonics Technology Letters* **23** (2011), no. 11 694–696.

[13] C. R. Doerr, P. J. Winzer, Y.-K. Chen, S. Chandrasekhar, M. S. Rasras, L. Chen, T.-Y. Liow, K.-W. Ang, and G.-Q. Lo, *Monolithic polarization and phase diversity*

coherent receiver in silicon, *Journal of Lightwave Technology* **28** (2010), no. 4 520–525.

[14] H. Guan, Y. Ma, R. Shi, X. Zhu, R. Younce, Y. Chen, J. Roman, N. Ophir, Y. Liu, R. Ding, T. Baehr-Jones, K. Bergman, and M. Hochberg, *Compact and low loss 90° optical hybrid on a silicon-on-insulator platform*, *Opt. Express* **25** (Nov, 2017) 28957–28968.

[15] S.-H. Jeong and K. Morito, *Optical 90° hybrid with broad operating bandwidth of 94 nm*, *Optics letters* **34** (2009), no. 22 3505–3507.

[16] S.-H. Jeong and K. Morito, *Compact optical 90° hybrid employing a tapered 2× 4 mmi coupler serially connected by a 2× 2 mmi coupler*, *Optics Express* **18** (2010), no. 5 4275–4288.

[17] F. Derr, *Coherent optical qpsk intradyne system: concept and digital receiver realization*, *Journal of Lightwave Technology* **10** (1992), no. 9 1290–1296.

[18] D.-S. Ly-Gagnon, K. Katoh, and K. Kikuchi, *Unrepeated 210-km transmission with coherent detection and digital signal processing of 20-gb/s qpsk signal*, in *OFC/NFOEC Technical Digest. Optical Fiber Communication Conference, 2005.*, vol. 2, pp. 3 pp. Vol. 2–, 2005.

[19] X. Pang, O. Ozolins, R. Lin, L. Zhang, A. Udalcovs, L. Xue, R. Schatz, U. Westergren, S. Xiao, W. Hu, G. Jacobsen, S. Popov, and J. Chen, *200 gbps/lane im/dd technologies for short reach optical interconnects*, *Journal of Lightwave Technology* **38** (2020), no. 2 492–503.

[20] C. Doerr, L. Chen, T. Nielsen, R. Aroca, L. Chen, M. Banaee, S. Azemati, G. McBrien, S. Y. Park, J. Geyer, B. Guan, B. Mikkelsen, C. Rasmussen,

M. Givehchi, Z. Wang, B. Potsaid, H. C. Lee, E. Swanson, and J. G. Fujimoto, *O, e, s, c, and l band silicon photonics coherent modulator/receiver*, in *Optical Fiber Communication Conference Postdeadline Papers*, p. Th5C.4, Optica Publishing Group, 2016.

[21] P. M. Seiler, A. Peczek, G. Winzer, K. Voigt, S. Lischke, A. Fatemi, and L. Zimmermann, *56 gbaud o-band transmission using a photonic bicmos coherent receiver*, in *2020 European Conference on Optical Communications (ECOC)*, pp. 1–4, 2020.

[22] J. K. Perin, A. Shastri, and J. M. Kahn, *Design of low-power dsp-free coherent receivers for data center links*, *Journal of Lightwave Technology* **35** (2017), no. 21 4650–4662.

[23] T. Hirokawa, S. Pinna, N. Hosseinzadeh, A. Maharry, H. Andrade, J. Liu, T. Meissner, S. Misak, G. Movaghar, L. A. Valenzuela, Y. Xia, S. Bhat, F. Gambini, J. Klamkin, A. A. M. Saleh, L. Coldren, J. F. Buckwalter, and C. L. Schow, *Analog coherent detection for energy efficient intra-data center links at 200 gbps per wavelength*, *Journal of Lightwave Technology* **39** (2021), no. 2 520–531.

[24] K. Sun, G. Wang, Q. Zhang, S. Elahmadi, and P. Gui, *A 56-gs/s 8-bit time-interleaved adc with enob and bw enhancement techniques in 28-nm cmos*, *IEEE Journal of Solid-State Circuits* **54** (2019), no. 3 821–833.

Chapter 2

Developing the Coherent Measurement Setup

In this chapter, details on the coherent measurement setup as well as the script for equipment control and data presentation will be discussed. All the transmitters and receivers presented in the dissertation are characterized based on this procedure, with some modifications being made for each particular case. Since the fabrication processes mentioned in this dissertation do not have on-chip laser integration for silicon photonics platform, we choose self-homodyne method, meaning the same laser source is used as signal laser and LO laser.

2.1 General Measurement Setup

Fig. 2.1 shows a general coherent measurement setup. The setup can be used to measure transmitter as well as receiver, and the other component needs to have high performance to be used as a reference. As mentioned before, the laser is split into signal and LO path. The signal path goes into a QPSK modulator, which is modulated by two

streams of PRBS signal coming from a bit pattern generator decorrelated by bit delay. Then the signal can be amplified if necessary, and goes into the signal port of the receiver. The other part of the laser power goes into the LO port of the receiver. Then the data from the output of the receiver gets captured by a real-time oscilloscope, which then can be plotted and presented in different ways.

Variations can be made based on the general setup for different devices and measurement requirements. For example, the splitting ratio of the laser can be adjusted, as well as the level of amplification from the SOA. As for the fiber connections, one option is to use polarization maintaining (PM) equipment and fibers for the whole setup, otherwise polarization controllers (PCs) will be needed when necessary.

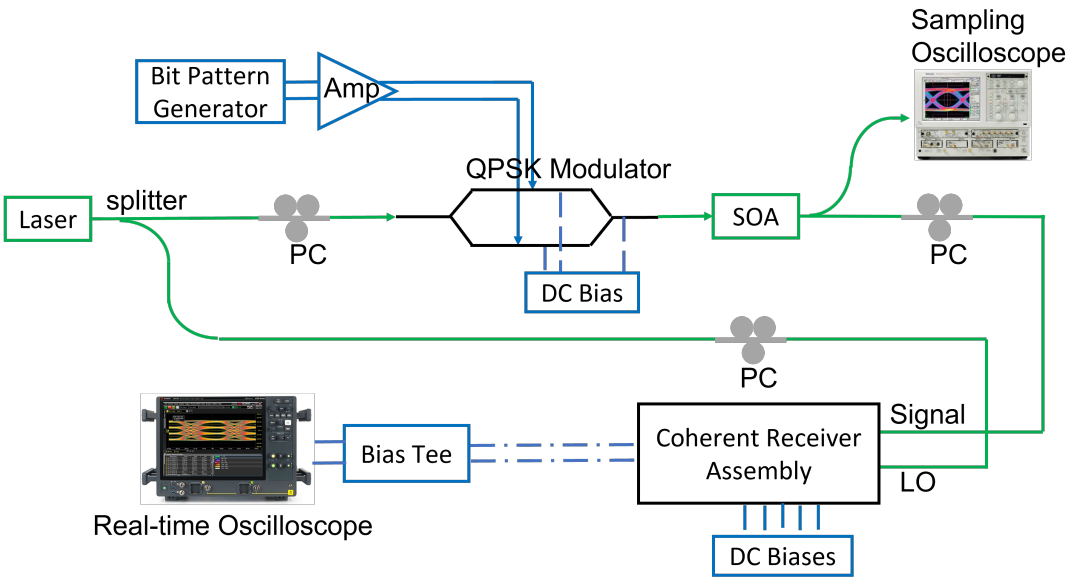

Figure 2.1: General coherent measurement setup

2.2 Script for Equipment Control and Data Presentation

Based on the general setup and the type of equipment available in the lab, the two-channel real time oscilloscope shows waveforms of the outputs from one of the I channels and one of the Q channels of the receiver. However, it is very difficult to tell the phase relation between I and Q simply by looking at the two waveforms directly. Usually, the data from the coherent receiver need to be presented in the format of a constellation diagram for straightforward understanding and qualification of the data. For this reason, a script is needed to present the data in the format of a constellation diagram. While it is an option to download the data from the oscilloscope and process the data on a computer later, real time feedback is more desirable so that optimizations on biases for the electronics and photonics part can be made during the measurement process. For those two reasons, the script that is used in the measurement needs to be able to send commends to the oscilloscope to make acquisition then download the data, to plot the acquired data into constellation diagrams and provide information such as BER, and to do this continuously until the data need to be saved or the measurement is stopped. Some commercial software can take care of that, but here we choose to develop our own script in order to meet our specific needs, and also to have better control over how the data is processed.

The flow chart of the script is shown in Fig. 2.2. It starts by setting up communication with the oscilloscope, and then send out the commend for the oscilloscope to do an acquisition. Afterwards, the data is processed and presented in the format of constellation diagrams, and BER values are calculated. The cycle continues, and the user can choose to save the data when they are satisfied with the result.

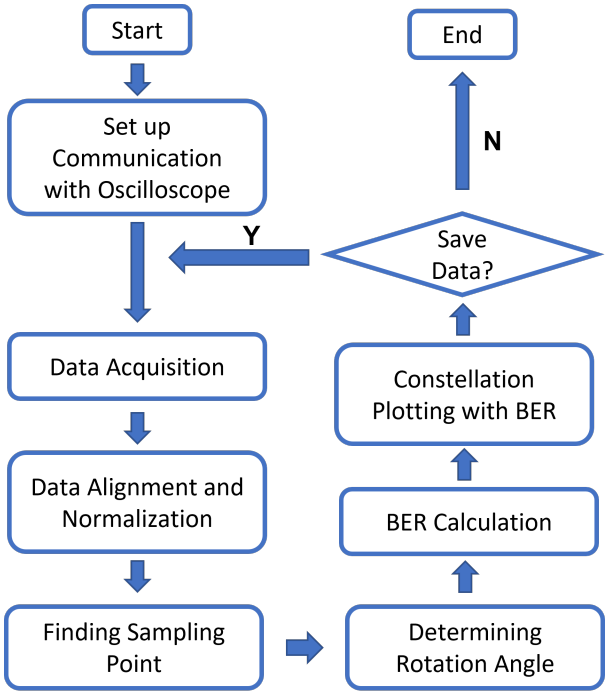

Figure 2.2: Measurement script flow chart

2.2.1 Data Acquisition

Commands for setting up the communication with the real time oscilloscope and data acquisition are specific to the particular model of equipment being used. The process usually involves establishing communication with the oscilloscope, and converting the raw data into actual voltage and time values. One thing to note is that enough data points are needed to represent the full length of the PRBS signal, so the total number of data points being aquired need to be determined based on the data rate, the PRBS signal length, and the sampling rate.

For example, assume we need to plot a constellation diagram of 10 GBaud QPSK signal, which needs to cover the full length of PRBS15 signal. The length of the PRBS15 signal is $2^{15} - 1 = 32767$. If the sampling rate of the real time oscilloscope is set to be 256 Gb/s per channel, the number of samples in a bit is $256/10 = 25.6$. So each channel needs to capture at least $25.6 \times 32767 = 838835.2$ sampling points to cover the full length

of PRBS15 signal. In the oscilloscope setting, the memory depth needs to be larger than this number, and the input buffer size in the script should be set up accordingly when creating the communication between computer and equipment.

2.2.2 Data Alignment and Normalization

Sometimes the I and Q data obtained on the real time oscilloscope may be misaligned with each other as a result of a built-in delay between the channels on the oscilloscope, or length mismatch of high speed traces on PCB. This effect will be more significant at higher data rate, since the period of one bit gets smaller and the amount of misalignment gets more comparable with the bit period. The amount of misalignment can be determined by directly observing the relationship between the signals on the two channels at a low data rate to avoid ambiguity. The misalignment can be compensated by moving one set of data relative to the other according to the amount of mismatch, so that the I and Q data points are aligned in time with each other.

Also, the I and Q data need to be normalized to compensate for the possible amplitude imbalance in the I and Q channels from the device. For each channel, the normalization process is as follows: firstly, the DC offset of the signal is removed; then the voltage values are normalized relative to the average of their absolute value.

2.2.3 Plotting the Constellation Diagram

In order to understand how to plot the I and Q data from the receiver into a constellation diagram, we need to firstly understand how the I and Q data are related to the phase of the incoming signal.

In coherent detection, mixing the signal and LO in the 90-degree hybrid produces the I,I',Q and Q'components of the photocurrent. Based on the derivation process of Eq. 1.5,

the photocurrent values can be expressed as

$$i_I(t) \propto \mid A_S \mid^2 + \mid A_{LO} \mid^2 + 2A_S \cdot A_{LO} \cos(\omega_{IF} t + \Delta\phi(t)) \tag{2.1}$$

$$i_{I'}(t) \propto \mid A_S \mid^2 + \mid A_{LO} \mid^2 - 2A_S \cdot A_{LO} \cos(\omega_{IF} t + \Delta\phi(t)) \tag{2.2}$$

$$i_Q(t) \propto \mid A_S \mid^2 + \mid A_{LO} \mid^2 + 2A_S \cdot A_{LO} \sin(\omega_{IF} t + \Delta\phi(t)) \tag{2.3}$$

$$i_{Q'}(t) \propto \mid A_S \mid^2 + \mid A_{LO} \mid^2 - 2A_S \cdot A_{LO} \sin(\omega_{IF} t + \Delta\phi(t)) \tag{2.4}$$

A_S and A_{LO} represent the amplitude of the signal and LO. ω_{IF} is the intermediate frequency, where $\omega_{IF} = \omega_S - \omega_{LO}$. In this self-homodyne measurement setup, signal and LO come from the same laser, so $\omega_{IF} = 0$. $\Delta\phi(t)$, being the phase difference between signal and LO, can be expressed as $\Delta\phi(t) = \phi_S(t) - \phi_{LO}(t)$. It can also be interpreted as $\Delta\phi(t) = \phi_{mod}(t) + \Delta\phi_{diff}(t) + \Delta\phi_n(t)$, where $\phi_{mod}(t)$ is the intentional phase difference introduced by modulation, and the other components results from effects other than modulation. For example, built-in length difference of the waveguides leading up to the signal and LO ports of the receiver may lead to a fixed additional phase difference in addition to the modulated phase difference. Also, vibration may cause change in fiber refractive index, which would result in additional phase difference. Those effects are incorporated in the parameter $\Delta\phi_{diff}(t)$. The third term, $\Delta\phi_n(t)$, is the phase noise term and is related to the combined linewidth of the signal and LO laser. In the case of the self-homodyne measurement, the LO and signal come from the same laser, so the term is related to the linewidth of the laser as well as the path length difference of the signal and LO path from the laser to the receiver.

Phase noise has a great impact on the performance of phase-diversity coherent system, since the information in this system is directly related to the phase term. Phase noise exists in both the signal and LO, and the differential phase noise term is added to the intentional phase change introduced from modulation. This effect would show up directly in the photocurrent.

In our setup, the signal and LO come from the same laser split into two paths. When the two path lengths before reaching the receiver chip are not exactly the same, the two phase noise values can be seen as two observations of the phase noise separated by a time interval dt. For this reason, the differential phase noise term $\Delta\phi_n(t)$ can be modeled as a Gaussian distribution where $\mu = 0$, and $\sigma^2 = 2\pi \cdot \Delta\nu \cdot dt$, where $\Delta\nu$ represents the laser linewidth, and dt is associated with the path lengths difference between signal and LO path.

Since two adjacent constellation points have $\frac{\pi}{2}$ phase difference, intuitively, the differential phase noise needs to be much smaller compared with $\pm\frac{\pi}{4}$ for preventing errors and ambiguities. Assuming in the measurement we use a 5 MHz linewidth laser, then the phase variation is roughly $\pm\pi$ in the time range of 0.2 μs, which is the inverse of the linewidth. For a differential phase noise much lower than $\pm\frac{\pi}{4}$, dt should not exceed $\frac{0.2\mu s}{40} = 5ns$, which is associated with about $\sim$ 1 m path lengths difference in fiber.

From Eq. 2.1 - 2.4, the AC terms of the photocurrent is associated with the phase difference between signal and LO, and the photocurrents can be shown in the complex plane where I is the in-phase or real part and Q is the quadrature or imaginary part. The constellation diagram can be obtained by plotting the AC part of I data on the X axis and the AC part of Q data on the Y axis.

Finding the Sampling Points

At the output of the coherent receiver, the QPSK signal has been demodulated and shows up in the format of on-off signal. As a result of limited bandwidth of all the devices and equipment involved in the measurement, the I and Q waveforms have non ideal rising and falling edges, which would take up a higher portion of the bit length when the data rate increases. Based on the data rate and the sampling rate of the real time oscilloscope, there are multiple data points acquired within the time frame of one bit. When plotting the constellation diagram, we need to pick the points at the center of the bits, instead of those at the rising edge or falling edge. Since all bits have equal length of time, theoretically, they all have the same number of sampling points. For this reason, the number of sampling options is associated with the number of sampling points in one bit period of time. If we define b as the number of samples per symbol (b can be a decimal), i.e., b=sampling rate/baud rate, then the processing of choosing the sampling point representing the nth bit can be described as $m = round(n \times b) + shift$, where m is the index of the sampling point being chosen, round() is the operation of finding the nearest integer, and shift ranges from 0 to round(b), determining the position of the chosen sampling point relative to the bit. With this method, the index interval for picking sampling points that represent the bits will vary from time to time because of the rounding process. If we want to avoid this problem altogether, the sampling rate has to be a integer multiple of the data rate. When this is not the case, we can interpolate based on the sampling points obtained from the oscilloscope, and obtain new data points which will make b an integer number.

Having obtained all the different sets of sampling points, the next question is which set should be picked to represent the bits. One way of doing this is to save the acquired data first, then manually pick the set of data by observing their distribution on the waveform,

or by comparing the constellation diagrams based on different sets of data. However, for a continuously running script and real time feedback, an approach utilizing a well-defined parameter is needed. The error vector magnitude (EVM) of the constellation can be used as the parameter to determine which set of sampling points is the most appropriate for representing the data.

EVM is a measurement of modulator or demodulator performance in the presence of impairments. It is a measurement of how much the constellation diagram deviates from the ideal case. For one data point, the error vector magnitude EVM[n] is the Euclidean distance between the measured point and the ideal reference point, as in Fig. 2.3:

$$EVM[n] = \sqrt{I_{err}[n]^2 + Q_{err}[n]^2} \tag{2.5}$$

where n is the symbol index and $I_{err} = I_{Meas} - I_{Ref}$ and $Q_{err} = Q_{Meas} - Q_{Ref}$.

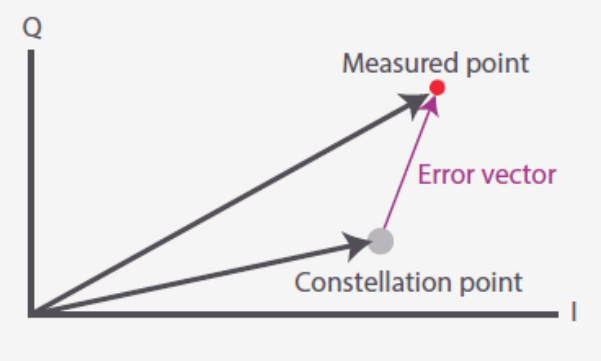

Figure 2.3: Definition of EVM

The normalized root mean square average EVM is defined as:

$$\%EVM = \frac{\frac{1}{N}\sum_{k=0}^{N-1}\sqrt{I_{err}[k]^2 + Q_{err}[k]^2}}{|Peak\ reference\ vector|} \tag{2.6}$$

where N is the number of measured points taken into account for calculating the EVM_{rms}.

Based on this definition, the lower the EVM value, the closer the constellation is to the ideal constellation diagram. Intuitively, when the sampling points are chosen at the rising and falling edges rather than the center, the values will be more spread out, since values representing the center of a bit may get chosen for the cases where there's a long stream of ones and zeros. And when the sampling points are chosen at the center, the constellation will be more concentrated on the four points for the QPSK. For this reason, the sampling points can be chosen by comparing the EVM values of the constellation diagrams generated by different sets of sampling points.

However, as discussed, $\Delta\phi(t)$ may have additional components other than the modulation phase term. In this case, all the points in the plotted constellation will be rotated relative to the way a QPSK constellation diagram is typically presented, which is shown in Fig. 1.4(a). If we calculate EVM based on rotated constellation and standard QPSK, the result may lead to incorrect choice of sampling points representing the bits.

One way to solve this problem is to rotate either the acquired constellation or the reference constellation, the method of which is explained later in this section. Another way that we have utilized in the script is the feed-forward Mth power phase estimation (or Viterbi and Viterbi algorithm [1]), however, it is used differently from its original purpose.

From the I and Q photocurrent, the complex optical field can be reconstructed as

$$E[n] = i_I[n] + ji_Q[n] = A[n]e^{j\theta[n]} \tag{2.7}$$

Theoretically, QPSK constellation only has four values for $\theta[n]$: $\pi/4$, $-\pi/4$, $3\pi/4$, and $-3\pi/4$. Assuming the constellation is rotated by $\pi/4$, the $\theta[n]$ values would be 0, $\pi/2$, π, and $3\pi/2$ instead. In this case, the phase for $E^4[n]$ should be 0, 2π, 4π, and 6π, which are all located on the same position of the complex plane. Any deviation from this point

is considered to be caused by phase terms other than the modulation. Then the phase deviation $\phi_e[n]$ can be calculated and its impact can be compensated by multiplying the original complex optical field by $e^{-j\phi_e[n]}$. Later, the intentional phase rotation can be recovered by multiplying the complex optical field by $e^{j\frac{\pi}{4}}$ [2, 3].

This algorithm is typically used for phase recovery, and the estimated phase deviation needs to be averaged over a certain block length, which depends on the amount of noise and the symbol rate. However, in our application, we are only using this method to position the constellation diagram points to the standard point positions. In this way, the EVM value can be used more reliably for choosing the sampling points, since the method not only makes sure that the EVM is comparing the acquired constellation and the reference constellation based on the same standard of ideal phase values, but it does not change the distribution of data points in the constellation as a result of sampling position relative to the bits: the bit points will be more concentrated around the four phase values for sampling points in the middle of the bits, and more spread out for sampling points on the rising or falling edges. In the constellation diagram plotting for this dissertation, this algorithm is only used as an effective way to find the location for sampling, and is not used for changing the distribution of points on the final constellation diagram.

Determining the Rotation Angle

In the previous steps, the bits are sampled in the middle and the sampling points give an accurate representation of the received bits. However, as a result of additional components other than the modulation phase term, constellation diagrams directly plotted from those points may be rotated compared with a standard QPSK diagram. The method to compensate for this is to rotate all the data points in one acquisition by the same angle. In other words, the rotation value is specific to each acquisition, but is not

specific to the individual points in the same acquisition.

In order to find the best rotation angle, EVM is chosen again as the figure of merit. Since the constellation points are 90 degree apart, the constellation is rotated from 0 to 89 degree at 1 degree interval, and the EVM value is calculated. The angle which results in the lowest EVM is chosen as the rotation angle.

2.2.4 BER Calculation

The bit error ratio (or bit error rate, BER) can be defined as the estimated probability that any bit transmitted through the system will be received in error. In practical tests, the BER is measured by transmitting a finite number of bits through the system and counting the number of bit errors received. The ratio of the number of bits received erroneously to the total number of bits transmitted is the BER.

Initially, we tried using EVM value to estimate the BER value with the method proposed in [4]. However, the accuracy of the estimation depends a lot on the primary source of the errors, and the carrier phase needs to be recovered perfectly. Since we do not use DSP for carrier phase recovery of the final data, we decide that the more accurate way for BER calculation is to count the number of erroneous bits and divide the number by the total number of bits being transmitted.

In order to determined which bits are received in error, we need to compare the bits being transmitted and the bits being received. Since it is not straightforward to use a bit error analyzer in the case of QPSK modulation for this purpose, we need to reproduce the transmitted bits with the script. PRBS streams are used for modulation, and the sequence can be reproduced in script by using linear-feedback shift registers. However,more consideration needs to be put into interpreting the data being received. As a result of the rotation of the constellation diagram, the received I and Q signal may have

the same or inverted sign compared with the transmitted signal. Also, the transmitted signal reproduced with the script and the received signal need to be synchronized with each other before the number of errors can be counted.

So we process the received data in two different ways: assign above threshold data points to 1 and the others to 0; and assign above threshold data points to 0 and the others to 1. Afterwards, both of the streams are synchronized with PRBS data streams using MATLAB cross correlation function, and then the numbers of errors get counted. Between the two error values, the smaller value is chosen. The same process is done on both I and Q data, and BER value is calculated by dividing the sum of I and Q errors by the total number of I and Q bits being transmitted.

The threshold for 0 and 1 assignment is typically chosen as zero. It is also possible to optimized the BER value by optimizing the threshold value. In the script, this is done by analyzing the data point distribution around 0 to decide on a range of threshold optimization, and then finding a new threshold within the range to minimize the BER. It should be noted that there is only one fixed threshold value for I and one fixed threshold value for Q in the same acquisition.

2.3 Preliminary Measurement Assemblies

Based on the discussion in Section 2.2, data from I and Q outputs of the receiver are needed at the same time in order to generate a constellation diagram. In order to verify and develop the measurement procedure including the script, we put together two versions of stand-alone PIC assemblies and use them as a starting point for this process. Fig. 2.4 shows the two PIC assemblies and the preliminary constellation diagrams obtained from them. In both of the assemblies, the anodes of the photodetectors are directly wire bonded to the high speed traces on the PCB, which lead to RF connectors, whereas the

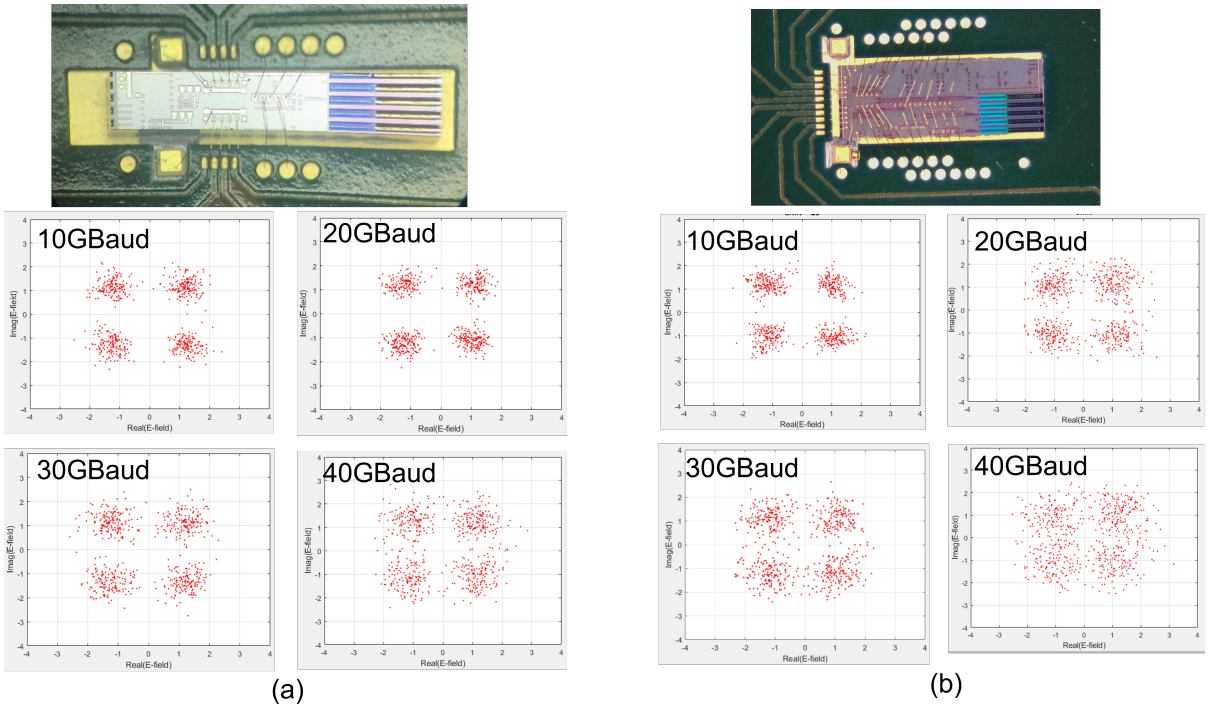

Figure 2.4: Preliminary PIC assemblies and constellation diagrams. (a) PIC without polarization recovery (b) PIC with polarization recovery

common cathode is grounded, with a decoupling capacitor to filter out the noise. The details of the PIC design will be discussed in Chapter 3 and Chapter 6. At the point of obtaining those constellation diagrams, a lot of the functionalities in the script have not been developed yet, and the procedure of plotting the constellation diagram was different from those in later measurements. Since then, we have continued to learn more about the measurement procedure, and the script is developed into what has been described in this chapter.

Bibliography

[1] A. J. Viterbi and A. M. Viterbi, *Nonlinear estimation of psk-modulated carrier phase with application to burst digital transmission*, *IEEE Transactions on Information Theory* **29** (1983), no. 4 543–551.

[2] P. Bayvel, C. Behrens, and D. S. Millar, *Chapter 5 - digital signal processing (dsp) and its application in optical communication systems*, in *Optical Fiber Telecommunications (Sixth Edition)* (I. P. Kaminow, T. Li, and A. E. Willner, eds.), Optics and Photonics, pp. 163–219. Academic Press, Boston, sixth edition ed., 2013.

[3] R. Hui, *Chapter 11 - application of high-speed dsp in optical communications*, in *Introduction to Fiber-Optic Communications* (R. Hui, ed.), pp. 497–553. Academic Press, 2020.

[4] R. Schmogrow, B. Nebendahl, M. Winter, A. Josten, D. Hillerkuss, S. Koenig, J. Meyer, M. Dreschmann, M. Huebner, C. Koos, J. Becker, W. Freude, and J. Leuthold, *Error vector magnitude as a performance measure for advanced modulation formats*, *IEEE Photonics Technology Letters* **24** (2012), no. 1 61–63.

Chapter 3

Coherent Receiver Based on GlobalFoundries PIC Platform

This chapter discusses a coherent receiver based on GlobalFoundries PIC platform. An introduction of the 90WG technology will be provided, followed by design considerations and measurement results of individual photonic components as well as the photonic receiver. Then the measurement results of two different assemblies with the same PIC design and different EIC designs are presented.

3.1 GlobalFoundries 90WG Technology

The GlobalFoundries 90WG technology is a sub-micron silicon-on-insulator (SOI) process [1] with waveguide width of 350 nm (single mode) and 810 nm (multi mode). The platform offers ridge and rib waveguides, high-speed Ge photodetectors, and V-groove and metamaterial converters for fiber coupling. The platform also supports polarization multiplexing, and offers a polarization splitter rotator (PSR) in its PDK library. In addition, the platform enables monolithic integration with CMOS devices, including

transmitter drivers and receiver TIAs and limiting amplifiers [1].

High-speed photodetectors are vital components in the receiver optical front end. Its key properties for receiver application are responsivity and bandwidth. A high responsivity means that the PDs are more effective in converting optical signal into electrical signal for the interface with the EIC receiver, and higher bandwidth leads to overall better performance of the receiver: higher data rate and lower BER. The PDs in the 90WG process show responsivity of approximately 1.0 A/W and a bandwidth of approximately 40 GHz, as shown in Fig 3.1.

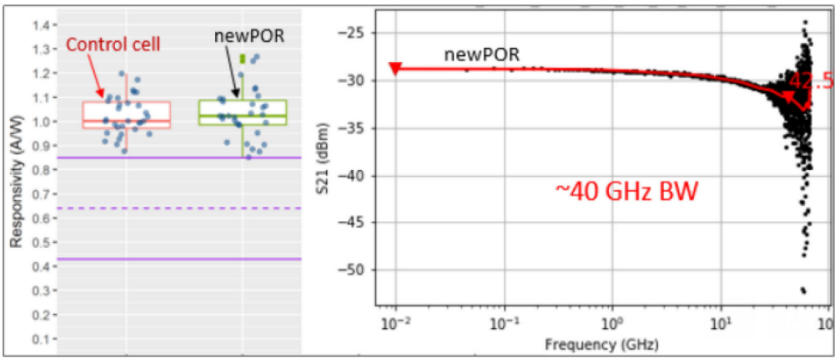

Figure 3.1: The responsivity and bandwidth of photodetectors ©2019 IEEE

The edge coupler offered by the 90WG platform is based on a metamaterial interface, which is different from the typical inverse taper structure. The metamaterial converter is composed of three sections: a metamaterial taper, a hybrid taper, and a solid waveguide taper, as shown in Fig. 3.2(a). A standard single-mode fiber can be self-aligned through an integrated V-groove, as can be seen in the cross section shown in Fig. 3.2(b). With index matching fluid, the coupler shows -1.3 dB peak transmission efficiency and supports both TE and TM polarizations, which is vital for polarization diversity receiver applications. The spectrum measurement of the fiber interface is shown in Fig. 3.2(c) [2].

The PSR is another important device for polarization management. The structure of

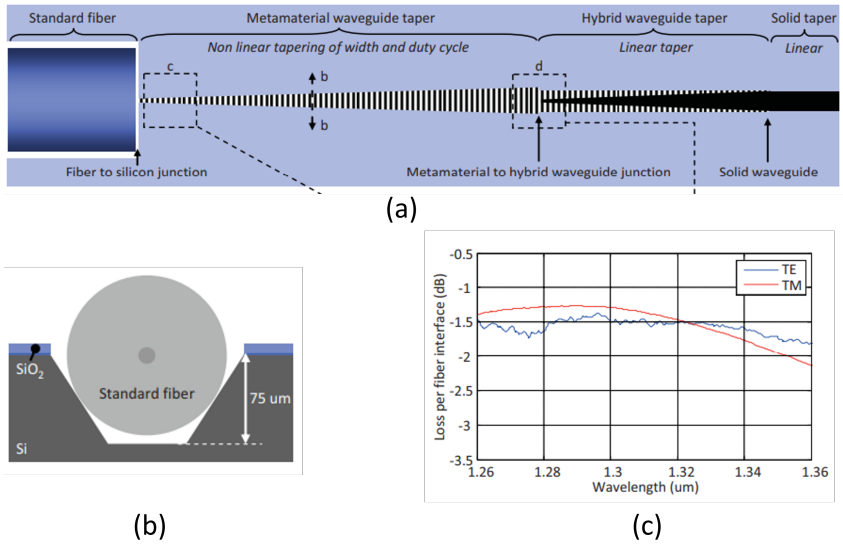

Figure 3.2: (a) Structure of the metamaterial fiber interface; (b) cross section of the V-groove and fiber; (c) spectral measurement of the coupler for TE and TM ©2015 IEEE

the PSR is shown in Fig. 3.3(a) and (b). It consists of a polarization splitter to separate the TE and TM components, a polarization rotator to rotate the TM polarization to TE, and clean-up splitters filtering residual TM. The measured device insertion loss is $\leq$ 1.0 dB, the polarization-dependent loss is $\leq$ 1.0 dB, and the polarization extinction ratio is better than 27 dB, as in Fig. 3.3(c),(d) and (e) [3].

3.2 Design and Measurement Results of Components and Test Structure

3.2.1 90-degree Hybrids

The reason for using an LO is to measure not the absolute phase, but the phase relative to a known reference signal. For this reason, it is intuitive to think of the 90-degree hybrid as a structure where the I and Q are provided as two separate signals, and the LO is split into two paths with one of them shifted by 90 degrees relative to the

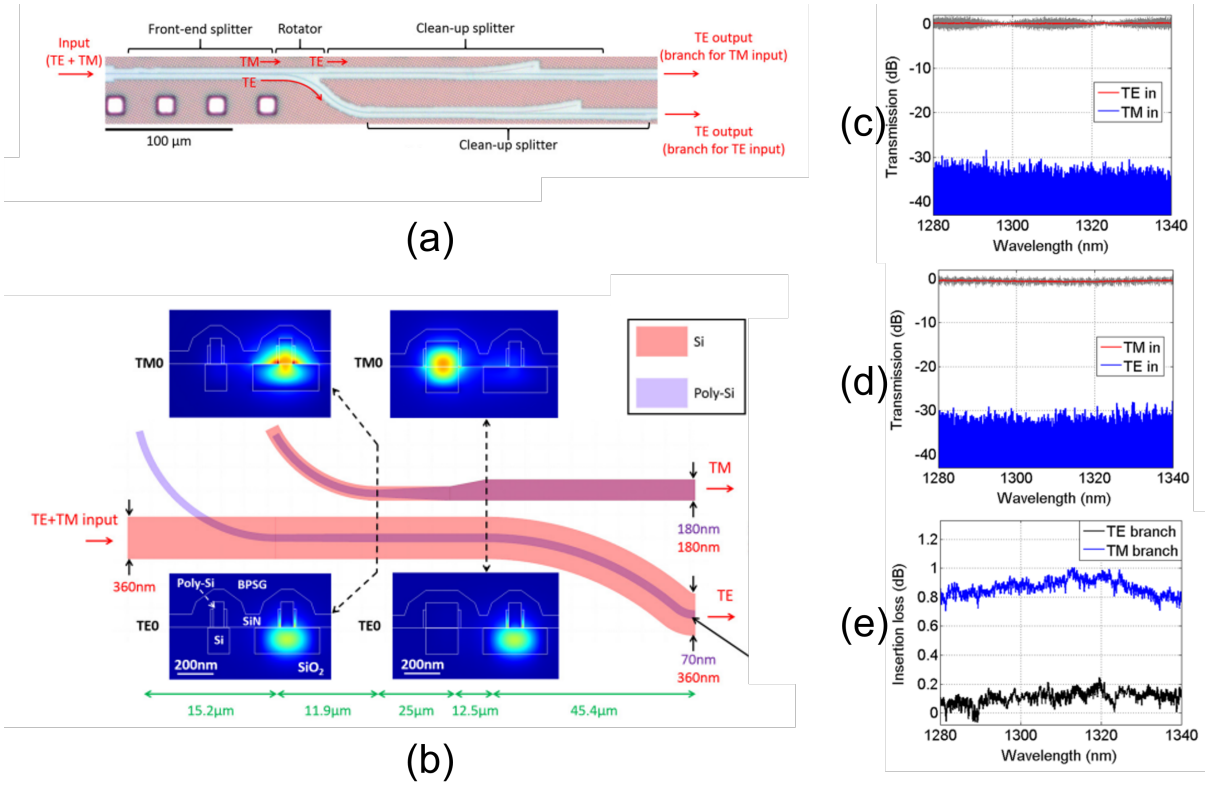

Figure 3.3: (a) Structure of the PSR; (b) schematic of the polarization splitter and mode profile; (c) output of the TE branch; (d) output of the TM branch; (e) insertion loss of both outputs

other. For this reason, the four outputs of the 90-degree hybrid E_1,E_2,E_3 and E_4 can be expressed as:

$$\begin{bmatrix} E_1 \\ E_2 \\ E_3 \\ E_4 \end{bmatrix} = \frac{1}{2}\begin{bmatrix} 1 & 1 \\ 1 & -1 \\ 1 & j \\ 1 & -j \end{bmatrix}\begin{bmatrix} E_S \\ E_{LO} \end{bmatrix} = \begin{bmatrix} \frac{E_S}{2} + \frac{E_{LO}}{2} \\ \frac{E_S}{2} - \frac{E_{LO}}{2} \\ \frac{E_S}{2} + j\frac{E_{LO}}{2} \\ \frac{E_S}{2} - j\frac{E_{LO}}{2} \end{bmatrix} \tag{3.1}$$

Since the photocurrent at the photodetector is proportional to the optical power, the

four photocurrents can be expressed as:

$$I \propto |E_1||E_1^*| = \frac{1}{4}|E_S|^2 + \frac{1}{4}|E_{LO}|^2 + \frac{1}{2}|E_S||E_{LO}|\cos(\phi_S - \phi_{LO}) \tag{3.2}$$

$$I' \propto |E_2||E_2^*| = \frac{1}{4}|E_S|^2 + \frac{1}{4}|E_{LO}|^2 - \frac{1}{2}|E_S||E_{LO}|\cos(\phi_S - \phi_{LO}) \tag{3.3}$$

$$Q \propto |E_3||E_3^*| = \frac{1}{4}|E_S|^2 + \frac{1}{4}|E_{LO}|^2 + \frac{1}{2}|E_S||E_{LO}|\sin(\phi_S - \phi_{LO}) \tag{3.4}$$

$$Q' \propto |E_4||E_4^*| = \frac{1}{4}|E_S|^2 + \frac{1}{4}|E_{LO}|^2 - \frac{1}{2}|E_S||E_{LO}|\sin(\phi_S - \phi_{LO}) \tag{3.5}$$

Based on Eq. 3.1, there are two most common ways of designing a 90-degree hybrid: 3-dB couplers with phase delays, and 4×4 MMIs [4].

3-dB Couplers with Phase Delays

Fig. 3.4 shows the layout and schematic of the 90-degree hybrid based on 3-dB couplers and phase shifters. In order to offer more tuning flexibility in the 90-degree hybrid, we put phase shifters on two of the waveguide paths, and the other two waveguides have the same length. In the layout, the unused input ports of the 3-dB couplers are terminated by absorbers. The phase shifters need to be tuned properly for the structure to function as a 90-degree hybrid. One way of biasing the thermal phase shifters is to tune one of them to have the same phase shift as the fixed length waveguides and tune the other one to have an extra 90 degree phase shift. But after going through the derivation, a conclusion can be drawn that as long as $\theta_1 + \theta_2 = \frac{\pi}{2} + n\pi$, θ_1 and θ_2 being the relative phase shift values to the fixed length waveguides, the structure is set up properly as a 90-degree hybrid.

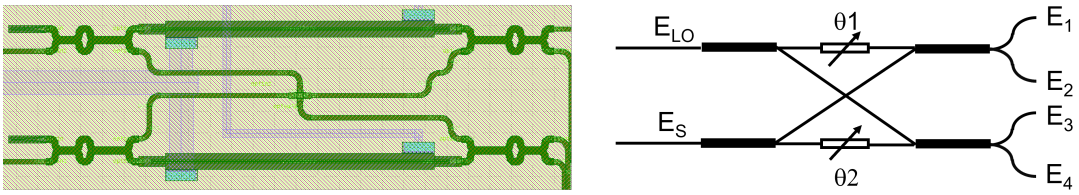

Figure 3.4: Layout and schematic of the 90-degree hybrid

Based on the definition of θ_1 and θ_2, E_1,E_2,E_3 and E_4 in Fig. 3.4 can be expressed as:

$$E_1 = \frac{1}{2}E_{LO}\mathrm{e}^{j(\frac{\pi}{2}+\theta_1)} + \frac{1}{2}E_S\mathrm{e}^{j\pi} \tag{3.6}$$

$$E_2 = \frac{1}{2}E_{LO}\mathrm{e}^{j(\pi+\theta_1)} + \frac{1}{2}E_S\mathrm{e}^{j\frac{\pi}{2}} \tag{3.7}$$

$$E_3 = \frac{1}{2}E_{LO} + \frac{1}{2}E_S\mathrm{e}^{j(\frac{\pi}{2}+\theta_2)} \tag{3.8}$$

$$E_4 = \frac{1}{2}E_{LO}\mathrm{e}^{j\frac{\pi}{2}} + \frac{1}{2}E_S\mathrm{e}^{j\theta_2} \tag{3.9}$$

From here the RF component of the photocurrent can be derived:

$$I, I' \propto \pm|E_{LO}||E_S|\sin(\theta_1 - \Delta\phi) \tag{3.10}$$

$$Q, Q' \propto \pm|E_{LO}||E_S|\cos(\frac{\pi}{2} - \theta_2 - \Delta\phi) \tag{3.11}$$

where $\Delta\phi = \phi_S - \phi_{LO}$.

For the 90-degree hybrid to work properly, intuitively, we need $\theta_1 - \Delta\phi = \frac{\pi}{2} - \theta_2 - \Delta\phi$, which leads to $\theta_1 + \theta_2 = \frac{\pi}{2}$. And it also works when $\theta_1 - \Delta\phi = \frac{\pi}{2} - \theta_2 - \Delta\phi + n\pi$. In this case, the sine or cosine functions will still have the same values with the sign flipped.

This offers some flexibility in tuning, and it is possible to find an configuration that is more energy saving than others.

4×4 MMI

The working principle of MMIs is self-imaging, which is defined as a property of multimode waveguides by which an input field profile is reproduced in single or multiple images at periodic intervals along the propagation direction of the waveguide. The central structure of an MMI device is a waveguide designed to support a large number of modes (typically ≥ 3). In order to launch light into and recover light from that multimode waveguide, a number of access (usually single-moded) waveguides are placed at its beginning and at its end. Such devices are generally referred to as N $\times$ M MMI couplers, where N and M are the number of input and output waveguides, respectively [5].

The analysis can be started by assuming a step-index multimode waveguide of width W_M, ridge (effective) refractive index n_r and cladding (effective) refractive index n_c. The waveguide supports m lateral modes with mode numbers $\nu = 0, 1, ...(m-1)$ at a free-space wavelength λ_0. The lateral wavenumber k_{yv} and the propagation constant β_ν are related to the ridge index n_r by the dispersion equation

$$k_{yv}^2 + \beta_\nu^2 = k_0^2 n_r^2 \tag{3.12}$$

with

$$k_0 = \frac{2\pi}{\lambda_0} \tag{3.13}$$

$$k_{yv} = \frac{(\nu+1)\pi}{W_{e\nu}} \tag{3.14}$$

where $W_{e\nu}$ is the effective width, and can be approximated by the effective width W_{e0} corresponding to the fundamental mode, which shall be denoted W_e for simplicity.

Through derivation, the beat length of the two lowest-order mode, L_π, can be expressed as [5]

$$L_\pi = \frac{\pi}{\beta_0 - \beta_1} \approx \frac{4n_r W_e^2}{3\lambda_0} \tag{3.15}$$

For the formation of the positions and phases of N-fold images, [6] gives a more complete derivation. The conclusion is that N-fold images can be formed at the location

$$L_N^M = \frac{M}{N} 3L_\pi \tag{3.16}$$

where M and N are any positive integers without a common divisor. In practice, $M = 1$ can be chosen for shortest device length. And the phases of the signals for the N images are given by (excluding a constant phase value)

$$\phi_{rs} = \frac{\pi}{4N}(s - r)(2N + r - s) + \pi \text{ for } r + s \text{ even} \tag{3.17}$$

and

$$\phi_{rs} = \frac{\pi}{4N}(r + s - 1)(2N - r - s + 1) \text{ for } r + s \text{ odd} \tag{3.18}$$

where $r = 1, 2, ...N$ is the bottom up numbering of the input waveguides and $s = 1, 2, ...N$ is the top down numbering of the output waveguides [5].

Based on Eq. 3.17 and 3.18, we can come up with a table of the relative phase of 4×4 MMI outputs to its inputs. It should be noted that for convenience, in this paper, MMI inputs and outputs are numbered from top down unless otherwise specified. The calculation result is shown in Table 3.1.

Based on the derivation in Eq. 3.1, to determine whether the 4×4 MMI meets the

Table 3.1: 4×4 MMI phases (output relative to input)

input/output	1	2	3	4
1	π	$-\frac{\pi}{4}$	$\frac{3\pi}{4}$	π
2	$-\frac{\pi}{4}$	π	π	$\frac{3\pi}{4}$
3	$\frac{3\pi}{4}$	π	π	$-\frac{\pi}{4}$
4	π	$\frac{3\pi}{4}$	$-\frac{\pi}{4}$	π

phase requirements of 90-degree hybrid, we need to study the relative phase shift between output to LO input, as well as between output to signal input. The difference between those two values at the four outputs, $\phi_{LO\_out} - \phi_{Signal\_out}$ should be $\pi/4$, $3\pi/4$, $-\pi/4$ and $-3\pi/4$.

When inputs 1 and 2, 1 and 3, 2 and 4 or 3 and 4 are chosen as signal and LO inputs, the phase relation of the outputs meets the requirement for a 90-degree hybrid. It should be noted that unlike the 90-degree hybrid based on 3-dB couplers and phase shifters, where the outputs with π phase difference are next to each other, in the case of 4×4 MMIs, outputs 1 and 4 have π phase difference, and outputs 2 and 3 have π phase difference, and the two groups are orthogonal to each other. In order to make the wire bonding process with the EIC receiver easier, waveguide crossings need to be used to route the out of phase outputs next to each other.

In our design, we choose inputs 2 and 4 as signal and LO inputs, and terminated the two unused inputs with absorbers.

Test Structure Design and Measurement Results for 90-degree hybrids

The characterization of the hybrid consists of two parts: power imbalance of the 4 outputs, and the phase relation between the 4 outputs. If balanced photodetectors are used, the power balance between I and I' and also Q and Q' is vital for reaching a high

common mode rejection ratio. However, in our case, since the real time oscilloscope has two channels and only one of the I channels and one of the Q channels will be connected to the oscilloscope, the balancing is not as important as the phase relation.

The way to measure the phase relation of the 4 outputs of the 4×4 MMI is to introduce an imbalanced MZI at the two inputs of the device and measure the spectra of the 4 outputs and see their relation with each other, as explained in [7]. In order to achieve this, the two arms in the imbalanced MZI need to have a certain length difference. By doing that, different wavelengths will result in different phase offsets between the two paths of light after going through the two arms, and the power after recombining will have various levels of constructive and destructive interference according to the phase offset. There will be a periodic power level as a function of wavelength. The period, or the wavelength difference between two successive minima or maxima in the spectrum, is called the free spectral range (FSR). Generally speaking, the FSR value should be chosen so that it is not so large that the wavelength range of the lab equipment is not enough to cover a couple of FSRs, and at the same time it shouldn't be so small that it becomes difficult to get a nice spectrum where the power maxima and minima are captured with the resolution of the measurement tool. Based on all those considerations, we chose the FSR to be around 8 nm. Then we are able to calculate the length difference of the two arms of the imbalanced MZI. The length difference ΔL required to achieve a certain FSR can be calculated by

$$\Delta L = \frac{\lambda^2}{n_g FSR} \tag{3.19}$$

where λ is the operation wavelength and n_g is the group index around the wavelength.

We used similar test structures for the 90-degree hybrid based on 3-dB couplers and phase delays as well as the 4×4 MMI. Two examples are shown in Fig. 3.5. In those test

structures, grating arrays are utilized in order to couple to all the inputs and outputs at the same time using fiber array. The test structure didn't work out well for the 90-degree hybrid based on 3-dB couplers and phase delays because the FSR values were different for the two upper outputs and the two lower outputs. Fig. 3.7 shows an example of the spectra scan of one of those hybrids. For the 90-degree hybrid based on 4×4 MMIs, the method works out well and we were able to pick the optimized design parameters for the 4×4 MMI. Fig. 3.6 shows the measurement results of three 4×4 MMI variations with different lengths of the multi-mode section.

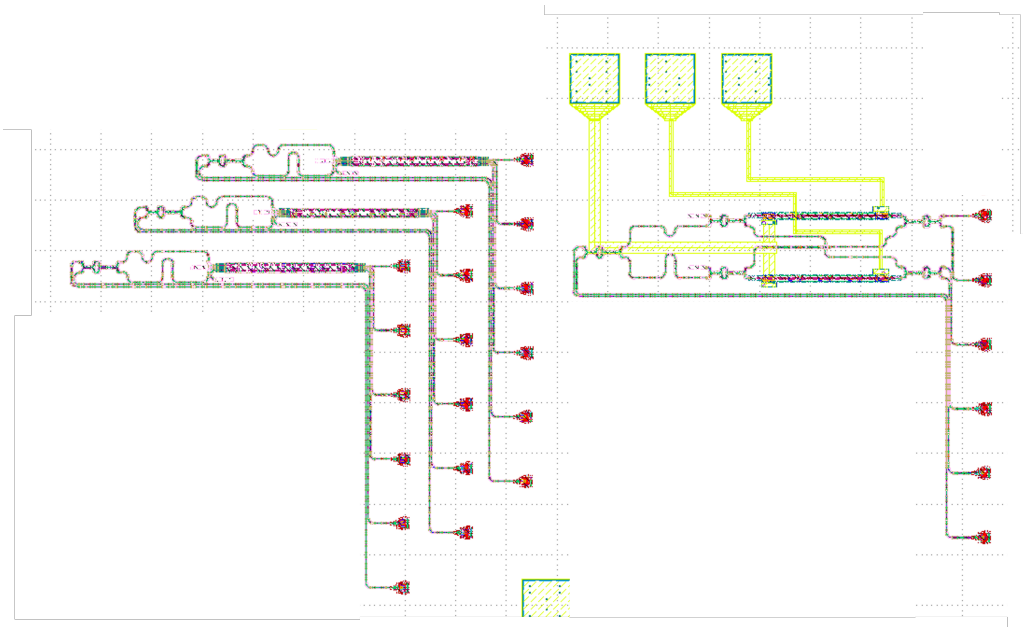

Figure 3.5: Examples of 90-degree hybrid test structures. Left: hybrid based on 4×4 MMI; Right: hybrid based on 3-dB couplers and phase delays

To interpret the data, firstly we measure the length of the FSR by measuring the wavelength spacing between adjacent power maxima or minima. Then we measure the wavelength shift of the four outputs relative to each other. Lastly, we convert wavelength shift into phase shift by dividing the wavelength shift by the FSR, then multiply the value by 2π:

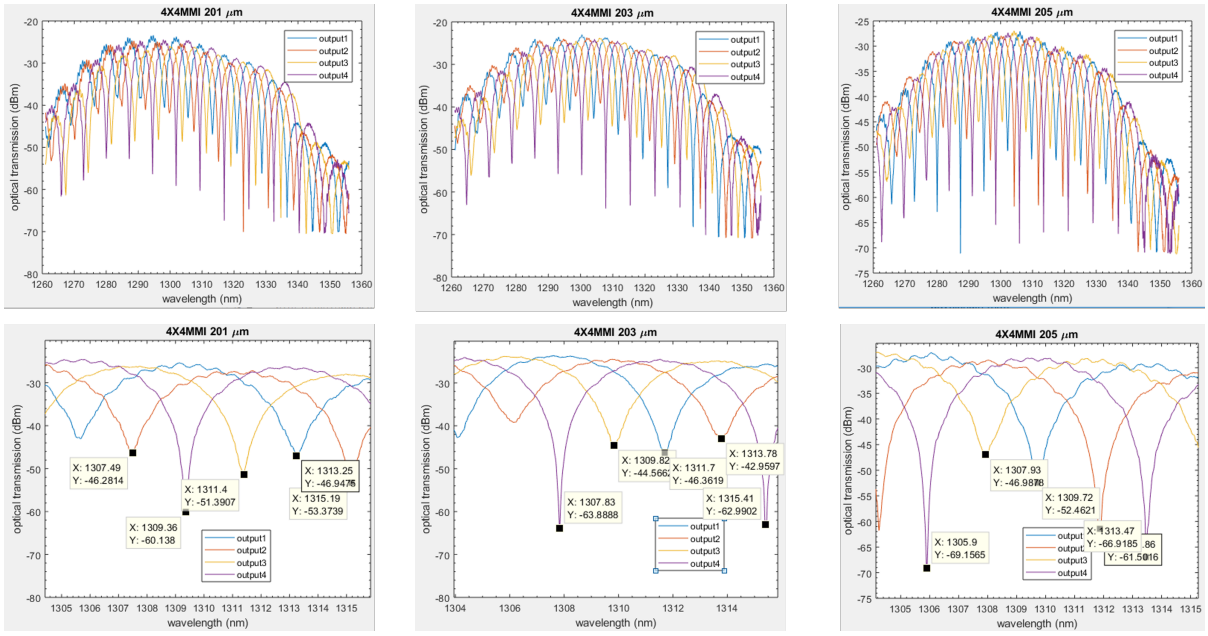

Figure 3.6: 4×4 MMI measurement results

$$\frac{\Delta\lambda}{FSR} = \frac{\Delta\phi}{2\pi} \tag{3.20}$$

The phase shift values of different 4×4 MMI variations are shown in Table. 3.2, and by comparing the measured phase shift values to the theoretical values, we pick 201 μm for MMI length as the optimized design for 4×4 MMIs in this process when the width is chosen as 10 μm.

For the 90-degree hybrid based on 3-dB couplers and phase delays, an example of the spectra is shown in Fig. 3.7 . The phase relation of the four outputs can not be obtained from the spectra since the outputs have two different FSR values. However, we are able to verify that the I and I' outputs do have π phase difference, so are the Q and Q' outputs. Also, it has been verified that the thermal phase shifters have the tuning range of a full 2π phase shift, so that the phase relation of those can be set up as needed in the measurement, and the functionality of 90-degree hybrid can be realized.

Table 3.2: 4x4 MMI phase measurement results

Design Variant	Ports	Min Transmission Wavelength (nm)	$\Delta\lambda(nm)$	%FSR	Phase Shift	Phase Error
201 μm FSR=7.7 nm	1	1313.25	0	0	0	0
	2	1315.19	1.94	0.252	90.7°	0.7°
	3	1311.4	-1.85	-0.240	-86.49°	3.51°
	4	1309.36	3.89	0.505	181.87°	1.87°
203 μm FSR=7.58 nm	1	1311.7	0	0	0	0
	2	1313.78	2.08	0.274	98.78°	8.78°
	3	1309.82	-1.88	-0.248	-89.29°	0.71°
	4	1315.41	3.71	0.489	176.2°	-3.8°
205 μm FSR=7.57 nm	1	1309.72	0	0	0	0
	2	1311.86	2.14	0.283	101.77°	11.77°
	3	1307.93	-1.79	-0.236	-85.13°	4.87°
	4	1313.47	3.75	0.495	178.34°	-1.66°

3.2.2 Thermal Phase Shifters

The tuning principle of thermal phase shifters is based on thermo-optic effect, which means the refractive index of the waveguide can be changed through temperature change. For this reason, heating up the waveguide can change the phase shift of light propagating through the same waveguide section. The tuning speed is slower compared with other mechanisms such as carrier dispersion effect and is typically on the order of microseconds, but it is not a concern in its application in 90-degree hybrids since the phase shift value needed is expected to be relatively stable.

Characterizing the efficiency of thermal phase shifters is very important for coherent receiver measurement. Based on the efficiency of the phase shifters and other information such as the length and effective index of the waveguides, a starting point for phase shifter

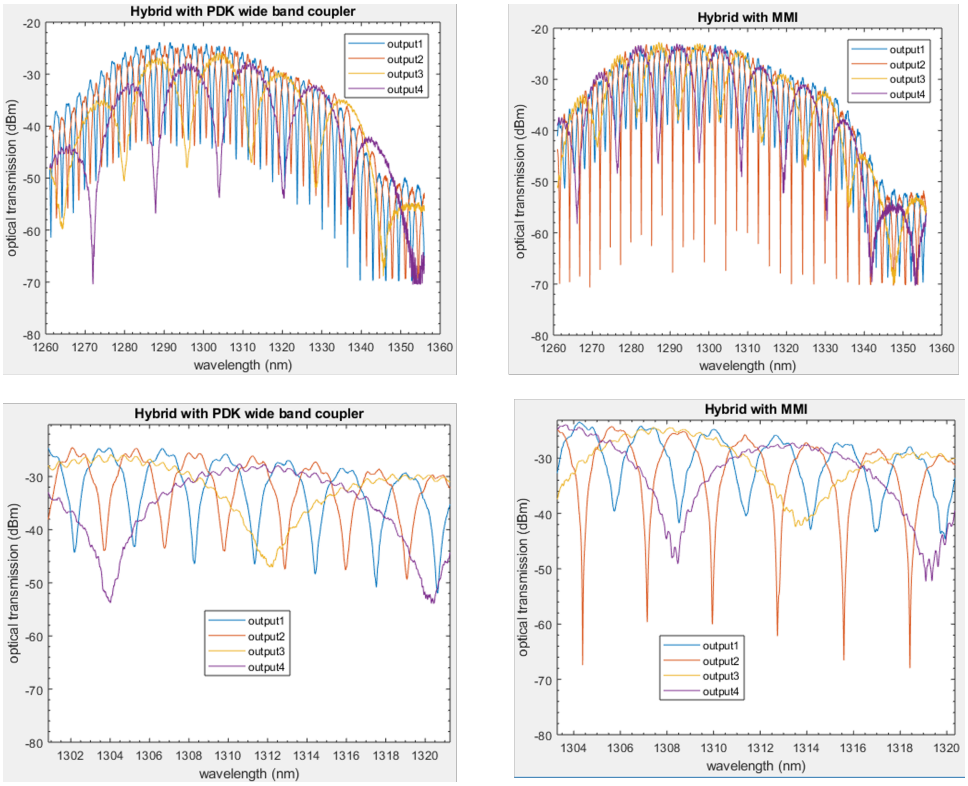

Figure 3.7: Hybrid measurement results

biases can be derived for coherent receiver characterization. In addition, improving the energy efficiency of the phase shifters can also benefit the overall power efficiency of the coherent link. The way to measure the efficiency of phase shifters, or in other words, the power consumption for a π phase shift, is to introduce an imbalanced MZI and create an FSR in the test structure, similar to the measurement for 4×4 MMI phase. An example of such a test structure and the measurement result from it is shown in Fig. 3.8. By varying the heater bias and observing the output power, the power consumption for a π phase shift can be measured.

Although the GlobalFoundries platform provides PDK thermal phase shifters, we also made some custom designs using similar structure as the PDK element for space saving purposes. We laid out a couple of variations with different lengths and widths of the resistors next to the waveguide, and we measured their resistance values and phase shift

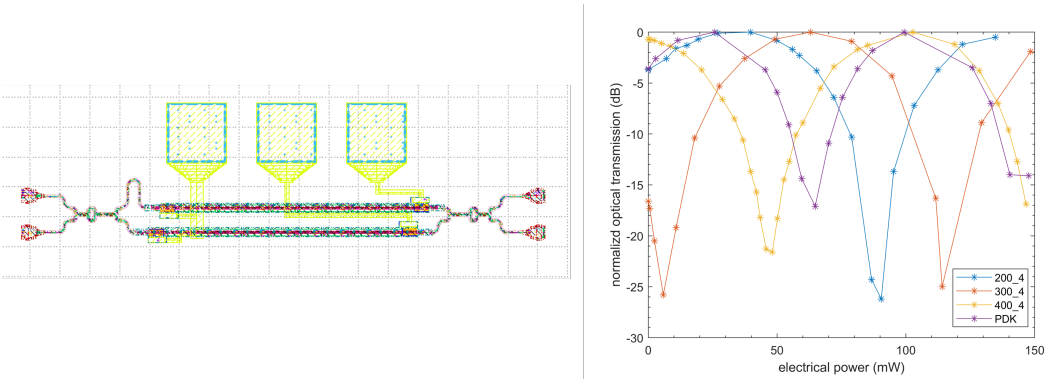

Figure 3.8: Thermal phase shifter test structure and measurement result

efficiency.

Fig. 3.9 shows a cross section of the PDK thermal phase shifters, which is also the structure used in custom heater design. The optical mode is inside the center waveguide area, and the heat is generated by resistors on both sides of the waveguide, with w being their width and L being their length.

The PDK phase shifter consists of 8 resistors in parallel, 4 on each side of the waveguide. Each resistor has a 2 μm width. The length of each resistor is around 200 μm, which makes the total length of resistor more than 800 μm.

In an effort to shorten the total length of the thermal phase shifter and keep the current density similar to the PDK design at the same time, we made a custom design of the phase shifter consisting of two resistors in parallel, one on each side of the waveguide. The resistor length is designed to be similar to that of the resistor in the PDK phase shifter (200 μm), and the width is four times of the resistor in the PDK structure (8 μm). Using those values as a starting point, we then come up with some other design variants of lengths and widths.

Table 3.3 shows a comparison of the resistance and efficiency values of different custom phase shifter resistor length and width designs, and the values for the PDK component are also listed for comparison. The PDK phase shifter shows the best efficiency, and

among the custom designs in this tapeout, the phase shifter resistor design with 200 μm length and 4 μm width shows the best thermal efficiency. With a much shorter length compared with the PDK design, this custom thermal phase shifter can be used when the design space is limited.

Figure 3.9: Cross section of thermal phase shifter

Table 3.3: Resistance and power consumption of different thermal phase shifter designs

Design Parameter	$R_{measured}(\Omega)$	Efficiency (mW/π)
$L = 200\mu m, w = 4\mu m$	183.65	50.85
$L = 300\mu m, w = 4\mu m$	267	57.15
$L = 400\mu m, w = 4\mu m$	351.75	51.15
$L = 200\mu m, w = 8\mu m$	98.15	74.27
$L = 300\mu m, w = 8\mu m$	143.2	76.56
$L = 400\mu m, w = 8\mu m$	203.65	85.6
PDK	95	39

3.2.3 Photodetectors

Fig. 3.10 shows a test structure for photodetector bandwidth measurement, as well as the OE S_{21} obtained by using external laser on LCA. From the measurement result, we can see that the photodetector bandwidth is higher than 40 GHz, which is consistent with the results in [1]. The data look noisy at high frequencies because the probe being used has a 40 GHz bandwidth and becomes the limiting factor in this measurement.

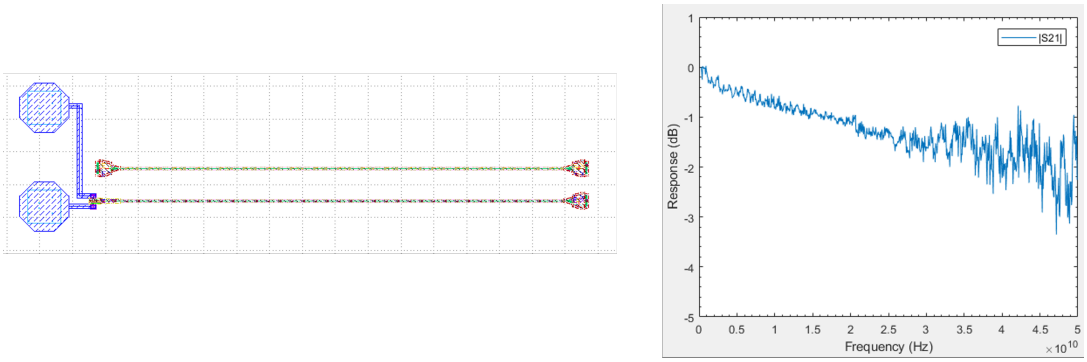

Figure 3.10: Photodetector test structure and bandwidth measurement result

3.3 Stand Alone Receiver PIC Assembly

The receiver PIC assembly was briefly mentioned in Chapter 2. Two assemblies were made: one based on a receiver without polarization recovery section, and the other based on a receiver with polarization recovery section. The layout of the two designs are shown in Fig. 3.11 , with the components labeled. The two designs have a lot of similarities: they both have two edge couplers, one as signal input and the other as LO input; they both have polarization splitter-rotators to separate the polarization of incoming light, and they both have one 90-degree hybrid and four photodetectors for each polarization. The difference between them is that one of them has a polarization recovery section composed of three thermal phase shifter sections, the design of which will be covered in Chapter 6. The waveguide paths from the hybrid to the photodetectors are length matched. The preliminary measurement results from the stand-alone PIC assemblies have already been illustrated in Chapter 2 so it's not repeated here.

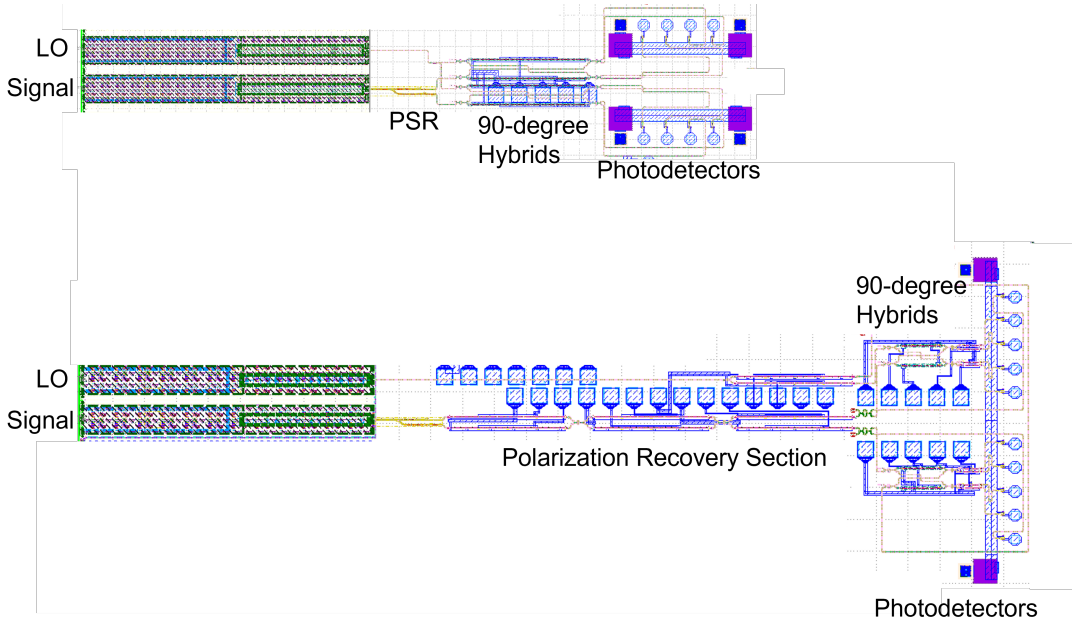

Figure 3.11: Designs of GlobalFoundries receivers on stand-alone assemblies. Upper: receiver without polarization recovery section; Lower: receiver with polarization recovery section; PSR: Polarization Splitter-Rotator

3.4 Integration of PIC with EIC Receiver

3.4.1 General Considerations for Packaging

Since the PIC will be integrated onto the same PCB with the EIC, packaging aspects need to be taken into consideration in the layout process. The anode pads of the photodetectors are laid out at 150 μm pitch to match that of the EIC receiver. The cathodes of the photodetectors are connected together for convenience of biasing. Since the anodes will be wire bonded to the EIC RF inputs, which typically have a DC voltage value higher than 0V, in order to reverse bias the PDs, the common cathode has to be biased at a even higher value. This means the cathode can not be connected directly to the ground. Instead, the bias has to be provided through a voltage supply. For this reason, the PICs have separate ground pads from the common cathode, and a VNCAP is connected in between the ground pads and the common cathode for filtering noise from

the power source. In addition to the on-chip VNCAP, more decoupling capacitors can be added onto the PCB in the assembly process. To reduce the parasitics, the RF pad size needs to be small, but they still need to be wire bondable, so the size is determined with available wire bonding capability taken into consideration.

Another packaging consideration is that in order to shorten the RF wire bond length between the PIC and the EIC, the anode and ground pads need to be placed as close to the edge of the device as possibly allowed by DRC rules placed by the foundry.

3.4.2 Simulation of TIA with PD Equivalent Circuit

When considering integration of photonic components with EICs, it is vital to take into account of the effect of the PIC on the EIC performance by using the equivalent circuit model of the PIC component for co-simulation. Packaging parasitics such as wire bonds inductance and pad capacitance should also be considered to have a more complete understanding of the assembly performance.

For example, simulation in Cadence was conducted using the equivalent circuit of the PDs and the TIA circuit for the assembly in Section 3.6. Fig. 3.12 shows the circuit diagram used for the simulation, with the top circuit diagram showing the PIC-EIC interface. Wire bond inductance, pad capacitance, and output load are also taken into consideration in this circuit diagram.

Fig. 3.13(a) shows the bandwidth simulation result of the TIA itself, with differential AC current source applied directly at the TIA input, and output voltage measured directly from unloaded TIA output. No parasitics have been considered in this simulation. The bandwidth from the simulation is about 30 GHz. Fig. 3.13(b) shows the bandwidth simulation result with the PD circuit model, output load and parasitics taken into consideration. In this case, the bandwidth is reduced to about 19 GHz, and the output voltage

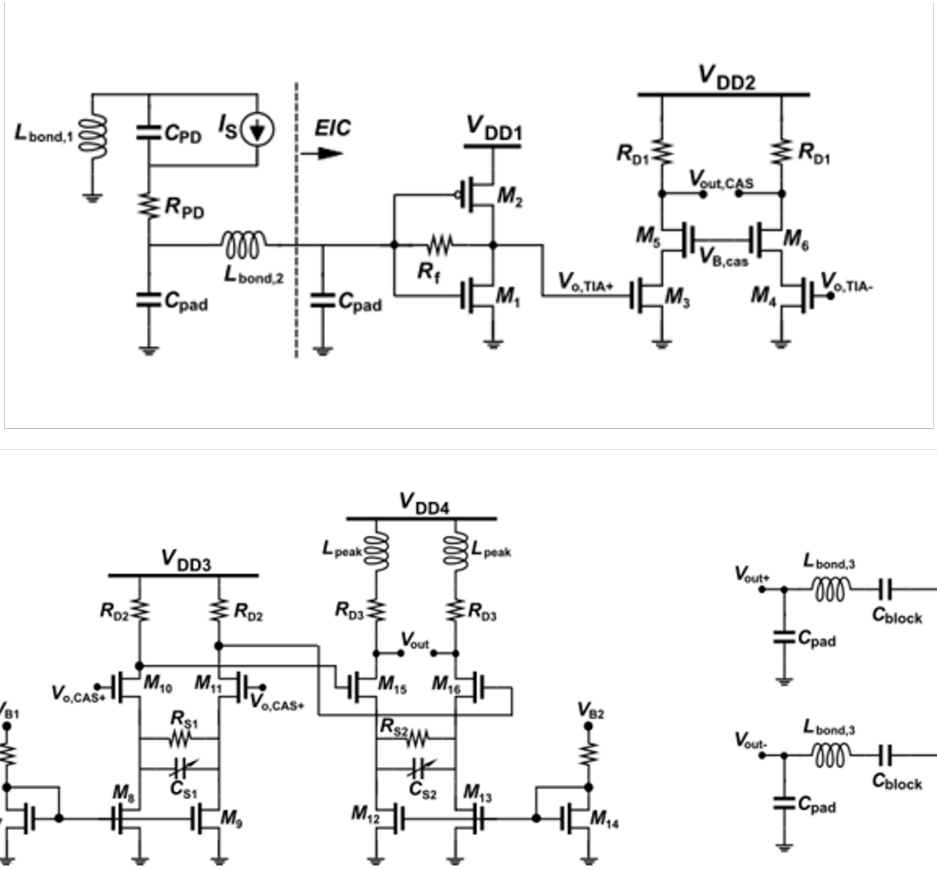

Figure 3.12: Cadence simulation circuit diagram with PD equivalent circuit and TIA, with pad capacitance, wire bond inductance and output load included

level is lower. From the comparison of the simulation results of stand-alone TIA and the results with more realistic factors taken into account, it can be seen that EIC-PIC co-design with parasitics taken into consideration is vital for a more accurate estimation of assembly performance, and can also guide EIC and PIC component design for better performance of the system.

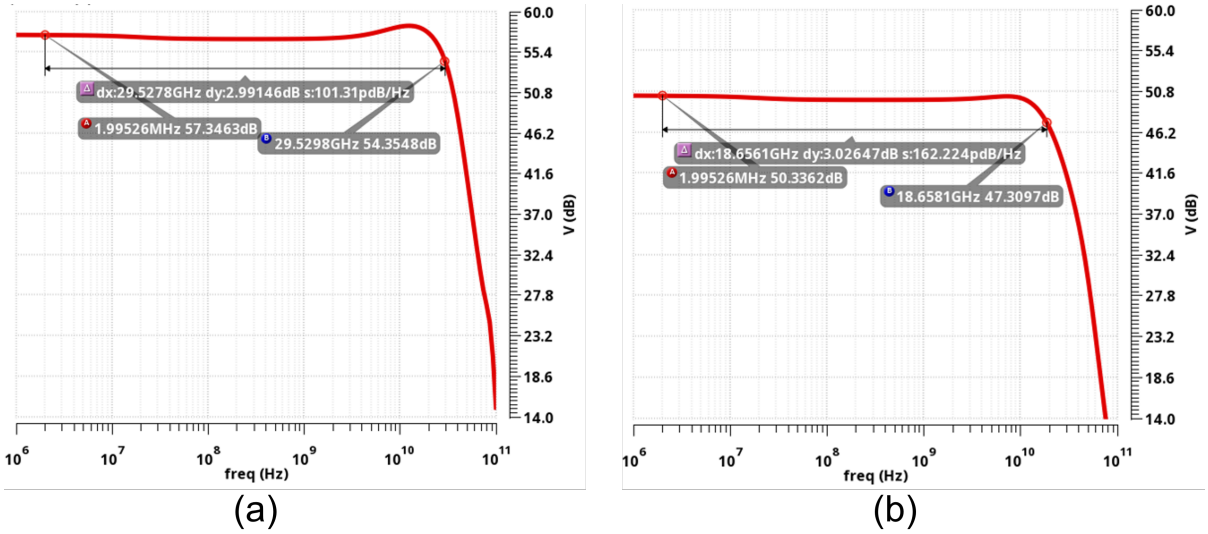

Figure 3.13: Cadence bandwidth simulation result of (a) stand-alone TIA; (b) TIA with PD equivalent circuit, parasitics and load resistance included

3.5 QPSK Coherent Receiver with 8XP EIC

Having developed the measurement setup and procedure, and having verified the functionalities of individual components, we went on to integrate PIC and EIC receivers on a PCB.

Fig. 3.14 shows a picture of the asssembly of the GlobalFoundries 90WG PIC and GlobalFoundries 130 nm SiGe HBT 8XP EIC. The PIC used here is the receiver without polarization recovery section, and Fig. 3.15 shows its microscopic image and schematic. The EIC in the assembly has been demonstrated in [8]. It is composed of a dual-channel RX chain consisting transimpedance amplifiers (TIA), variable gain amplifiers (VGA), and output buffers (OB), as well as a QPSK Costas Loop. Open eyes up to 108 Gb/s have been demonstrated. Because of the setup of the optical coupling of the PIC as well as high speed consideration, some adaptations were made to the PCB. Typically, PICs fabricated by GlobalFoundries are a couple of hundred microns thicker than the EICs, so if the PIC and EIC are placed directly onto the PCB, the wire bond between them

would need to be long enough to compensate for not only the horizontal distance, but also the vertical height difference, which is not ideal for high speed applications. For this reason, we made a recess underneath the PIC using a milling machine, so the top of the PIC and EIC can sit at the same level and the wire bond length can be shortened. Also, a corner of the PCB was removed to give access to fibers for coupling. It is also worth noting that only one polarization of the PIC has been wire bonded to fit into this particular PCB design. The measurement is conducted using the general measurement setup in Chapter 2 with a 50/50 splitter connected to the laser.

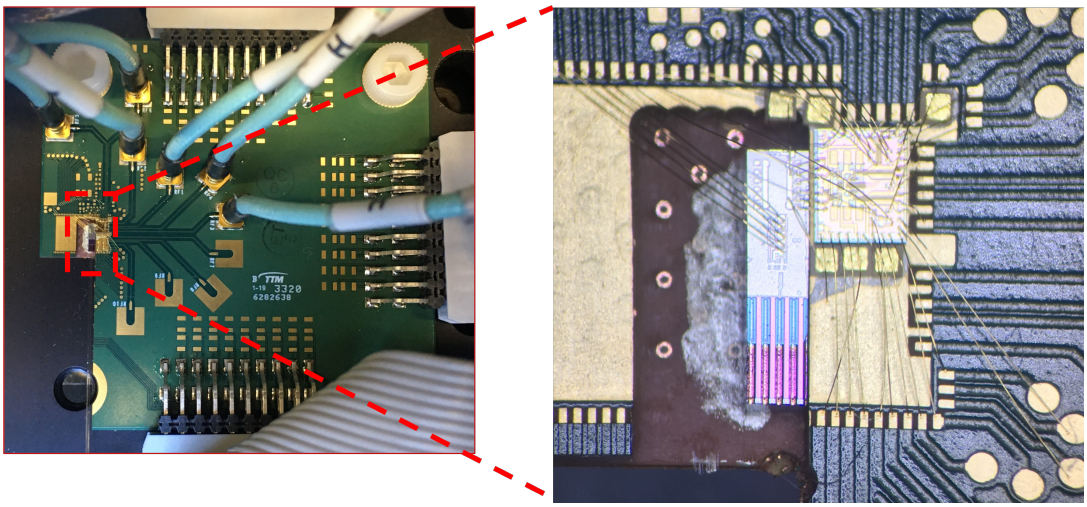

Figure 3.14: Assembly of GlobalFoundries 90WG PIC and 8XP EIC ©2021 IEEE

Fig. 3.16 shows the constellation diagram of the assembly at 56 Gb/s, 80 Gb/s, and 100 Gb/s, where QPSK receiving up to 100 Gb/s has been demonstrated. As mentioned in Chapter 2, here in each constellation diagram, all data points are rotated by the same angle to plot the constellation as the typical orientation, and no other DSP algorithms were used for data processing. The number of bits are chosen so that the measurement result represents a full cycle of PRBS15 signal used for the modulator. The BER values are obtained by directly counting the number of errors divided by the total number of bits being transmitted, and the details are discussed in Chapter 2. At 100 Gb/s the BER

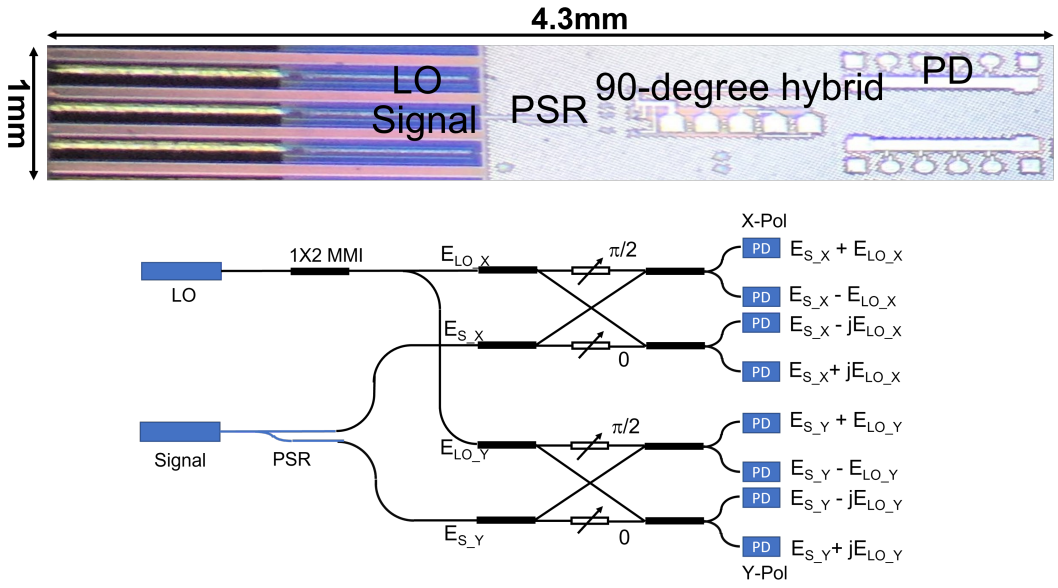

Figure 3.15: Microscopic image and schematic of GlobalFoundries 90WG receiver

value is 6.8×10^{-5}, which is below the KP4-FEC BER limit (2.2×10^{-4}).

It is also worth noting that for measurement above 80 Gb/s, 2-tap feed-forward equalization (FFE) is used on the PRBS signals modulating the commercial transmitter to help overcome its bandwidth limitation (25 GHz). A feed-forward equalizer is a system whose output is the sum of a set of input signals which are appropriately delayed and weighted by the tap coefficients:

$$out(t) = \sum_{n=1}^{N} C_n \times s[t - (n-1)T] \tag{3.21}$$

where $out(t)$ and $s(t)$ are the equalizer output and input signal respectively, $C_n (n = 1, 2...N)$ are the tap coefficients, T is the tap delay and N is the number of taps. Fig. 3.17 shows the schematic of the FFE system [9] and an example of using FFE on PRBS signal, which is what has been used in the measurement of the coherent receiver.

In the measurement setup, the FFE concept is realized by using two independent PRBS channels to generate modulation signal for one RF input of the commercial mod-

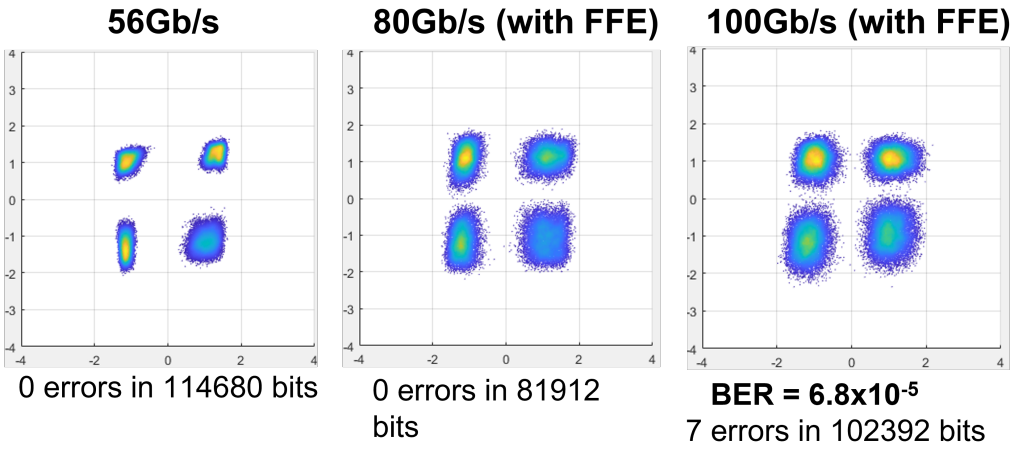

Figure 3.16: Constellation diagrams at 56 Gb/s, 80 Gb/s and 100 Gb/s for 90WG PIC-8XP EIC assembly

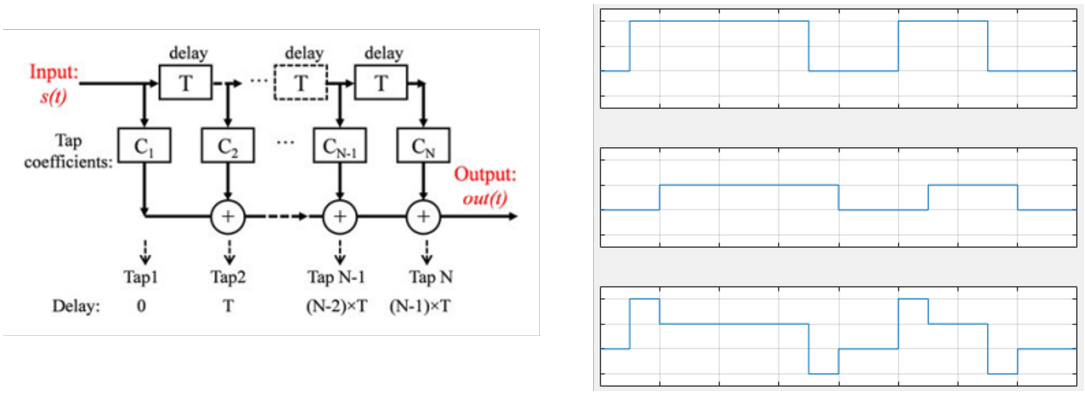

Figure 3.17: Left: schematic of FFE system; Right: an example of FFE on PRBS signal

ulator. In each PRBS pair, one of the channels is inverted and set up to have a lower amplitude and a certain amount of delay compared with the other one. Then the pair goes through a RF combiner, and the combined output goes into the RF input of the modulator.

In the 90WG PIC-8XP EIC assembly, 100 Gb/s operation below the KP4-FEC BER limit has been demonstrated, and the work has been published in [10]. We improved the BER calculation method and acquired improved results after the time of publication, so the plots in the paper look different than the ones displayed here.

The energy consumption of the EIC, including the receiver chain and OPLL, is 534 mW; the two RX channels consume 332 mW without the OPLL. So for 100 Gb/s operation, the energy efficiency is 3.32 pJ/bit [11].

3.6 QPSK Coherent Receiver with 45 nm CMOS EIC

With the same 90WG photonic receiver, another assembly is made with an EIC fabricated in the GlobalFoundries 45RF-SOI 45 nm CMOS process. Fig. 3.18 shows a picture of the assembly, and Fig. 3.19 shows two examples of constellation diagrams at 40 GBaud and 50 GBaud, both with FFE applied to the commercial Mach-Zehnder modulator, as well as BER vs OMA for various data rates. The assembly performance and the circuit design is explained in more detail in [12]. It is worth noting that only one polarization is demonstrated in this paper.

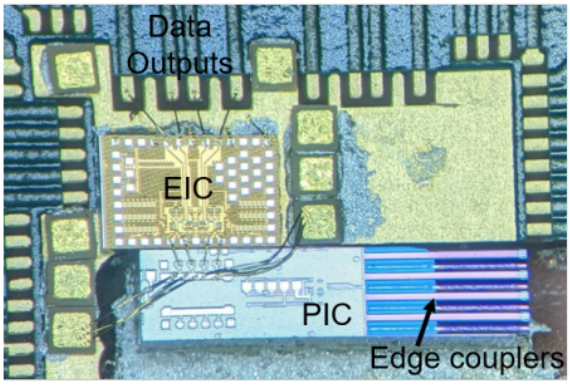

Figure 3.18: Assembly of GlobalFoundries 90WG PIC and 45 nm EIC ©2021 IEEE

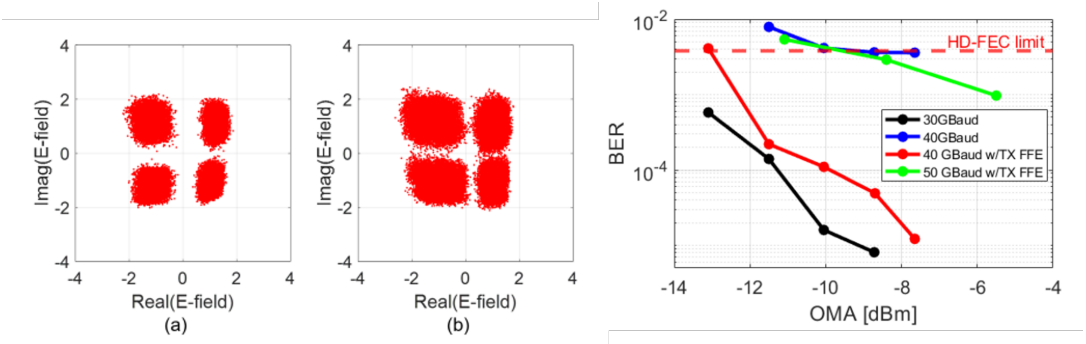

Figure 3.19: Examples of constellation diagrams at (a) 40 GBaud and (b) 50 GBaud, and BER vs OMA at various data rates ©2021 IEEE

3.7 Conclusion

In this chapter, the performance of different variations of receiver assemblies based on GlobalFoundries PIC and EIC is presented. A brief introduction of the GlobalFoundries 90WG platform is given, followed by measurement and characterization results from single components to the whole coherent assembly. The assemblies are capable of 100 Gb/s of data rate per polarization with BER lower than KP4-FEC or HD-FEC BER limits. When both polarizations are utilized, we can expect the data rate to double. High-speed photodetectors on the PIC, high-speed EICs, and short wire bond lengths for RF paths are all very important factors for high data rate performance.

By comparing the measurement results of assemblies utilizing 8XP EIC and 45 nm CMOS EIC, we can see that the 8XP platform has the advantage of higher speed. The 45 nm CMOS technology, however, is more energy efficient, as will be shown in Chapter 4.

Bibliography

[1] K. Giewont, K. Nummy, F. A. Anderson, J. Ayala, T. Barwicz, Y. Bian, K. K. Dezfulian, D. M. Gill, T. Houghton, S. Hu, B. Peng, M. Rakowski, S. Rauch, J. C. Rosenberg, A. Sahin, I. Stobert, and A. Stricker, *300-mm Monolithic Silicon Photonics Foundry Technology*, *IEEE Journal of Selected Topics in Quantum Electronics* **25** (2019), no. 5 1–11.

[2] T. Barwicz, A. Janta-Polczynski, M. Khater, Y. Thibodeau, R. Leidy, J. Maling, S. Martel, S. Engelmann, J. S. Orcutt, P. Fortier, and W. M. J. Green, *An o-band metamaterial converter interfacing standard optical fibers to silicon nanophotonic waveguides*, in *2015 Optical Fiber Communications Conference and Exhibition (OFC)*, pp. 1–3, 2015.

[3] W. D. Sacher, B. Peng, J. C. Rosenberg, M. Khater, Y. Martin, J. S. Orcutt, Y. A. Vlasov, W. M. J. Green, and T. Barwicz, *An o-band polarization splitter-rotator in a cmos-integrated silicon photonics platform*, in *Frontiers in Optics 2016*, p. FTu2D.2, Optica Publishing Group, 2016.

[4] M. Seimetz and C.-M. Weinert, *Options, feasibility, and availability of 2 × 4 90° hybrids for coherent optical systems*, *J. Lightwave Technol.* **24** (Mar, 2006) 1317.

[5] L. Soldano and E. Pennings, *Optical multi-mode interference devices based on*

self-imaging: principles and applications, *Journal of Lightwave Technology* **13** (1995), no. 4 615–627.

[6] M. Bachmann, P. A. Besse, and H. Melchior, *General self-imaging properties in n × n multimode interference couplers including phase relations*, *Appl. Opt.* **33** (Jun, 1994) 3905–3911.

[7] L. Zimmermann, K. Voigt, G. Winzer, K. Petermann, and C. M. Weinert, *c -band optical 90° -hybrids based on silicon-on-insulator 4 × 4 waveguide couplers*, *IEEE Photonics Technology Letters* **21** (2009), no. 3 143–145.

[8] L. A. Valenzuela, A. Maharry, H. Andrade, C. L. Schow, and J. F. Buckwalter, *A 108-gbps, 162-mw cherry-hooper transimpedance amplifier*, in *2020 IEEE BiCMOS and Compound Semiconductor Integrated Circuits and Technology Symposium (BCICTS)*, pp. 1–4, 2020.

[9] X. Li, N. Bamiedakis, X. Guo, J. J. D. McKendry, E. Xie, R. Ferreira, E. Gu, M. D. Dawson, R. V. Penty, and I. H. White, *Wireless visible light communications employing feed-forward pre-equalization and pam-4 modulation*, *Journal of Lightwave Technology* **34** (2016), no. 8 2049–2055.

[10] Y. Xia, L. Valenzuela, A. Maharry, S. Pinna, S. Dwivedi, T. Hirokawa, J. Buckwalter, and C. Schow, *A fully integrated o-band coherent optical receiver operating up to 80 gb/s*, in *2021 IEEE Photonics Conference (IPC)*, pp. 1–2, 2021.

[11] L. A. Valenzuela, Y. Xia, A. Maharry, H. Andrade, C. L. Schow, and J. F. Buckwalter, *A 50-gbaud qpsk optical receiver with a phase/frequency detector for energy-efficient intra-data center interconnects*, *IEEE Open Journal of the Solid-State Circuits Society* **2** (2022) 50–60.

[12] H. Andrade, Y. Xia, A. Maharry, L. Valenzuela, J. F. Buckwalter, and C. L. Schow, *50 gbaud qpsk 0.98 pj/bit receiver in 45 nm cmos and 90 nm silicon photonics*, in *2021 European Conference on Optical Communication (ECOC)*, pp. 1–4, 2021.

Chapter 4

Coherent Receiver Based on Rockley Photonics Multi-Micron SiP Platform

In this chapter, photonic receiver design based on the multi-micron silicon photonics platform developed by Rockley Photonics is discussed. Firstly, a brief introduction of the Rockley Photonics multi-micron SiP platform is provided; then information on the 4×4 MMI design is given, followed by details on the EIC-PIC assembly and measurement results. In the end, there is a summary of the advantages and differences of the two SiP platforms utilized for the photonics receivers described in the dissertation.

4.1 Rockley Photonics Multi-Micron SiP Platform

Unlike most of the sub-micron silicon photonic platforms currently available, the Rockley Photonics platform has a much larger dimension with height higher than 1 μm, as can be seen in Fig. 4.1(a) . A couple of advantages come with the larger waveguide di-

mension, such as low propagation loss, low coupling loss, high power handling and higher tolerance to fabrication variations. The platform has propagation losses much lower than sub-micron waveguides, with 0.18 dB/cm loss for rib waveguides and 0.31 dB/cm loss for strip waveguides. For sub-micron silicon photonic platforms, the loss for strip waveguides is typically around 1.5 dB/cm. In high volume production, the theoretical loss of the fiber attach can be < 1 dB per interface. The platform also offers integration with III-V components and Ge photodetectors [1]. Fig. 4.1(c) shows reflective SOA gain chip edge coupled to the SiP chip and the gratings on the SiP chip [2]; and Fig. 4.1(b) shows EAMs integrated on the SiP chip. Polarization independence is another distinct feature of the platform. It may not be an advantage for our particular measurement, but it can be an advantage for certain applications such as photonic switches.

4.2 Receiver Design

Similar to Chapter 3, two configurations of photonic receivers are designed: one based on 3-dB couplers and phase shifters, and the other based on a 4×4 MMI. The configuration based on 3-dB couplers and phase shifters is similar to that in Chapter 3 so it will not be discussed here.

4.2.1 Design of 4×4 MMI

The first step for designing a 4×4 MMI is to pick an appropriate width which supports enough number of modes, and is compatible with the taper widths and separations of the input and output waveguides. Then the L_π can be calculated by Eq. 3.15, and for our application, the length of multimode section of the 4×4 MMI can be calculated by Eq. 3.16, where $M = 1$ and $N = 4$.

After calculating the dimensions as a starting point, Lumerical simulation software

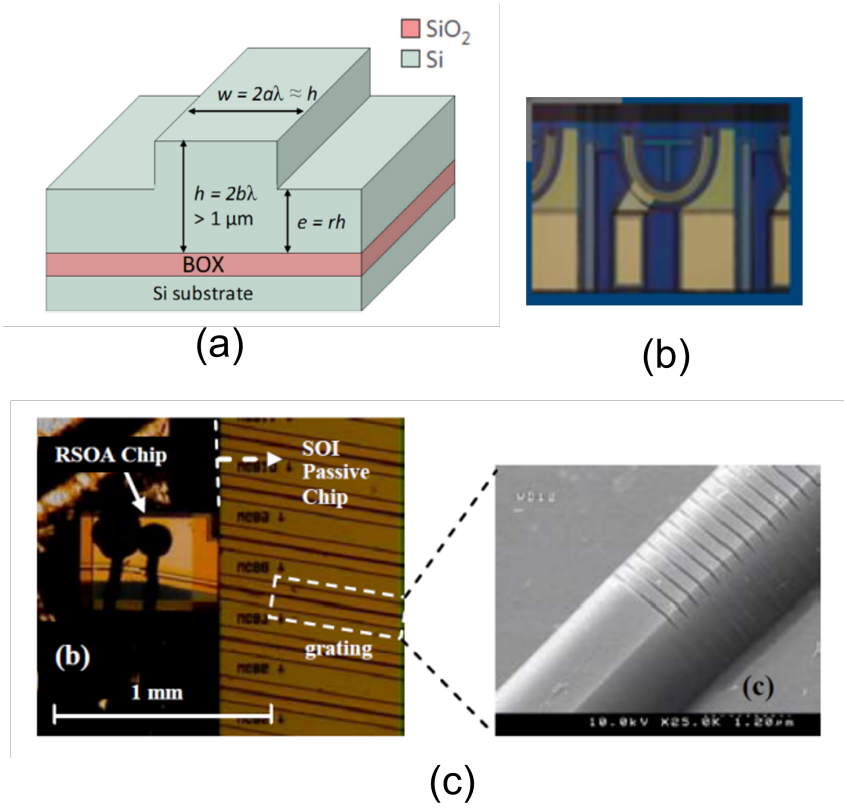

Figure 4.1: (a) Cross section of Rockley Photonics platform waveguide ©2019 IEEE; (b) EAM integration on Rockley Photonics platform; (c) SOA integration on Rockley Photonics platform

is used for optimization of taper separation and multimode section length. The figure of merits for optimization are power imbalance for the output ports, the insertion loss, and the phase relation. The real time oscilloscope available at this point only has two inputs, so data from only one of the I outputs and one of the Q outputs will be processed. For this reason, the power imbalance with the I-s and Q-s will not show up in the measurement result, and the power imbalance in between I and Q can be compensated easily by normalizing the data after acquisition. For those reasons, the phase relation is the more important factor to be optimized.

Fig. 4.2 shows the simulated mode profile of the 4×4 MMI with optimized parameters. Based on Table 3.1, when ports 1 and 3 are used as input ports, the phase increments of

input 3 relative to input 1 at each output port are equal to $-45°$, $225°$, $45°$ and $-225°$. And the simulated angles are $-44.92°$, $225.33°$, $45.01°$ and $-224.94°$, so the maximum phase error is $0.33°$.

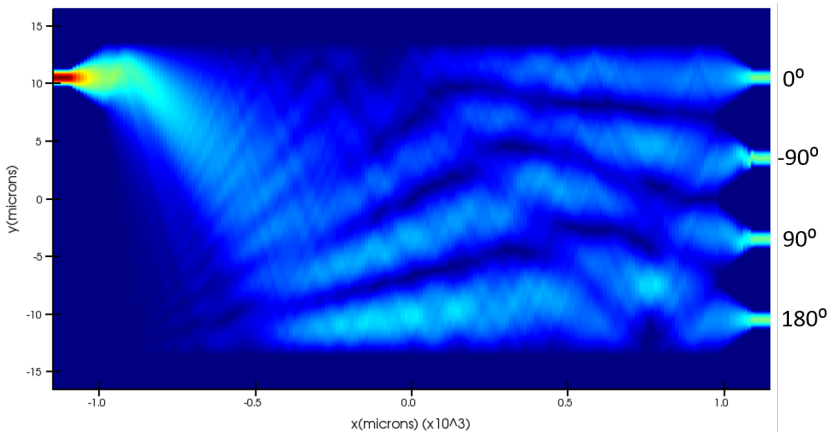

Figure 4.2: Simulated mode profile of 4×4 MMI

To characterize the excess loss and power imbalance of the 4×4 MMI, we can define excess loss as

$$EL = -10 \log \frac{\sum P_i}{P_{in}} \tag{4.1}$$

and power imbalance as

$$PI = -10 \log \frac{\min(P_i)}{\max(P_i)} \tag{4.2}$$

Based on the definition, the simulated excess loss is 0.12 dB, and the power imbalance is 0.2 dB.

4.2.2 Test Structures

Similar to Chapter 3, on the Rockley receiver tapeout, there are test structures of 4×4 MMIs for phase relation verification, and test structures for the thermal phase shifter for tuning efficiency characterization. Although the receiver PIC used for the assembly is one based on 4×4 MMI, the layout also includes a receiver based on power

splitters/combiners and thermal phase shifters, as well as its test structure. For this receiver design, we matched all the four path lengths in the 90-degree hybrid to make the FSR at the four outputs of the test structure as close as possible, so that its phase relation can be characterized. In addition, there is a stand-alone PD test structure for responsivity and bandwidth measurement.

4.3 QPSK Coherent Receiver with 45 nm CMOS EIC

Fig. 4.3 shows the Rockley receiver PIC with fiber attach, with the inset showing a microscope image of the PIC. The receiver is composed of 4×4 MMI as the 90-degree hybrid and quad photodetectors (PD) for detection, and the waveguide routing between the MMI and the PDs are length matched. Waveguide crossings are used so that the I and I' outputs are placed next to each other, so are Q and Q' outputs. Two edge couplers work as signal and local oscillator (LO) inputs of the receiver, and have low-loss fiber attach for packaging and ease of characterization. The fiber is epoxy attached using butt-coupled high-NA fibers to the edge coupler on these shuttle-run PICs. In the full Rockley volume process, similar or lower fiber attach losses are achieved when the PIC is directly coupled to a SMF fiber[1]. No post fabrication trimming or tuning power was required to operate the photonic receiver.

The EIC is the same one as presented in the assembly in Section 3.6. It is fabricated in GlobalFoundries 45 nm RFSOI process, and consists of a transimpedance amplifier (TIA), a cascode amplifier (CAS), a cascade of limiting amplifiers (LA), and an output buffer (OB). The simulated post-layout 3 dB bandwidth assuming a 40 GHz PD bandwidth, with wire bond inductance and bondpad capacitance included, is 23 GHz [3]. The CMOS-

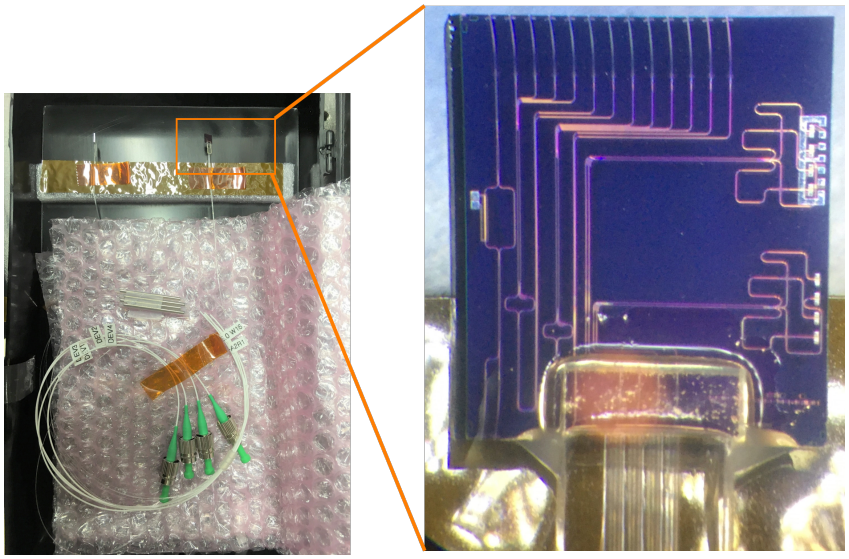

Figure 4.3: PIC with fiber attach

based electronics have a significant power efficiency advantage.

Fig. 4.4 shows the PIC and the EIC assembled on a test platform that has demonstrated operation up to 108 Gb/s [4]. Bypassing capacitors were added to TIA supplies and PD cathodes. The PD anodes are wire-bonded to the inputs of the EIC, and the EIC outputs are wire-bonded to the high-speed traces on the PCB. Data outputs are connected to real time oscilloscope through mini-SMP connectors and RF cables. The EIC dimensions are 1.88 mm x 1.28 mm. The size of the photonic chip is 5.5 mm x 4.7 mm, however, the receiver itself only occupies 3 mm x 2.7 mm. Similar to the GlobalFoundries assemblies, a recess is made under the Rockley PIC so that the top of the two chips can be at the same level and the wire bond lengths between them can be shortened. A block diagram of the receiver is shown in Fig. 4.5.

One of the challenges we faced with when building the assembly with the fiber attached Rockley PIC is the temperature sensitivity of the fiber attach unit. It is not recommended to apply higher than 100 ℃ onto the fiber attach unit; however, the solder we have been using to attach the RF connectors and DC headers needs to be cured at

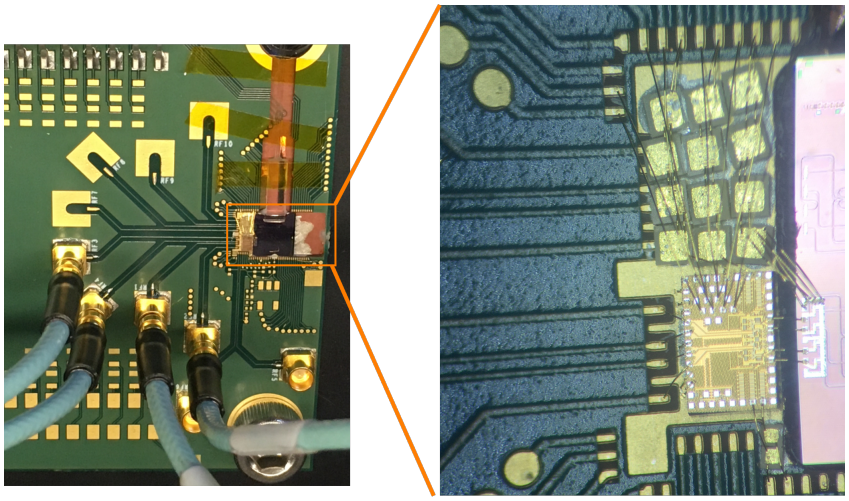

Figure 4.4: PCB assembly of Rockley Receiver and 45 nm EIC

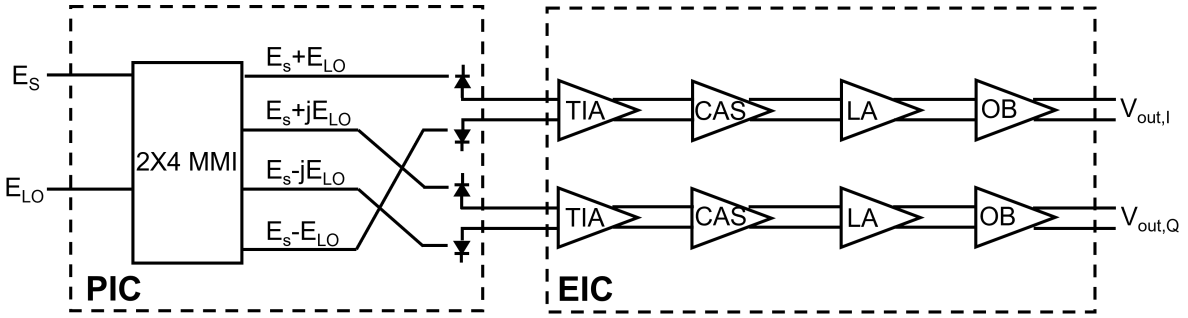

Figure 4.5: Block diagram of the receiver

165 ℃. In addition, we have been using silver epoxy at 165 ℃ to attach the chips to the PCB, and the previous wire bond recipes are all at 165 ℃. In order to keep the temperature on the fiber attach unit below 100 ℃, we have developed low-temperature wire bonding recipes, and we have also lowered the curing temperature of the epoxy and extended the curing time (80 ℃ for 3 hours). And since the soldering step can not be skipped or modified to be done at a lower temperature, we changed the order of the steps for building an assembly. Typically, the chips and decoupling capacitors need to be attached onto the PCB with epoxy as the first step. Then the wire bonding is done, and attaching the RF connectors and DC headers is the final step. The advantage of building

the assembly in this sequence is that RF and DC connectors will not be in the way when doing the wire bonding. However, doing this would expose the fiber attach unit to high temperature. So for the assemblies with fiber attach unit, the first step is to solder the connectors. Then the chips are attached to the PCB using epoxy at low temperature; and the last step is to wire bond using low temperature recipe. This sometimes poses challenges for the wire bonding process because the headers may get in the way for some wire bonding tools, but we have been able to move on by using different tools.

The block diagram of the self-homodyne measurement setup is illustrated in Fig. 4.6. The light from an external cavity laser (ECL) set at 1310 nm is split into two paths by a 50/50 splitter. One path goes through a polarization controller (PC), then to the LO port on the PIC; the other goes into a PC followed by a $LiNbO_3$ I-Q modulator (iXblue MXIQER-LN-30), a semiconductor optical amplifier (SOA), and a PC before being coupled into the signal port of the PIC. Two streams of PRBS15 pattern decorrelated by bit delay are amplified and used to drive the I- and Q-inputs of the modulator that is configured for QPSK modulation.

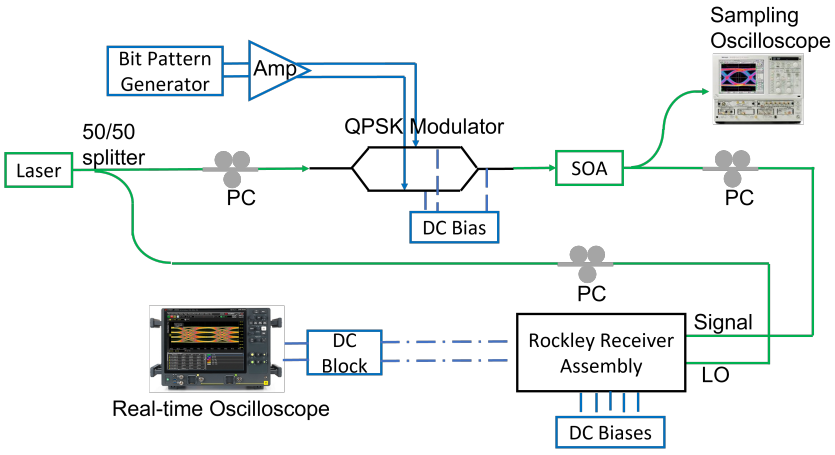

Figure 4.6: Rockley receiver measurement setup

The MATLAB script described in Chapter 2 is used for remote control of the real-

time oscilloscope and data processing. Data from the I- and Q-channels of the assembly are captured through the single-ended outputs of the receiver chains, and constellation diagrams are generated with data from I- and Q- channel plotted on the X and Y axis, respectively. In addition, at each acquisition, all data points are rotated by an angle optimized for the particular set of data for QPSK constellation plotting. Constellation diagrams are constructed using at least 32800 symbols, representing a full cycle of the PRBS15 pattern. BER values are calculated by comparing received bits with transmitted bits, and directly counting the number of errors, divided by the total number of bits. When calculating BER, the threshold for assigning received voltage values to 1 and 0 is optimized for each acquisition to obtain minimum BER values. The threshold value is fixed for all data points in the same acquisition.

In Fig. 4.7, the BER values for 64 Gb/s, 80 Gb/s and 100 Gb/s are plotted against different signal power at the signal input fiber of the PIC, and the insets show examples of the constellation diagrams at 80 Gb/s and 100 Gb/s. Above 80 Gb/s, a feed-forward equalization (FFE) technique was used at the RF input of the modulator to help overcome its bandwidth limitation (25 GHz). The receiver operates below the HD-FEC BER limit at 100 Gb/s at -6.63 dBm signal power, and below the KP4-FEC BER limit at 80 Gb/s at lower than -12.8 dBm signal power. For all the data points in the figure, the LO power is set to 7.8 dBm.

We define effective responsivity as the ratio of the total photocurrent in the four PDs to the optical power at the input fiber of the PIC. By this definition, the effective responsivity takes into account the coupling loss, the propagation loss of the PIC, as well as the PD responsivity itself, and it represents the efficiency of the receiver in terms of converting input power to photocurrent. The effective responsivity is estimated from this measurement to be 0.5 A/W, which demonstrates the low coupling and propagation losses of the Rockley Photonics fabrication platform. Assuming 1 A/W of photodetector

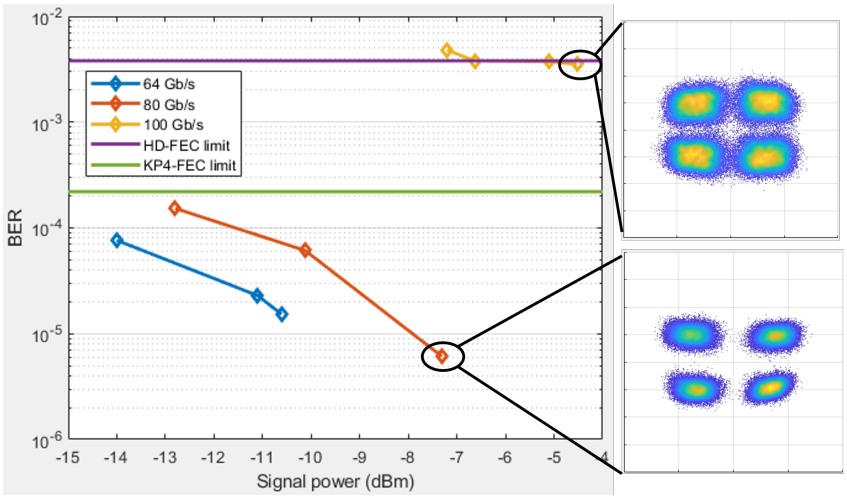

Figure 4.7: Sensitivity curves and constellation

responsivity, 0.5 A/W effective responsivity means the total loss from the PIC input to the PD is only 3 dB.

The measured power consumption of the EIC is 98 mW, or 0.98 pJ/bit for 100 Gb/s data. The receiver PIC utilizes MMI as the 90-degree hybrid and consumes no tuning power.

4.4 Comparison of Receivers on the Two Different SiP Platforms

This chapter and Chapter 3 show demonstrations of EIC-PIC coherent receivers based on two different silicon photonic platforms: GlobalFoundries' sub-micron silicon photonic platform and Rockley Photonic's multi-micron silicon photonic platform. From the performance stand point, the GlobalFoundries 90WG platform offers high speed photodetectors and provides polarization multiplexing functionalities and components; however, it is hard to optimize the coupling loss from external laser into the edge coupler, and high laser power is needed to compensate for the loss. On the other hand, as a platform

which is distinctively different from most of the sub-micron silicon photonic platforms, the Rockley Photonics multi-micron photonics platform offers a lot of advantages for coherent link application, including low propagation loss and low coupling loss. However, its polarization independent property makes it a challenge to utilize the polarization diversity aspect of coherent technology.

Although it is not obvious in the measurement results or fabricated PICs, some aspects of the two platforms can affect the flexibility in the design, layout and packaging process. One of them is the size of the components. For the Rockley Photonics platform, since the waveguide dimension is larger, all the waveguide components also have significantly larger size compared with those in the GlobalFoundries process. For example, length of a 4×4 MMI in the Rockley Photonics platform is on the order of millimeters, almost 10 times the size of 4×4 MMIs on the sub-micron SiP platforms. Such large size can make it difficult to lay out a full PIC in a space efficient way on a typical die size of a couple of millimeters. This not only makes it more difficult to modify the layout when changes are needed, but can also make packaging activities less efficient, since it may be difficult to dice out separate PICs because of the way they are laid out. Also, Rockley Photonics platform has limited number of metal layers and routing capability, and this can add to challenges in the wire bonding process, since DC pads have to be placed close to the components being biased instead of being routed to a certain area for easy wire bonding. In summary, the Rockley Photonics platform has significant advantage in its low loss aspect; however, it requires a lot more special handling and customization compared with the GlobalFoundries SiP platform.

Bibliography

[1] A. J. Zilkie, P. Srinivasan, A. Trita, T. Schrans, G. Yu, J. Byrd, D. A. Nelson, K. Muth, D. Lerose, M. Alalusi, *et. al.*, *Multi-micron silicon photonics platform for highly manufacturable and versatile photonic integrated circuits*, *IEEE Journal of Selected Topics in Quantum Electronics* **25** (2019), no. 5 1–13.

[2] A. J. Zilkie, P. Seddighian, B. J. Bijlani, W. Qian, D. C. Lee, S. Fathololoumi, J. Fong, R. Shafiiha, D. Feng, B. J. Luff, X. Zheng, J. E. Cunningham, A. V. Krishnamoorthy, and M. Asghari, *Power-efficient iii-v/silicon external cavity dbr lasers*, *Opt. Express* **20** (Oct, 2012) 23456–23462.

[3] H. Andrade, Y. Xia, A. Maharry, L. Valenzuela, J. F. Buckwalter, and C. L. Schow, *50 gbaud qpsk 0.98 pj/bit receiver in 45 nm cmos and 90 nm silicon photonics*, in *2021 European Conference on Optical Communication (ECOC)*, pp. 1–4, 2021.

[4] A. Maharry, L. A. Valenzuela, J. F. Buckwalter, and C. L. Schow, *A pcb packaging platform enabling 100+ gbaud optoelectronic device testing*, in *2021 IEEE 71st Electronic Components and Technology Conference (ECTC)*, pp. 1323–1328, 2021.

Chapter 5

EAM-based QPSK Transmitter

In this chapter, the operation principle of EAM-based QPSK modulator is explained, followed by an analysis of the challenges for measurements. Then single EAM operation and preliminary QPSK measurement attempts are shown with a stand-alone PIC assembly. Afterwards, the process of EIC-PIC transmitter assembly optimization is discussed. With the EIC-PIC assembly, QPSK constellations at different data rates are generated, and the transmitter operates below the HD-FEC BER limit up to 56 Gb/s, and below the SD-FEC BER limit up to 64 Gb/s. Link operation is also accomplished with the transmitter and the Rockley receiver presented in Chapter 4. The link also operates below the HD-FEC BER limit up to 56 Gb/s, and below the SD-FEC BER limit up to 64 Gb/s.

5.1 EAM-based QPSK Modulator

The concept and experiment result of EAM-based QPSK modulator is first explained in Doerr's paper [1]. The device is based on InP platform, and is made up of star couplers and EAMs. Fig. 5.1 shows the schematic of the modulator, and Fig. 5.2 shows

the generation of the QPSK constellation. The center arm acts as a DC level offset, and the upper arm and lower arm are modulated by RF signals. By adjusting the power ratio and the phase relation of the three arms to appropriate levels, the four points on the QPSK constellation can be constructed by on-off modulation of the two EAMs. In order to adjust the phase shift, the device has phase shifters on the three arms. The desired power ratio is obtained through design of the star couplers.

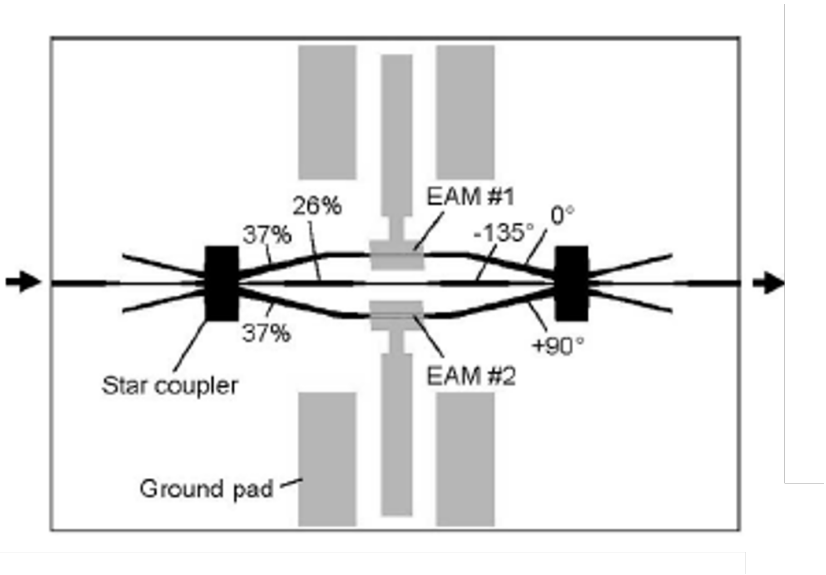

Figure 5.1: Schematic of EAM-based QPSK modulator ©2007 IEEE

The device performance is demonstrated at 1540 nm using a Mach-Zehnder delay interferometer (MZDI). 21.4 Gb/s DQPSK result is demonstrated, and preliminary measurement results at 107 Gb/s are given.

In [2], a PIC with similar working principle is presented. This paper demonstrates a C-band QPSK modulator based on rings, with the same concept where two RF devices act as intensity modulators and the third path acts as a DC path to move the constellation to the origin, which in this device is achieved by a variable optical attenuator (VOA). Device performance is shown at 24 Gb/s data rate and 1550.25 nm wavelength. Unlike [1], the measurement setup utilizes the self-homodyne scheme and a coherent receiver

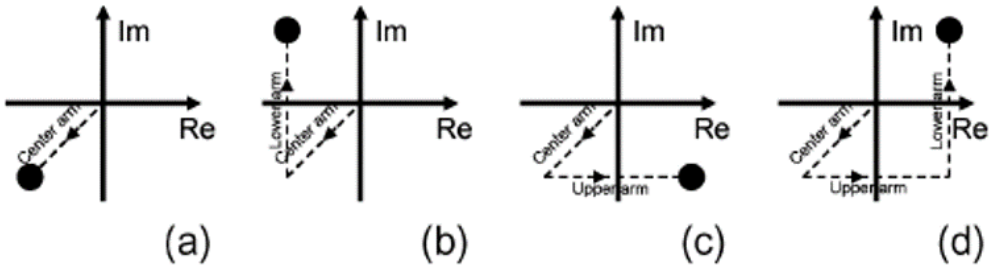

Figure 5.2: Generation of QPSK constellation ©2007 IEEE

is used for demodulation. The data is processed offline with DSP algorithms and the constellation diagram is recovered.

The most common way of generating a QPSK signal is based on the combination of two 90-degree shifted BPSK signals. There are various ways of generating BPSK signal and achieving 90° phase shift, and a very typical way is to use nested Mach-Zehnder structures [3]. The two sub-MZIs each require a phase shifter for adjusting the biases to BPSK modulation point, and another phase shifter is needed to obtain 90° phase offset between the two sub-MZIs. Compared with the explanation in Fig. 5.2, it is obvious that the EAM-based QPSK modulator generates the QPSK signal using a completely different method.

The EAM-based QPSK modulator has a couple of advantages. The III-V EAMs have a compact size, on the order of 100 μm, whereas the length of a Mach-Zehnder modulator is typically a couple of millimeters. This means EAMs can be operated as lumped elements, which greatly simplifies design and fabrication. Also, EAMs usually require a lower modulation RF swing compared with Mach-Zehnder modulators, and this advantage can potentially lead to better power efficiency. These advantages of EAMs give rise to its application in other modulation formats as well. An example is presented in [4], where a 100 Gb/s PAM-4 C-band transmitter is demonstrated on the Rockley Photonics platform, with two uneven lengths EAMs in an unbalanced MZI.

However, Mach-Zehnder based QPSK modulators also have advantages which make them still more commonly available than the EAM-based ones. One thing that stands out during the measurements process is that it is much easier to find the operation point for Mach-Zehnder modulators. This will be explained in more detail in Section 5.3.1.

5.2 Transmitter Design

Our design of EAM-based QPSK transmitter is based on Rockley Photonics SiP platform, integrated with III-V EAMs. Fig. 5.3 shows a schematic of our device design. We have one additional EAM in the center path, which acts as a DC EAM for more flexibility of power ratio control. Instead of using star couplers, we used 1×3 MMI at the input and 3×3 MMI at the output for more reliability in fabrication, since it is our first time utilizing the technology. There are two phase shifters in each path to ensure a full 2π phase shift range in all the paths.

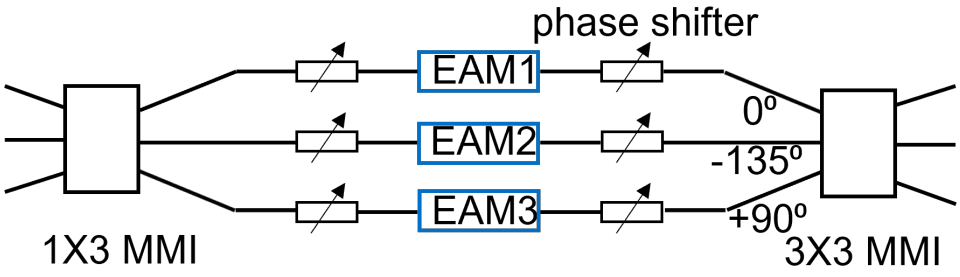

Figure 5.3: Transmitter schematic

5.2.1 MMI Design

The MMI design method is the same as mentioned in Chapter 3. Technically, we need only one input and one output. However, 3×3 MMI is needed at the output to avoid reflection problems. Since MMIs are not typically designed to reach uneven

splitting ratio, the optimization process still focuses on minimizing power imbalance at the outputs and minimizing excess loss as usual, and the power ratio adjustment will be done using the DC EAM. The simulated field profiles of 1×3 MMI and 3×3 MMI are shown in Fig. 5.4.

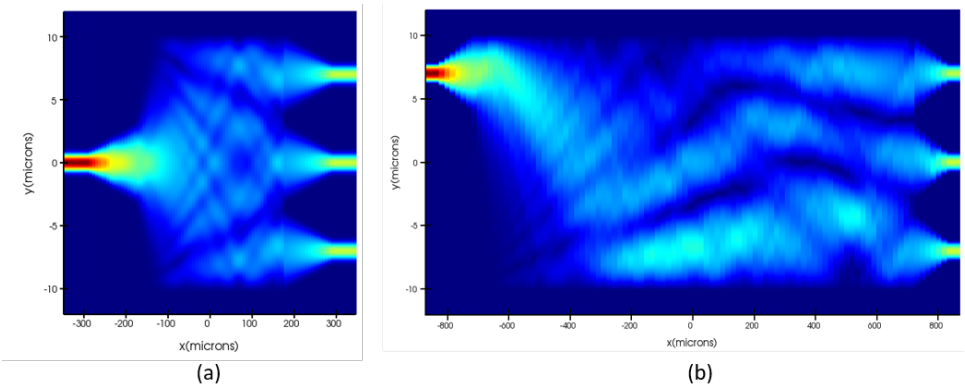

Figure 5.4: Simulated field profile of 1×3 and 3×3 MMI

For the 3×3 MMIs, we have two designs with different lengths. The shorter 3×3 MMI has practically the same dimensions as the 1×3 MMI, with two additional inputs. Simulation results show that in this case, the upper and lower output will have lower output power compared with the center output. But this is not a problem for our application, since only one output is needed, and power balance at the transmitter output is not required. The longer version of the 3×3 MMI, based on Eq. 3.16, has four times the length of the 1×3 MMI, and has equal amount of power at all three outputs.

5.2.2 Test Structures

On the Rockley transmitter tapeout, there are also test structures for the 1×3 MMI and 3×3 MMIs. Ideally, the 3×3 MMI test structures should be able to provide test results for power splitting ratio as well as phase relation; however, as a result of space limit, most of the 3×3 MMI test structures can only provide splitting ratio test results.

Since there are phase shifters in each path, the phase relation of MMI outputs does not need to be accurate, so this missing aspect of the test structures does not affect the transmitter measurement. Similar to the receivers discussed in Chapter 4, there is also a test structure for phase shifter efficiency. A stand-alone EAM test structure is designed with an imbalanced MZI to characterize the phase shift of the EAM at different biases. There is also a test structure for a star coupler, which will be discussed in Section 6.2.4.

5.3 Measurement Challenges

5.3.1 Difficulty in Tuning Compared with MZM-based Modulator

The major challenge in the characterization of the EAM-based transmitter is the difficulty in finding the appropriate biasing points for the EAMs and phase shifters as a result of the design of the structure and QPSK generation mechanism. For MZM-based QPSK modulators, only three phase shifters need to be tuned, and the process is well defined and relatively straightforward, and it is easy to check the two BPSK signals individually and adjust the three phase shifters separately. In addition, the three phase shifters can be adjusted independently from each other. It is more difficult to find the biasing points of EAM-based QPSK modulators. More parameters need to be tuned, including biases of the three EAMs and at least two phase shifters. For the EAM biases, unlike the sub-MZIs which need to be biased at minimum transmission power, there are no well-defined rules for biasing the EAMs and the biases need to be adjusted based on the specific situation of the device. Also, the parameters are correlated with each other. For example, the DC EAM bias is related to the RF EAM biases as well as the modulation swing, and EAM phase will change as a result of EAM chirp when applying

a different bias to change its power output. Which means, when one parameter changes, all parameters may need to be re-adjusted. It is also difficult to modulate the two RF EAMs individually to see BPSK modulation and adjust related parameters separately, since the BPSK generation of one EAM depends on a couple of parameters including the correct phase and power relation of the EAM being modulated and the DC EAM, and adjusting those parameters will also affect if the other RF EAM can generate BPSK properly. For all these reasons, finding the operation point for the EAM-based modulator is more difficult, since not only there are more parameters, but the parameters are also related to each other and can not be adjusted individually.

5.3.2 Deviation from Theory

From the theory proposed by [1], the measurement setting seems very straightforward, with fixed power ratio and phase relation parameters to aim for. However, the actual process for finding the biases is more complicated for a couple of reasons.

Firstly, the theory in [1] is based on the assumption that the EAMs have infinite extinction ratio, so the two RF EAMs are either on or fully off. However, in actual measurements, the extinction ratio will be a finite number, which depends on a lot of factors including EAM design, EAM biases, as well as the swing of the RF signals driving the EAMs. For this reason, in actual measurements, the phase and power relation required for QPSK generation will deviate from theoretical values.

Aside from the deviation caused by extinction ratio, the setting of QPSK biases is further complicated by other factors. Biasing the RF and DC EAMs will introduce phase shift, which means the biases of the phase shifters may need to be adjusted to compensate for this effect. Also, since the silicon waveguide part and the EAM part of the transmitter are fabricated separately and edge coupled in later processing steps, the

coupling ratio may have some variation in between the three EAMs on one transmitter, making it difficult to determine the actual power ratio of the three paths. In addition, there may also be some variations in the EAM performance itself for the EAMs on the same transmitter. As a result of the variations, it is very likely that the two RF EAMs will need to be biased at different levels and modulated at different voltage swings.

Fig. 5.5 shows the effect on the transmitter output with only some of the factors mentioned above taken into consideration. Assuming the two EAMs are identical and biased at the same voltage and operated at the same swing, the extinction ratio and the EAM chirp will still have a significant impact on the transmitter output. When the EAMs have infinite extinction ratio and no chirp, the constellation is ideal when setting the phase and power relation as in [1], and the transition between constellation points follows a straight line. With the same phase and power relation, when the extinction ratio gets lower, the transmitter output constellation is no longer centered around the origin. Examples of transmitter output for 10 dB and 6 dB EAM extinction ratio are shown in Fig. 5.5 (b) and (c).These diagrams also assume 0.2 rad EAM chirp in the swing range of the EAMs, which causes a curved trajectory between the constellation points. The plots are generated assuming that when the RF EAMs are being modulated, the on state power level is 1. So when the extinction ratio starts to decrease, the off state starts to have a more significant effect, and the center of the constellation deviates from the origin. Although this effect can be compensated after capturing the data at the receiver output by using data processing script to move the center to the origin, it is worth noting that adjustment to phase and power relation needs to be made for the transmitter to operate as a phase modulator.

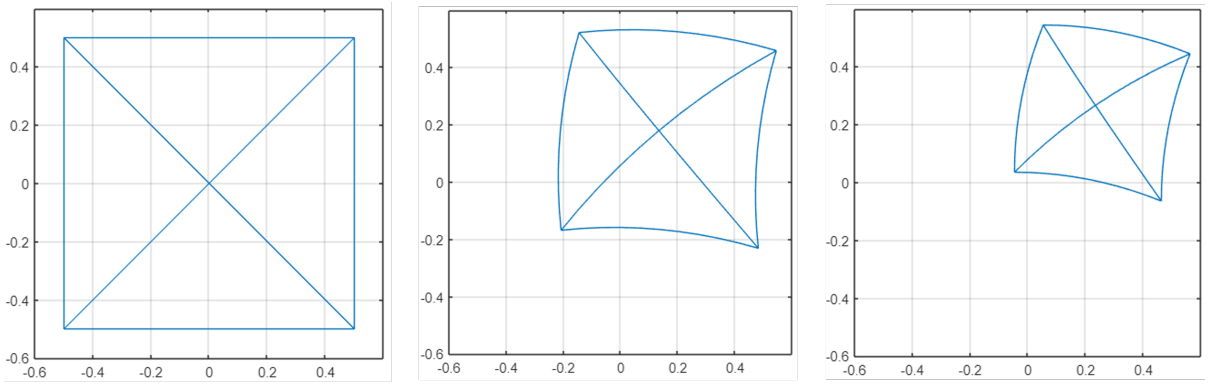

Figure 5.5: The effect of finite EAM extinction ratio and EAM chirp on transmitter output. (a) Infinite extinction ratio, no EAM chirp; (b) 10 dB extinction ratio, 0.2 rad phase change between EAM on and off states; (c) 6 dB extinction ratio, 0.2 rad phase change between EAM on and off states

5.3.3 Measurement Condition

In order to get a better understanding of the device performance, we measure the spectra of the two RF EAMs in the transmitter at different reverse bias levels. Since the measurement is directly taken from the modulator structure, while measuring one EAM, the other two EAMs are biased at a high reverse bias voltage in order to absorb most of the light in the other paths and in effect eliminate the power in those paths. The result is shown in Fig. 5.6. The measurement is taken when heating up the assembly to 50-60 ℃ using a thermoelectric cooler (TEC).

Even though the two EAMs are on the same transmitter, they have some variations from each other, which is the result of a combination of factors including difference in coupling loss and device variation. At lower wavelengths, the extinction ratio is higher, but at the same time the device suffers from higher insertion loss.

O-band device measurements are typically taken at 1310 nm. However, in the case with the particular EAMs measured at 50-60 ℃, the extinction ratio at 1310 nm is too small for modulation. To take measurement at a reasonable level of extinction ratio,

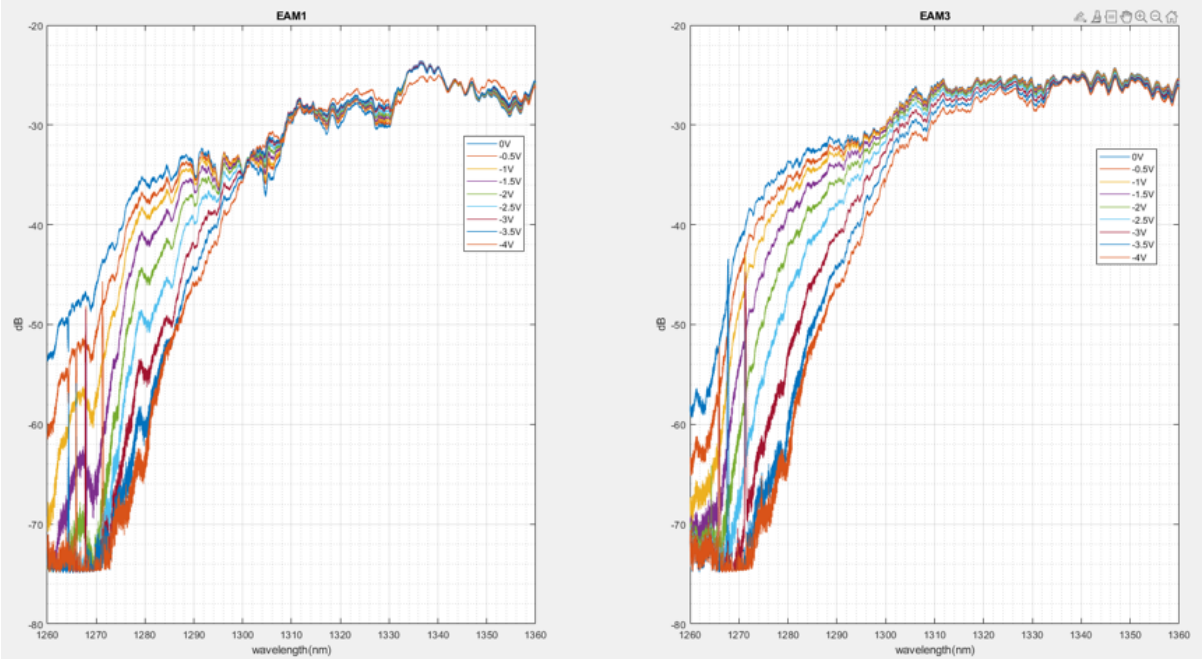

Figure 5.6: Spectra of two RF EAMs in the same transmitter

there are two options. One is to take measurement at a lower wavelength; and the other is to further increase the temperature so that the curves are red shifted to the point where there is a reasonable level of extinction ratio for 1310 nm. A number of the O-band equipment needed in the measurement setup such as SOA and commercial photonic receivers have an operation wavelength range starting from 1290 nm, which means the lowest wavelength that can be used is 1290 nm for equipment reliability. And in order to measure at 1310 nm, the curves need to be shifted by at least 10 nm, which means about another 20 ℃ higher in temperature. Most of the TECs and TEC controllers readily available in the lab are unable to maintain this temperature reliably. Considering all the factors mentioned as well as the trade off between extinction ratio and insertion loss, the measurements can be taken at 75 ℃ in between 1290 to 1300 nm.

5.3.4 Insertion Loss

For the particular EAMs in the transmitter, their transparency wavelength is higher than 1310 nm, and the insertion loss at transparency is around 6 dB. In the actual device, the insertion loss at transparency would be even higher because of the coupling loss at the interface between the silicon waveguide and the III-V EAMs. In addition, measurements are taken between 1290 to 1300 nm, where the insertion loss is higher than transparency.

The device structure and the QPSK generation mechanism also inevitably introduce more insertion loss. When only the phase relation and the power attenuation of the DC EAM is considered, in theory, the inherent loss through the transmitter is $(\sqrt{(}2)/6)^2 = -12.5$ dB. And also because of the combination of EAM biases and driver swing, the highest transmission of the EAMs may not be reached, so the total insertion loss can be even higher.

High insertion loss can make it challenging to get high signal to noise ratio (SNR) in the measurement. To address this issue, an SOA is placed before the transmitter for SNR improvement.

5.4 Stand-alone Transmitter Assembly

To verify the functionality of the transmitter, the first step is to build a stand-alone transmitter assembly to observe modulation from the RF EAM, as well as to verify the tunability of DC EAM power and the phase shifters.

Fig. 5.7 shows the stand-alone transmitter PIC assembly. All of the three EAMs have their anodes wire bonded to the high speed traces on the PCB, and cathodes wire bonded to the ground. The upper and lower EAMs are RF EAMs, and the middle EAM will only have DC biases applied to it. The longer wire bonds are for the DC biases of the thermal phase shifters. We apply thermal paste in between the PCB and the platform

underneath it, which is heated by a TEC unit and has its temperature monitored by a thermistor. It can be seen that because of fabrication requirement, all three EAMs are on one edge of the photonic chip instead of arranged in the way as the schematic in Fig. 5.3. The three EAM paths have the same total length and number of crossings.

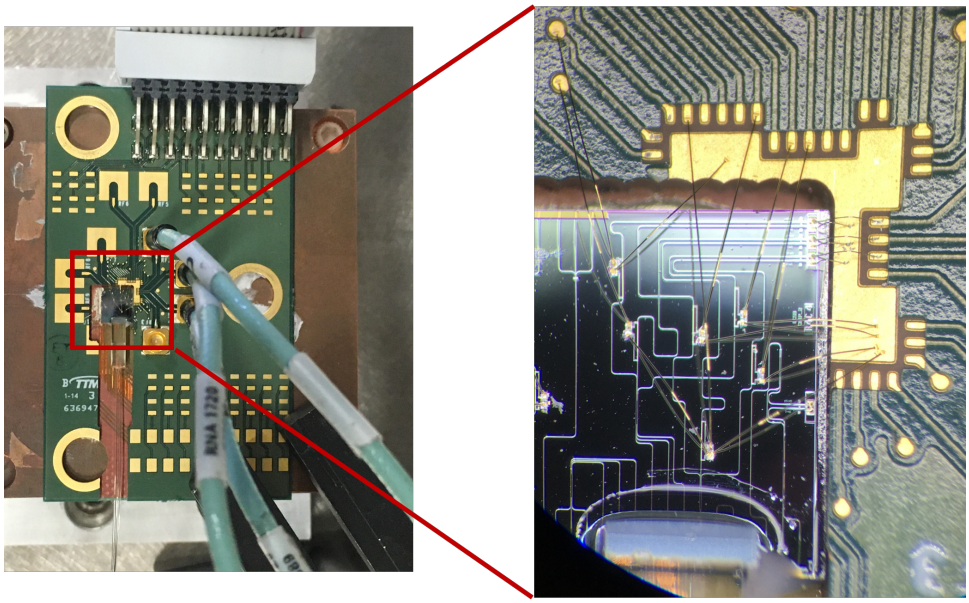

Figure 5.7: Stand-alone transmitter assembly

Fig. 5.8 shows the measurement setup of the stand-alone PIC assembly. In order to observe the eye diagram of a single EAM, the other two EAMs are biased at a high reverse bias level to minimize the optical power in these paths. An SOA as well as a PDFA is incorporated in the measurement setup because of the high insertion loss of the measurement setting. Although measurement can be carried out with the PDFA only, the SOA before the transmitter can significantly improve the SNR. Eye diagrams at 10 Gb/s, 20 Gb/s and 30 Gb/s are shown in Fig. 5.9.

To test the tunability of the DC EAM power and the phase shifters, QPSK measurement is carried out. The measurement setup is similar to Fig. 5.8, except that two PRBS data streams offset by bit delay have been used to modulate both RF EAMs.

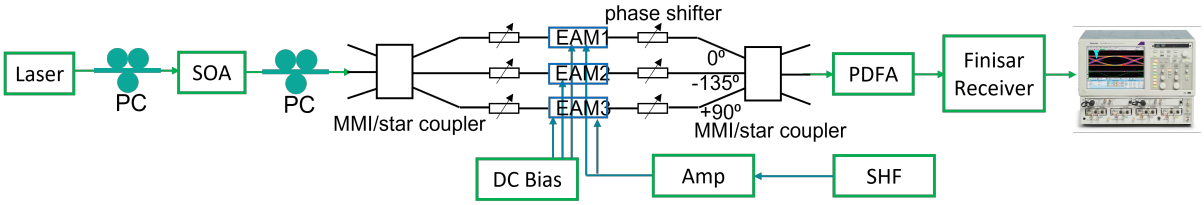

Figure 5.8: Measurement setup of stand-alone transmitter assembly

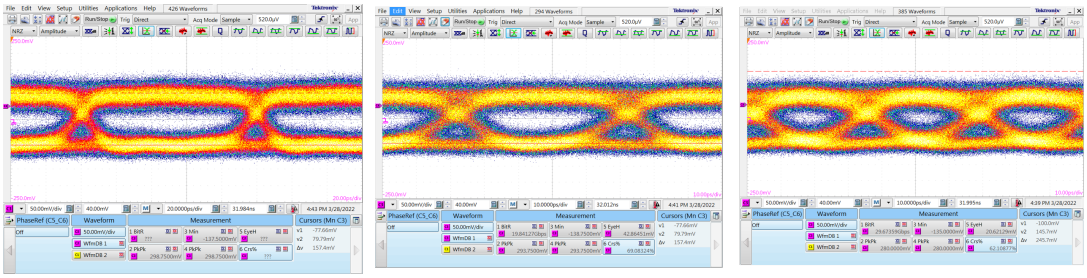

Figure 5.9: Eye diagram from a single EAM at (a) 10 Gb/s; (b) 20 Gb/s; (c) 30 Gb/s

Since the real time oscilloscope was not available at the time of measurement, sampling oscilloscope waveform was obtained, which is illustrated in Fig. 5.10. The sampling oscilloscope waveform shows a typical phase modulation with direct detection scheme. Although a constellation diagram is not obtained for this assembly, it shows that the phase shifters and EAMs have the tunability for QPSK modulation.

5.5 PIC-EIC QPSK Transmitter Assembly

5.5.1 Driver Performance

Having verified the functionality of the transmitter PIC, we move on to driver integration experiments. The driver is not specifically designed for the EAMs, so the performance of the EIC-PIC assembly can potentially be further improved with future driver design optimized for the EAMs. The driver is fabricated in GlobalFoundries 130 nm SiGe

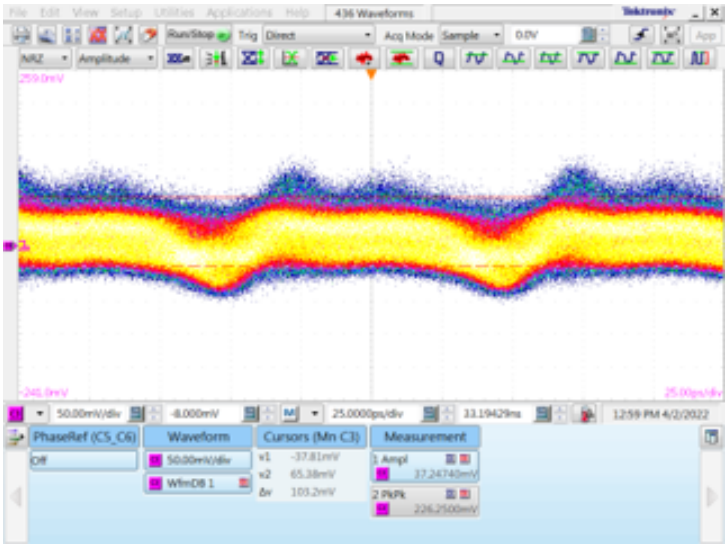

Figure 5.10: QPSK waveform at 10 Gb/s on sampling scope

BiCMOS process, and has 6-channel 50 Ω differential outputs, two of which are used in this assembly. The driver has 2-stage 50 Ω emitter-coupled differential pair output and 50 Ω input buffer, and is designed to have 12.5 dB single-ended gain. Fig. 5.11 shows the schematic of one driver stage and the driver layout. The dimension of the driver is 4.1 mm × 0.82 mm. Fig. 5.12 shows the simulated S_{21} and simulated 56 Gb/s eye with 50 Ω load. From the simulation, the driver has a 34 GHz bandwidth.

Since the driver isn't designed to have EAMs as its load, its output on EAMs will have some deviation from the simulated results with 50 Ω load. Fig. 5.13 provides an example of the simulation result of the driver output with EAM circuit model provided by Rockley Photonics as the driver load. The simulation also includes the EAM anode wire bond inductance with an estimated value of 150 pH, which is the wire bond in between the PIC and the EIC. The EAM cathode wire bond inductance is not included. Significant peaking and jittering can be observed in the eye diagram even when only part of the parasitics is considered.

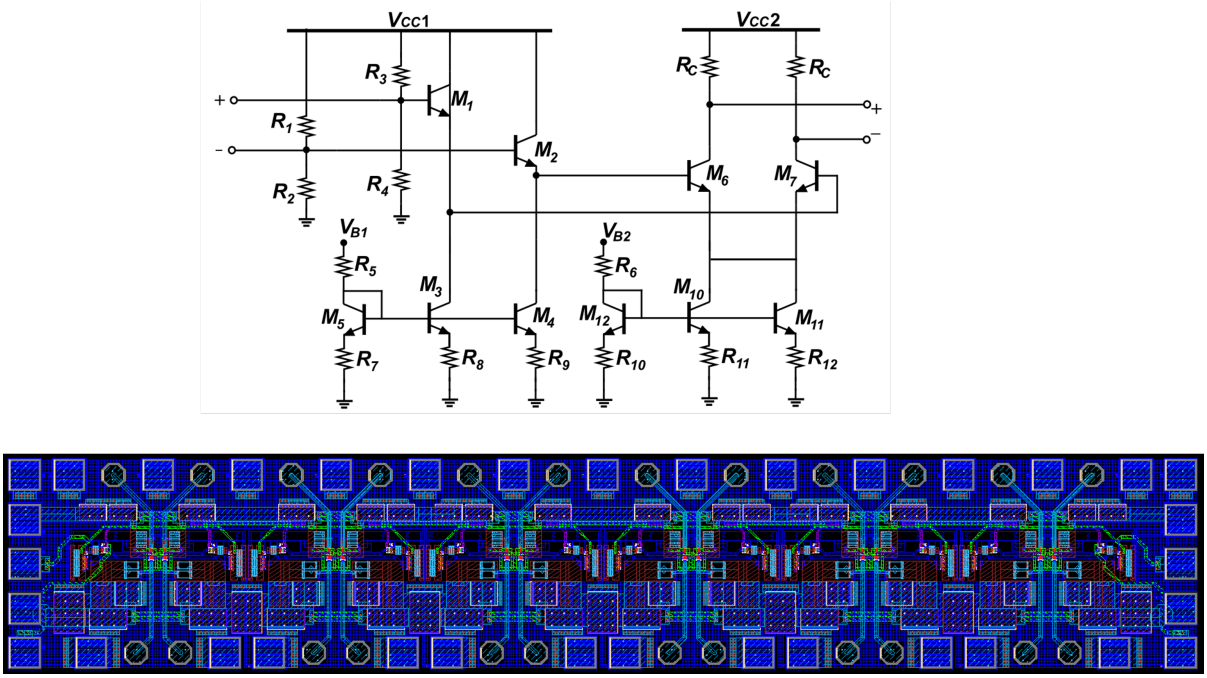

Figure 5.11: Schematic of one driver stage and driver layout

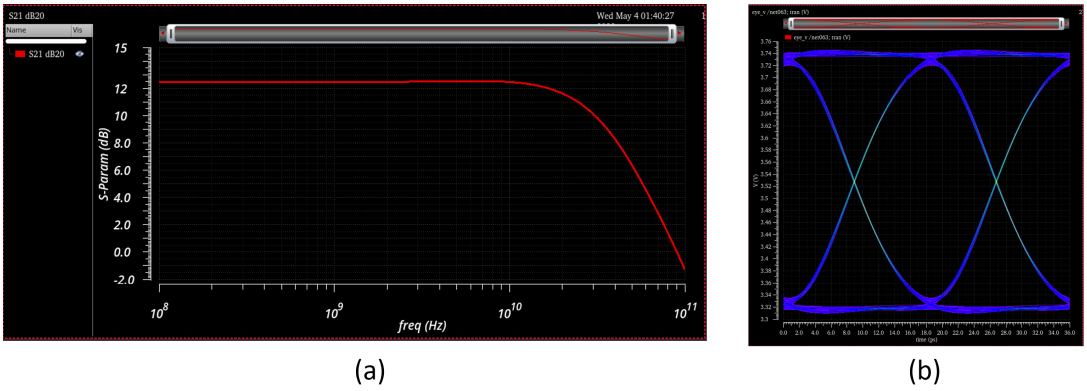

Figure 5.12: Simulation results of the driver with 50 Ω load. (a) S_{21}; (b) 56 Gb/s eye

5.5.2 Optimizing the Assembly

Fig. 5.14 shows the initial assembly wire bonding. From top to bottom, there are three EAMs. The top one and the bottom one are referred to as the upper EAM and the lower EAM, and they are both RF EAMs; the EAM in the middle is the DC EAM. The RF EAM anodes are wire bonded to the outputs of the EIC, and the RF EAM

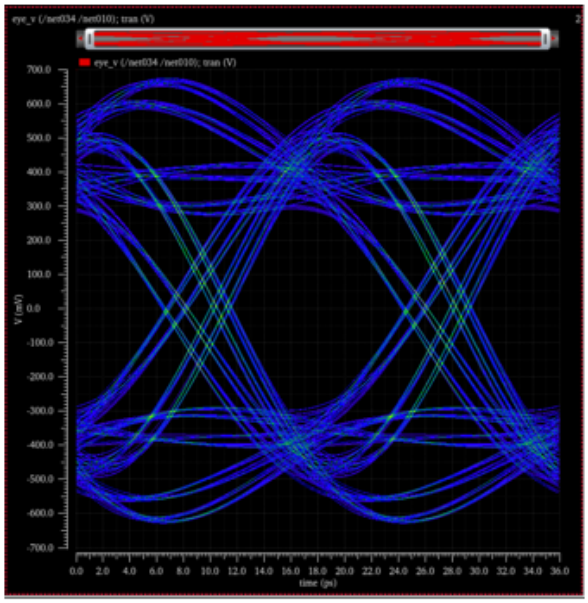

Figure 5.13: Simulation of driver output incorporating EAM anode wire bond and EAM circuit model

cathodes are wire bonded to DC biases on the PCB, as well as decoupling caps which are grounded on the other side for noise reduction. For the DC EAM, its anode is grounded and its cathode is wire bonded to a DC bias through a decoupling capacitor, similar to the cathodes of the RF EAMs. The inputs of the EIC are wire bonded to the high speed RF traces on the PCB. To account for the thickness difference between the PIC and the EIC, we milled a recess on the PCB to place the PIC.

Fig. 5.15 shows the assembly after making a couple of fixes, with Fig. 5.15(b) zooming in to the high-speed wire bond area. Since the milled area of the PCB was a bit longer than expected, the wire bonds from the cathode to the decoupling caps are longer than expected and cause bandwidth degradation. The high speed path wire bond length is reduced by adding small decoupling caps closer to the EAM cathodes. For the upper EAM, a small decoupling cap is added to the upper edge of the EIC and wire bonded to the upper EAM cathode. For the lower EAM, adding the decoupling cap is more difficult as a result of the length of the EIC. We added a decoupling cap onto the top of the EIC,

and its backside is connected to the ground pad of the EIC with epoxy. Since the EIC has aluminum pads and a thin layer of oxide will form on the top immediately when those are exposed to the air, we use wire bonding machine to break the oxide and leave a wire footprint before attaching the decoupling capacitor, so that a proper electrical connection can be made. Those changes are marked with red arrows in Fig. 5.15(b). Fig. 5.16(a) and (b) show the comparison between the single EAM eyes at 20 Gb/s and 30 Gb/s of upper and lower EAMs before and after shortening the cathode wire bond length. The significant improvement shows that the bandwidth of the assembly was previously degraded as a result of the long wire bonds.

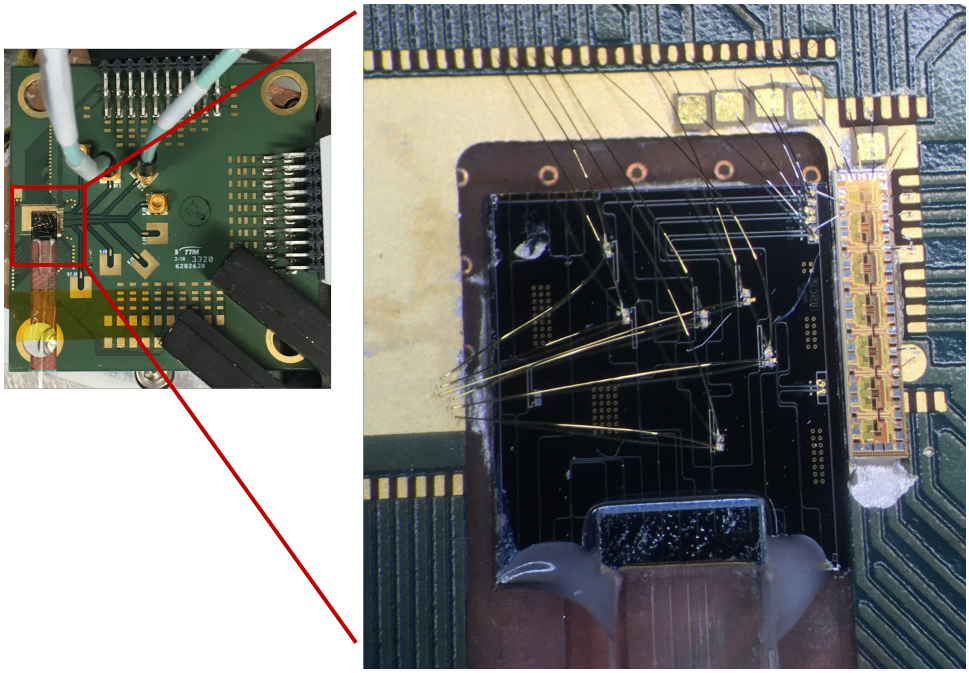

Figure 5.14: Initial wire bonding of the PIC-EIC QPSK transmitter

When trying to tune the device for QPSK constellation generation, we realized that another wire bond modification needed to be made. Previously, we have wire bonded the upper and lower EAM anodes to two differential outputs of the driver, whereas the two EAMs need to be driven independently. So we modified the wire bond so that the

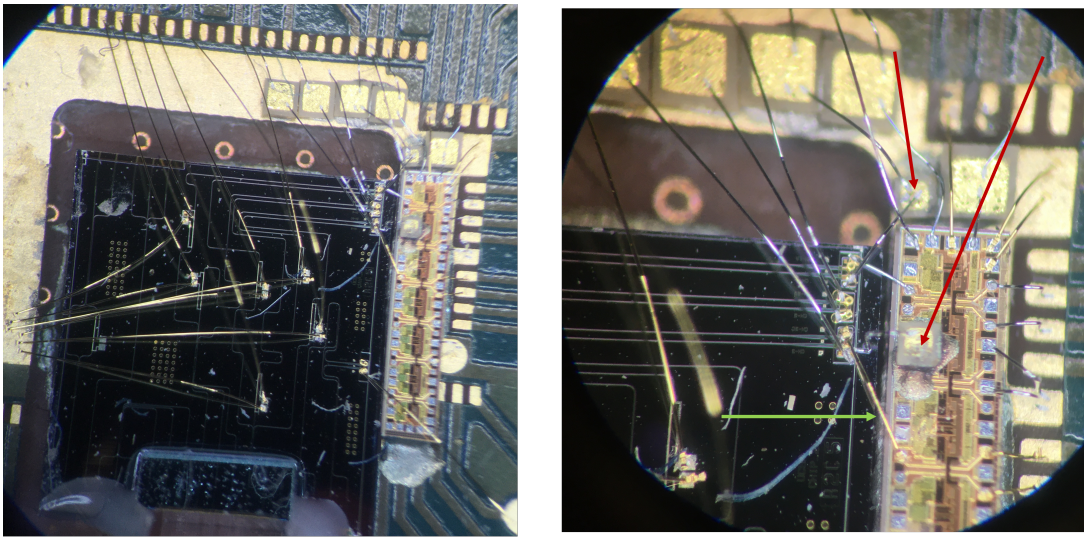

Figure 5.15: (a) Updated wire bonding of PIC-EIC QPSK transmitter; (b) The high-speed wire bonding area after the update

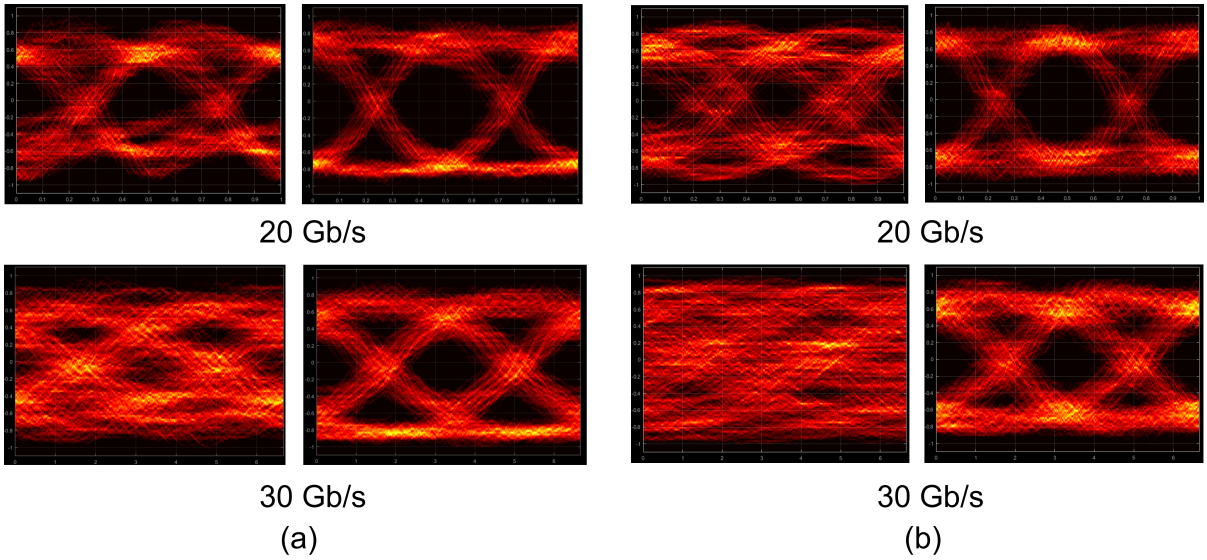

Figure 5.16: Comparison of single EAM eyes before and after shortening cathode wire bond lengths at 20 Gb/s and 30 Gb/s for (a) Upper EAM and (b) Lower EAM

anode of the lower EAM is wire bonded to another differential pair, and we also changed the EIC input wire bond accordingly. Afterwards, a RF connector needs to be added to have access to the modified modulation path. Because of the temperature limitation of

the fiber attach unit, we soldered the connector by heating up the PCB locally. The new anode wire bond is marked in Fig. 5.15(b) with a green arrow.

Fig. 5.17 shows a comparison between the single EAM eyes from the upper EAM and lower EAM after all the wire bond modifications are done as in Fig. 5.15. The SNR is low, since the eyes are taken directly from coherent measurement setup, meaning only part of the laser power goes into the transmitter and the rest of the power is routed to the LO. The eye opening of the upper EAM is smaller than that of the lower EAM as a result of device variation. However, the device bandwidths look similar although the lower EAM has a longer anode wire bond compared with before.

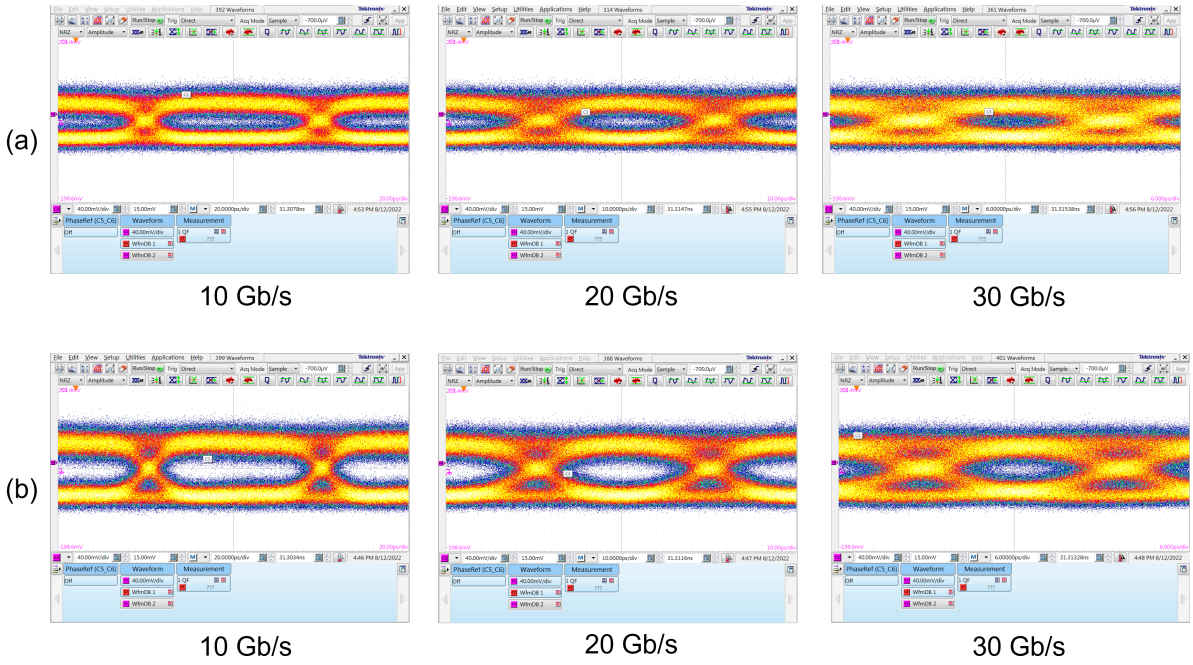

Figure 5.17: Comparison of single EAM eyes after fixing EAM anode wire bonds (a)Upper EAM; (b)Lower EAM

5.5.3 QPSK Constellation Measurement

Fig. 5.18 shows the measurement setup for the EIC-PIC assembly for QPSK modulation. In the signal path, there is an SOA before the transmitter, and also a PDFA at the transmitter output. As a result of high insertion loss of the transmitter and other fundamental factors which lead to even higher loss, the insertion loss of the modulator at the QPSK generation status can be as high as 35 to 40 dB, and the output power of the transmitter can be as low as -20 to -30 dBm. That is the reason why a PDFA is used at the device output instead of an SOA, since the PDFA can operate with input level as low as -30 dBm, whereas for the SOA the number is -20 dBm. Extra fibers are added to the LO path to match the added path length in the signal path introduced by the PDFA. Using an SOA before the input of the transmitter can help increase the SNR of the output signal. Since the SOA saturates with high input power, 10% of the laser power is routed into the SOA and 90% of the laser power is routed into the LO path. Since both the laser and the SOA used in the setup are PM, a PM splitter is used to reduce the number of polarization controllers needed. The coherent receiver used in this setup is composed of a commercial O-band 90-degree hybrid, and two balanced photodetectors with 70 GHz bandwidth connected to the hybrid outputs.

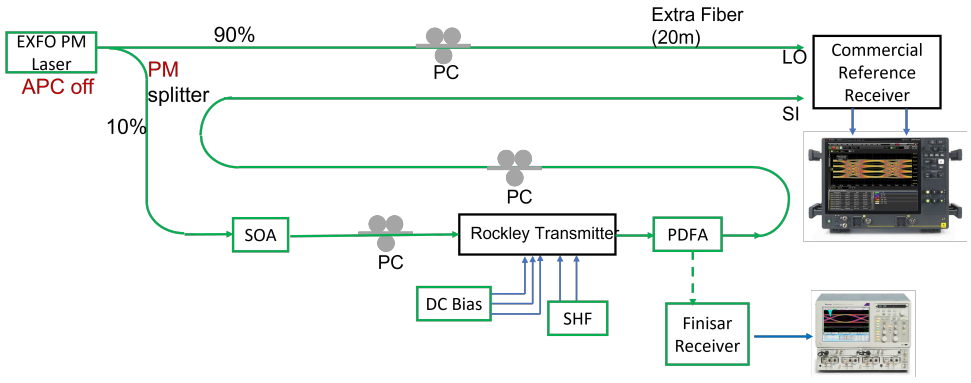

Figure 5.18: Measurement setup for Rockley transmitter QPSK constellation

To generate the QPSK constellation, figuring out the biases for the EAMs and the phase shifters is the first step. The method proposed below still needs work on, but it is a reasonably good start in finding the QPSK biasing point. The procedure can be summarized in the following steps:

1. Find biasing points for the two RF EAMs so that the power levels at the output are similar when one of them is set to the modulation biasing level and the two other EAMs are turned off (biased at high reverse bias level)

2. Adjust the modulation voltage swing for the two RF EAMs by observing the eye opening level when the other two EAMs are turned off so that the eye opening levels are similar when only one of the EAMs is being modulated

3. Turn off the RF modulation signal and bias the RF EAMs at the level determined in step 1, and turn off the DC EAM. Then adjust the phase shifters on one of the RF EAM paths so that the output power reaches the maximum. Then continue to adjust till the output power level is 3 dB lower than the maximum level. Doing this sets the phase relation of the two RF paths to 90°

4. (Optional) Turn on both of the modulation signals and observe the output signal through a commercial photodetector on a sampling oscilloscope. Ideally, at this point, the constellation diagram already has the phase and power relation of QPSK, but it is shifted so that the point previously in the third quadrant is now at the origin. For this reason, the waveform on the sampling oscilloscope should show three levels

5. Adjust the biasing level of the DC EAM and the phase shift in the DC EAM path so that the output power reaches the minimum level

6. Turn on both of the modulation signals and observe the output signal through a commercial photodetector on the sampling oscilloscope. Try tuning the two phase shifters as well as the biasing voltage of the DC EAM so that the waveform looks as close to QPSK waveform as possible. Then check that the waveform looks close to BPSK modulation when turning on the RF modulation signals individually (not exactly BPSK since the other RF EAM path still has some optical power)

7. Connect the device output to signal input port of the receiver and observe the waveform on the real time oscilloscope, and adjust the polarization of the PCs in the signal and LO path. Then use the data captured from the real time scope to plot constellation diagrams

Fig. 5.19 shows the constellation diagrams of the transmitter at 10 GBaud, 20 GBaud, 25 GBaud, 28 GBaud and 32 GBaud. The transmitter operates up to 50 Gb/s with BER below the KP4-FEC limit (2.2×10^{-4}), up to 56 Gb/s with BER below the HD-FEC limit (3.8×10^{-3}), and up to 64 Gb/s below the SD-FEC BER limit (2×10^{-2}). The limiting factors of the transmitter performance include the low SNR as a result of high insertion loss, as well as the EAM bandwidth.

5.6 Link Measurement

Having measured the receiver in Chapter 4 and the transmitter in this chapter, we took a step further to do a link measurement, where the Rockley receiver processes the data generated by the Rockley transmitter.

The measurement setup is similar to Fig. 5.18, except that the Rockley Photonics receiver is used instead of the commercial reference receiver. The constellation diagrams at 10, 20, 25, 28 and 32 GBaud are shown in Fig. 5.20. At each of the data rates, the full

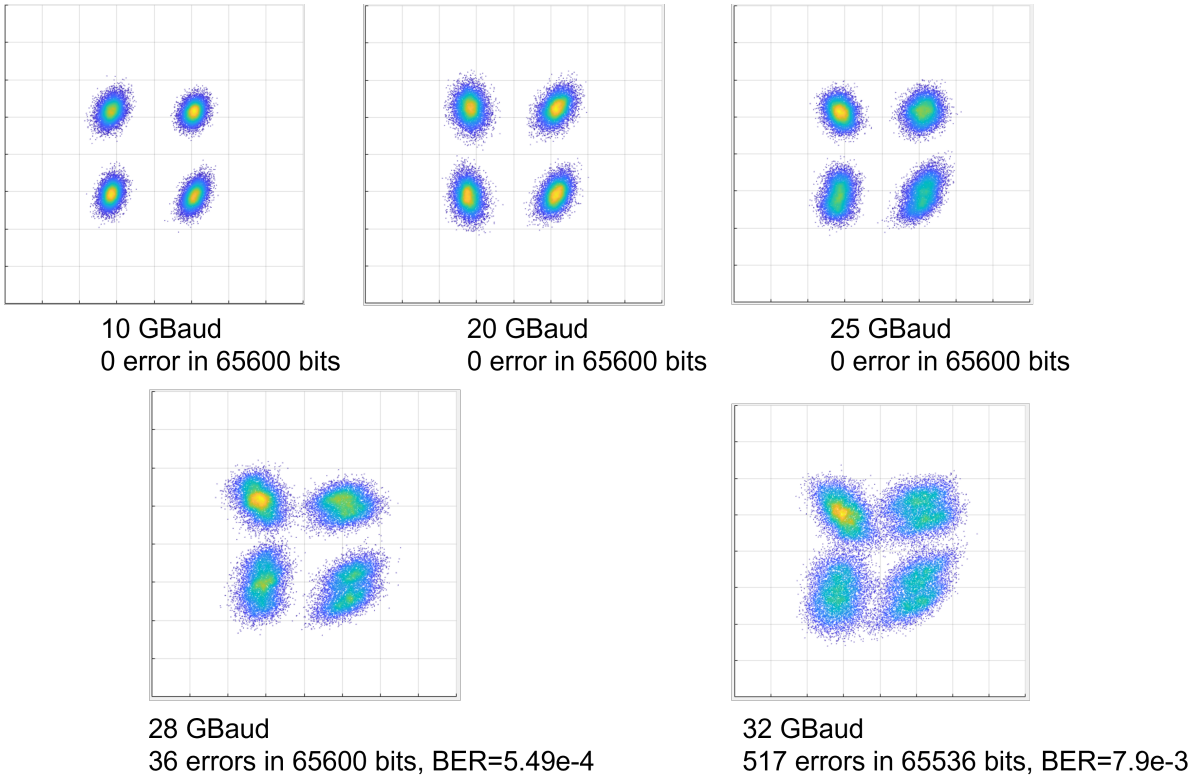

Figure 5.19: Rockley transmitter QPSK constellation diagrams at different data rates

link measurement has a higher number of errors compared with the Rockley transmitter with the commercial reference receiver, as can be seen from the comparison between Fig. 5.19 and Fig. 5.20. Nevertheless, at each data rate, the BER stays within the same FEC limit when using the Rockley receiver instead of the commercial receiver. In other words, the link operates up to 50 Gb/s with BER below the KP4-FEC limit (2.2×10^{-4}), up to 56 Gb/s with BER below the HD-FEC limit (3.8×10^{-3}), and up to 64 Gb/s below the SD-FEC BER limit (2×10^{-2}). There is not much degradation in BER from using the Rockley receiver, as can be expected from the receiver performance shown in Chapter 4. Although the receiver design is optimized for 1310 nm, the measurement is taken at 1290 nm wavelength because of the transmitter operation wavelength. This is the first O-band coherent full link demonstration on the Rockley Photonics multi-micron

silicon photonics platform.

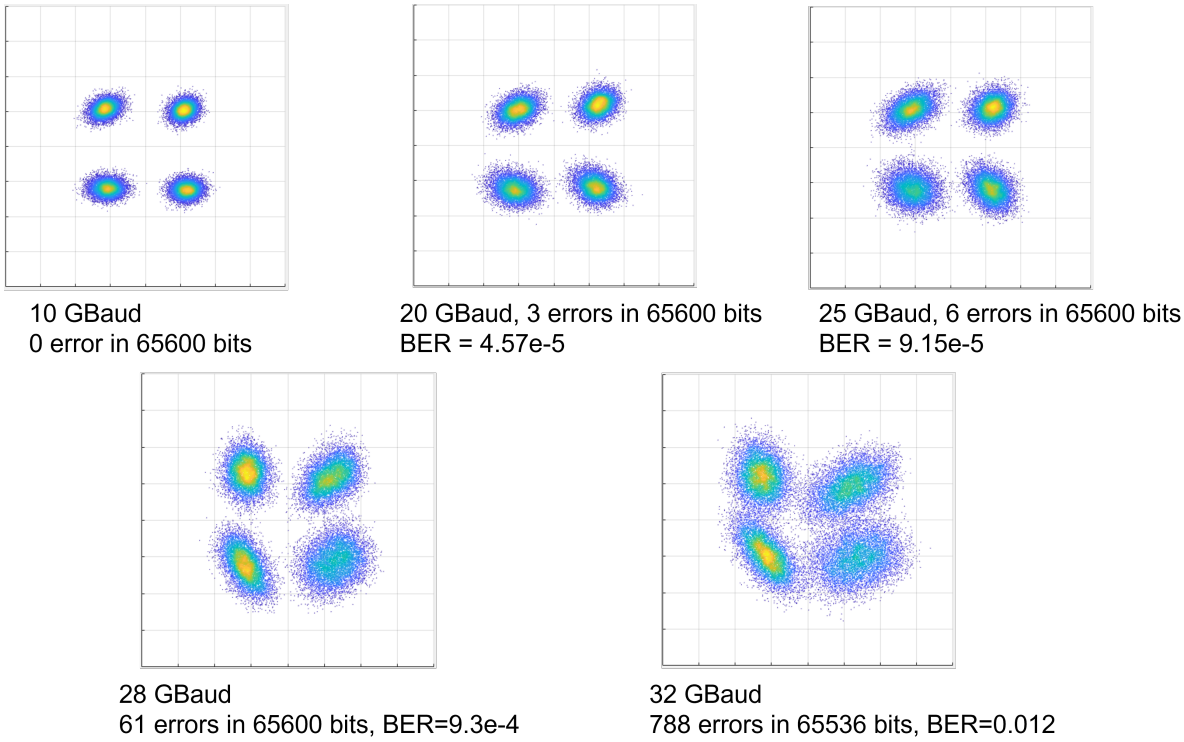

Figure 5.20: Rockley link QPSK constellation diagrams at different data rates

5.6.1 Energy Efficiency of the Link

It has been mentioned in Chapter 4 that the energy consumption on the receiver side is 98 mW. For the transmitter side, the energy consumption is composed of the driver power and the tuning power for the PICs with the phase shifters.

The total power consumption of the six-channel driver is 2055 mW. Since only two channels are used in this case, the EIC power consumption can be calculated as 2055/6x2 = 685 mW. As for the power consumption from tuning the phase shifters, three out of six phase shifters are operated at around 1 V. However, since the resistance of the phase shifters is only a couple of ohms, the current level is relatively high and the tuning power consumption comes out to be around 581.8 mW. Compared with those values, the power

consumption from EAM biases and PD biases is negligible. Adding the numbers together, the energy consumption of the full link is 1364.8 mW, which is 24.4 pJ/bit for 56 Gb/s and 21.3 pJ/bit for 64 Gb/s.

Although the energy consumption level is much higher than what we try to achieve, there are a couple of factors that can be optimized for a more energy efficient link. Firstly, the driver is not designed to be operated with EAMs, which contributes to the high power consumption. By designing drivers specifically for the EAMs, the driver energy efficiency can be improved. Also, the thermal phase shifters are simply metal wires that are not designed to heat up the waveguide efficiently, so the tuning efficiency has a lot of room for improvement by designing more efficient thermal phase shifters. Another aspect is the data rate. By optimizing the EAM design for higher bandwidth, and using flip-chip technology for the integration of EIC and PIC, the link will be able to operate at a higher data rate, and the pJ/bit level can be reduced.

Bibliography

[1] C. R. Doerr, L. Zhang, P. J. Winzer, J. H. Sinsky, A. L. Adamiecki, N. J. Sauer, and G. Raybon, *Compact high-speed inp dqpsk modulator*, *IEEE Photonics Technology Letters* **19** (2007), no. 15 1184–1186.

[2] C. Gui, P. Dong, G. de Valicourt, H. Chen, N. K. Fontaine, K. Kim, and Y.-k. Chen, *Experimental demonstration of quadrature phase-shift keying silicon ring modulator based on intensity modulation*, in *2015 European Conference on Optical Communication (ECOC)*, pp. 1–3, 2015.

[3] K. Goi, A. Oka, H. Kusaka, Y. Terada, K. Ogawa, T.-Y. Liow, X. Tu, G.-Q. Lo, and D.-L. Kwong, *Low-loss high-speed silicon iq modulator for qpsk/dqpsk in c and l bands*, *Opt. Express* **22** (May, 2014) 10703–10709.

[4] A. H. Talkhooncheh, A. Zilkie, G. Yu, R. Shafiiha, and A. Emami, *A 100 gb/s pam-4 silicon photonic transmitter with two binary-driven eams in mzi structure*, in *2021 IEEE Photonics Conference (IPC)*, pp. 1–2, 2021.

Chapter 6

Conclusion and Future Work

6.1 Conclusion

The goal of the work presented in the dissertation is to develop energy efficient O-band QPSK analog coherent receivers and transmitters. The dissertation starts by stating the limitations of IM/DD links and introducing the concept of coherent detection. Then a brief introduction of the history of coherent optical system is given, including the research activities in the early days driven by sensitivity improvement, the pause of related research as a result of EDFA emergence, as well as the revival of interest in coherent technology, which started primarily using DSP in long-haul communication, and then expanded to intra-data center links. Then the dissertation also explains the advantage of DSP-free coherent links for data center link application, as well as the reason for choosing QPSK as the modulation format.

In this dissertation, three EIC-PIC integrated QPSK receivers are demonstrated based on different fabrication platforms. All of them are capable of operation up to 100 Gb/s below the HD-FEC BER limit. The dissertation also presents an EAM-based QPSK transmitter integrated with an EIC driver, and demonstrates its operation at up to

56 Gb/s below the HD-FEC BER limit, and up to 64 Gb/s below the SD-FEC BER limit. The dissertation also shows a link measurement with both the transmitter and the receiver based on Rockley Photonics technology. The link operates up to 56 Gb/s below the HD-FEC BER limit, and up to 64 Gb/s below the SD-FEC BER limit. The energy saving advantage of the analog coherent scheme has been proved with 1 pJ/bit energy consumption for one of the receiver assemblies.

For the coherent receiver, both receiver EICs utilized in the assemblies presented in the dissertation have OPLL functionalities integrated in them. However, the closed loop operation is not demonstrated in the scope of dissertation for lack of integrated laser on the PIC.

Coherent receivers for DSP-free intra-data center links need to have low loss, high bandwidth, and an on-chip LO laser for OPLL. When on-chip lasers are not available, self-homodyne technique is the most straightforward means of detection. The PIC and EIC platforms need to be chosen according to these requirements. The work in the dissertation involves InP, GlobalFoundries 90WG, and Rockley Photonics for the PIC platform, and GlobalFoundries 130 nm SiGe HBT and 45 nm CMOS for the EIC platform.

Both GlobalFoundries 90WG and Rockley Photonics are SiP platforms, which makes them subject to some disadvantages compared with InP platforms in data center link application, as will be mentioned in Section 6.2.1. However, at the same time, SiP platform also has advantages of larger scale integration and lower cost compared with InP platform. From an integration stand point, although Si platforms do not have intrinsic laser integration, monolithic electronic-photonic integration is more straightforward compared with InP platform, since part of the initial motivation for developing silicon photonic platform is to utilize the readily available large scale integrated electronics fabrication technology. For example, the GlobalFoundries 90WG platform supports monolithic integration, which can reduce interface parasitics in packaging and result in higher operation

speed. While Rockley Photonics platform does not have monolithic electronics integration capability, it is more fundamentally suited for integration with III-V components such as lasers and EAMs, and demonstrations of integration with those devices have been made. However, the yield and coupling loss of the integration technique remain challenging. For these reasons, to have on-chip LO and OPLL for the coherent receiver, InP platform seems to be the most straightforward option. From the loss stand point, Rockley Photonics multi-micron silicon photonic platform has the most advantage because of its low coupling loss and low propagation loss.

The bandwidth and power efficiency of the PIC-EIC assemblies also depend on the EIC platform. The 130 nm SiGe process has a higher bandwidth than the 45 nm CMOS platform, whereas the 45 nm CMOS platform is more energy efficient compared with the 130 nm SiGe platform.

6.2 Future Work

6.2.1 InP Coherent Receiver and Transmitter

It has been mentioned that OPLL operation has not been demonstrated in the work presented in the dissertation. The major reason is that there is no laser integration provided by the silicon photonic platforms at the time when the photonic chips shown in this dissertation were fabricated. Different approaches have been developed for laser integration on silicon, including integrating III-V lasers on Si with bonding approaches, as well as direct crystal growth of IIIV semiconductor lasers on Si. Those methods are complicated and face a lot of technical difficulties.

For this reason, InP photonics platform has a significant advantage. The InP platform supports laser as well as other components needed for coherent receiver, so there isn't

complicated bonding or heteroepitaxy process involved. Also, unlike silicon, InP exhibits Pockels effect, which is the linear electro-optic effect where the refractive index changes in proportion to the applied electric field. As a result, Mach-Zehnder based QPSK modulators on InP platform can be shorter and can have a higher efficiency compared with its Si counterpart. QPSK modulators based on EAMs similar to those mentioned in Section 5.1 on InP platform also offers some advantages. EAMs require lower drive voltage compared with Mach-Zehnder modulators, and they also have less parasitics because of their small size, which is an advantage for high-speed application. Having the transmitter fully on InP platform can also facilitate laser integration, which reduces the loss from coupling the laser into the modulator, and makes a more compact system.

Previously, we have fabricated InP receivers with integrated sampled grating distributed Bragg reflector (SGDBR) laser and some test structures. Fig. 6.1 shows the schematic of an InP-based receiver, including an on-chip SOA for the signal port, and the integrated SGDBR LO enables the potential of closing the loop with OPLL. Fig. 6.2 shows a microscopic image of a die. It consists of a couple of full receiver PICs, as well as some test structures such as broad area laser, MMIs, SGDBRs and PDs. These devices didn't perform as expected as a result of some epi design and processing issues, but the research effort in this path is still going on with new receiver designs being fabricated on semi insulating substrates.

6.2.2 Clock Recovery

In the process of Rockley transmitter constellation diagram measurement, at one point, the sampled constellation was showing traces between constellation points. This shows that the clock period of the pattern generator and the real time oscilloscope may have a slight difference, which will result in the position of sampling points relative to

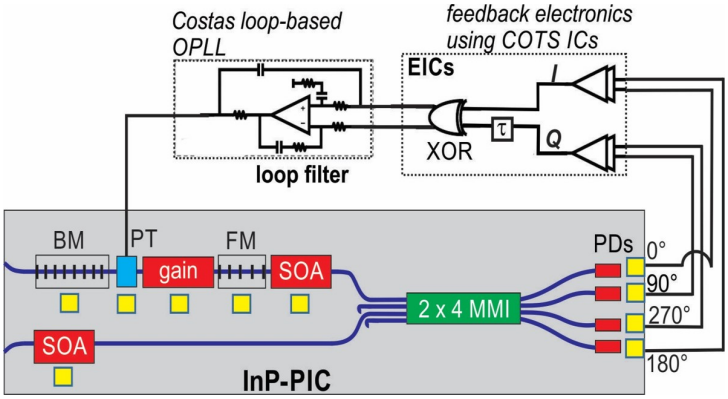

Figure 6.1: Schematic of InP coherent receiver with OPLL

the bit periods getting shifted over time, as shown in Fig. 6.3. It can be seen that the sampling points gradually change position relative to the bits, and shift from the center of the bit to the rising or falling edges of the bit. The sampling points which corresponds to the traces in the constellation diagram are all presented in a certain time period, which shows that it is not a result of a random process such as noise.

In later measurements, we got rid of the issue by connecting the 10 MHz reference output of the oscilloscope to the 10 MHz reference input of the pattern generator. It did not work the other way around, which may suggest some problems with the pattern generator clock. However, in real transceivers, there is no guarantee that the receiver clock is in sync with the clock on the transmitter side, so clock recovery technique needs to be utilized.

Clock recovery can be carried out in a couple of ways, and one of those is using a phase locked loop (PLL). Depending on the modulation scheme, there are different types of PLL such as early-late clock recovery and zero-crossing clock recovery. There are demonstrations of clock recovery circuit in CMOS 90 nm technology, and some examples are shown in [1] and [2]. It can also be done with DSP algorithms such as the work discussed in [3].

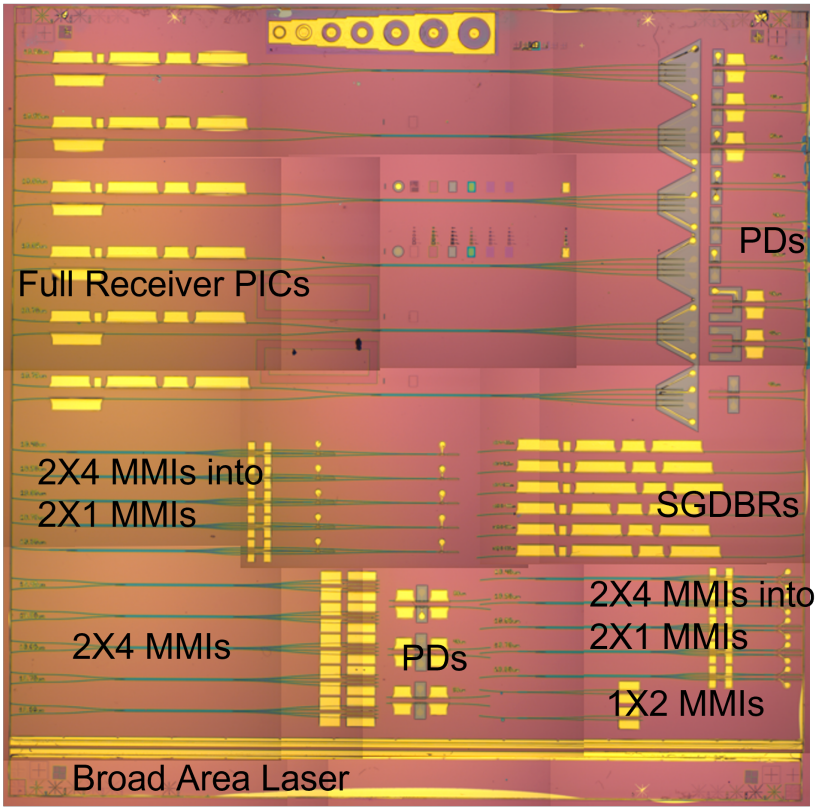

Figure 6.2: Microscopic image of InP coherent receiver

6.2.3 Polarization Recovery

In Chapter 3, we have demonstrated the high speed performance of a single polarization of the coherent receiver. The data rate can be directly doubled if polarization multiplexing technique is utilized. To separate the incoming polarization, we have incorporated PDK polarization splitter-rotator (PSR) in the layout. However, polarization rotation effect needs to be compensated before the light goes into the 90-degree hybrids for each polarization.

The authors of [4] proposed a structure for compensating for the polarization rotation which is a result of propagation in the fiber. According to [4], the polarization transformation due to fiber propagation in the absence of polarization-dependent loss (PDL) and polarization mode dispersion (PMD) can be expressed as

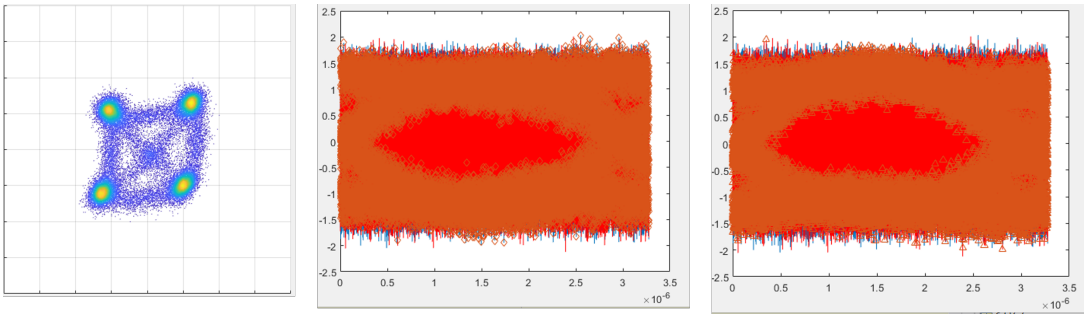

Figure 6.3: Constellation diagrams and sampling points as a result of clock synchronization issue

$$T_{Fiber} = \begin{bmatrix} e^{j\alpha_1} & 0 \\ 0 & e^{-j\alpha_1} \end{bmatrix} \begin{bmatrix} \cos(\zeta) & -j\sin(\zeta) \\ -jsin(\zeta) & \cos(\zeta) \end{bmatrix} \begin{bmatrix} e^{j\alpha_0} & 0 \\ 0 & e^{-j\alpha_0} \end{bmatrix} \tag{6.1}$$

where the variables α_0, ζ and α_1 represent random, time-varying rotation variables of the unitary matrix corresponding to the rotation undergone by propagation through the fiber.

As a result of the rotation, the data at the two outputs of the PSR is no longer the original data on the X and Y polarization; instead, it becomes a combination of the original X and Y data at each of the PSR output. In order to compensate for this rotation, a similar matrix needs to be set up as

$$T_{Controller} = \begin{bmatrix} e^{j\phi_1} & 0 \\ 0 & e^{-j\phi_1} \end{bmatrix} \begin{bmatrix} \cos(\theta) & -j\sin(\theta) \\ -jsin(\theta) & \cos(\theta) \end{bmatrix} \begin{bmatrix} e^{j\phi_0} & 0 \\ 0 & e^{-j\phi_0} \end{bmatrix} \tag{6.2}$$

which can be obtained by setting up a sequence of three phase shifters, and ϕ_0, θ and ϕ_1 correspond to the phase shift in each section. The structure is shown in Fig. 6.4. Based on this theory, we designed a polarization recovery test structure in the GlobalFoundries 90WG process, the layout of which is shown in Fig. 6.5. It has exactly the same structure

as proposed in [4], with PSR and thermal phase shifters. Each output is connected to a 50/50 power splitter to facilitate on-chip photodetectors as well as grating couplers as two ways to access the output.

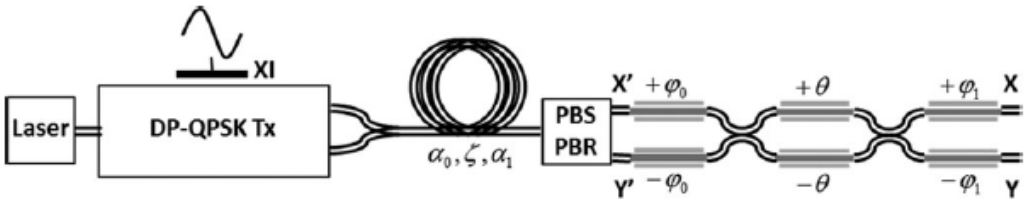

Figure 6.4: Polarization recovery structure composed of three phase sections [4]

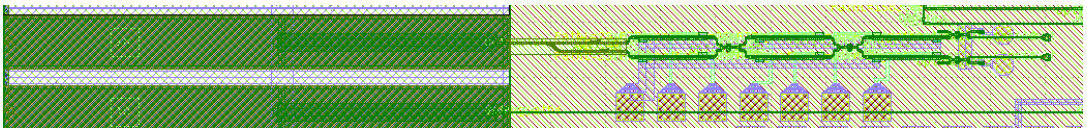

Figure 6.5: Polarization recovery test structure

We did a couple of experiments to verify the functionality of the polarization recovery section. The first experiment was done by using an adjustable polarizer. By adjusting the polarizer, we can have two orthogonal input polarization status and measure the power spectra at the two outputs of the test structure.

Fig. 6.6 shows the measurement setup and the measurement result. CT440 is a piece of equipment which works together with the laser source and a computer software to automatically obtain the power spectrum of the device output. It can be seen from the measurement result that orthogonal polarization status can be separated and will propagate in different output ports.

Later, we designed another setup to show the performance of the polarization recovery section. Two MZMs are modulated by sine waves at different frequencies: in this particular measurement, f_1=20 MHz and f_2=30 MHz. Then the two signals are combined using a polarization beam combiner, and by doing this, the two orthogonal polarizations

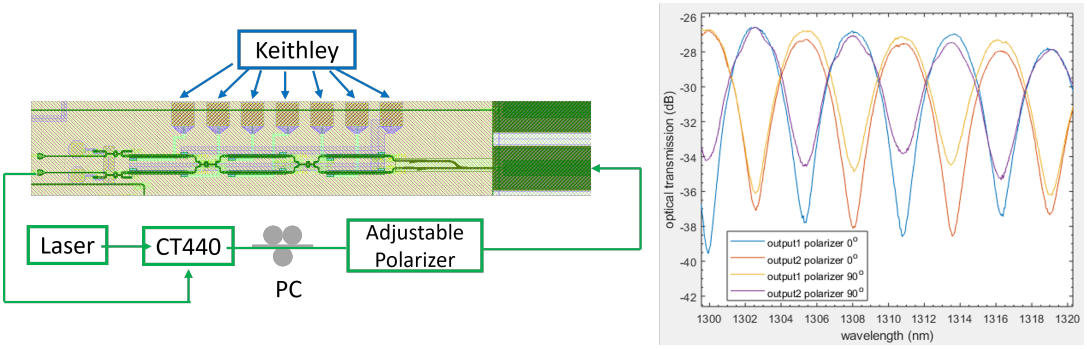

Figure 6.6: Polarization recovery measurement with adjustable polarizer

of the PM fiber at the polarization beam combiner output each carry one of the signals. Then the combined signal goes through a polarization controller to simulate the effect of fiber rotation; and the combined signal gets coupled into the polarization recovery section test structure, and its outputs goes into photodetectors. An electrical spectrum analyzer (ESA) was used to monitor the beat tone of the output signal. This measurement setup is shown in Fig. 6.7.

When modulating MZMs with sine waves, depending on the bias status of the MZMs, different sidebands will be generated, including carrier, odd and even order of sidebands. Odd order sidebands, or even order sidebands together with the carrier, can be suppressed when biasing the MZM at certain conditions. When the power of the modulation sine wave increases, high order sidebands will be generated. The modulated signal will beat with each other in the photodetector and generate beat tones at frequencies equal to the frequency differences of the beating signals. For this reason, to simplify the measurement, we control the power of the sine wave to a relatively low level, so that only the carrier and the first order sidebands are generated.

In some preliminary measurements, tuning the phase shifters allows the spectrum at one of the outputs to shift from showing only one frequency to showing only the other frequency, whereas when the phase shifters are not tuned the output contains both

frequencies. The pictures of the spectra shown by ESA are shown in Fig. 6.7.

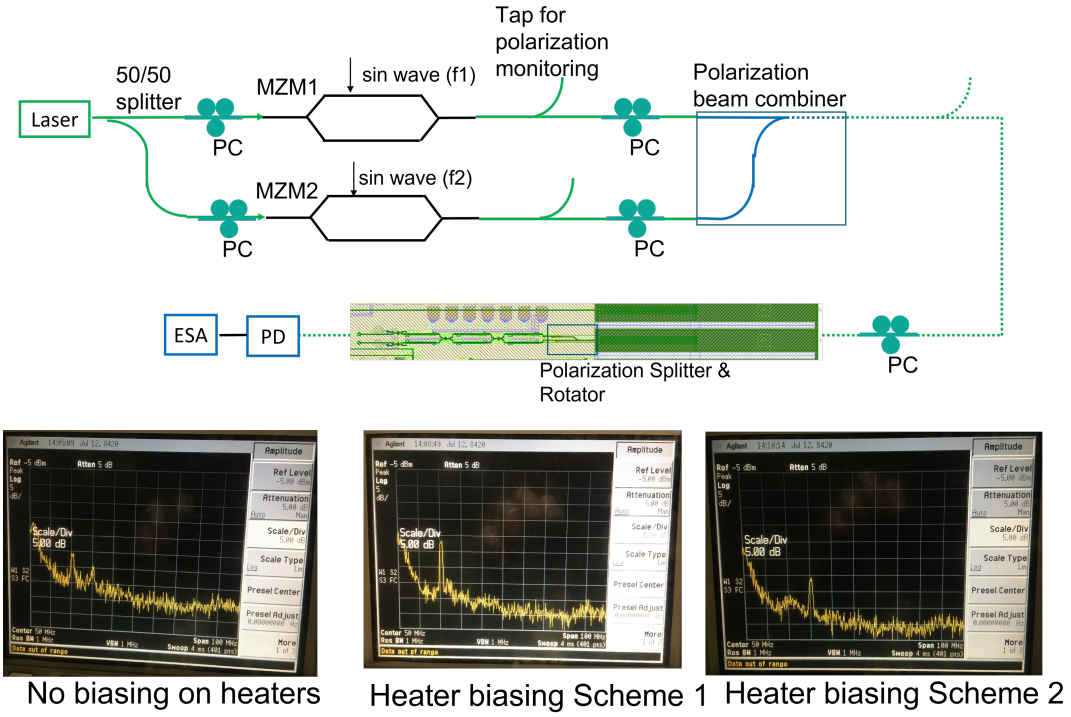

Figure 6.7: Polarization recovery measurement with MZMs

An issue with this setup is that the fiber at the device output has to be moved back and forth to couple the light from the two grating coupler outputs. The polarization may drift when the coupling takes long. Also, the polarization status may change in the fiber going from the grating couplers at the device output into the photodetector, resulting in inaccurate polarization status measurement. A way to avoid this problem is to utilize the on-chip photodetectors to convert the output optical signal directly into an electrical signal. In order to use the on chip photodetector and for convenience in testing, an assembly was built as shown in Fig. 6.8.

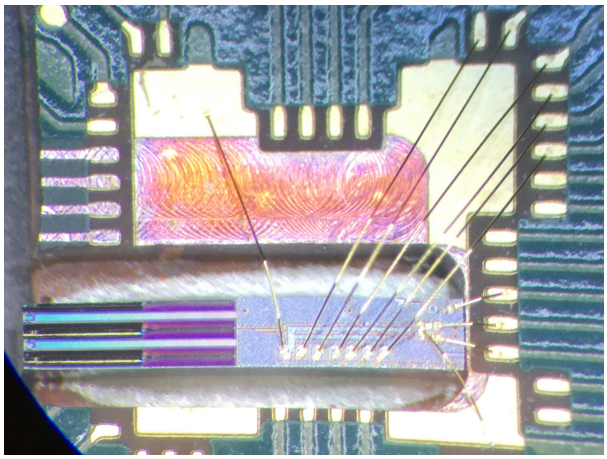

Figure 6.8: Polarization recovery test structure assembly

Dual-Pol Demonstration of Coherent Receiver

In most of the receiver designs in GlobalFoundries 90WG process, the receivers have a PSR integrated with it but do not have a polarization recovery section because of area limitation. One of the coherent receiver designs has a polarization recovery section following the PSR. Its design is shown in the lower part of Fig. 3.11, and the preliminary single polarization measurement result on its stand-alone PIC assembly is shown in Fig. 2.4(b). Fig. 6.9 shows the microscopic image of the device, as well as a single polarization PIC-EIC assembly based on this device, and some preliminary constellation diagram measurement results are also given. The EIC is wire bonded to only one of the polarizations of the PIC because of limitations of the PCB dimension. In order to fully characterize the dual-pol performance, a new PCB needs to be designed to fit in two EICs, one for each polarization.

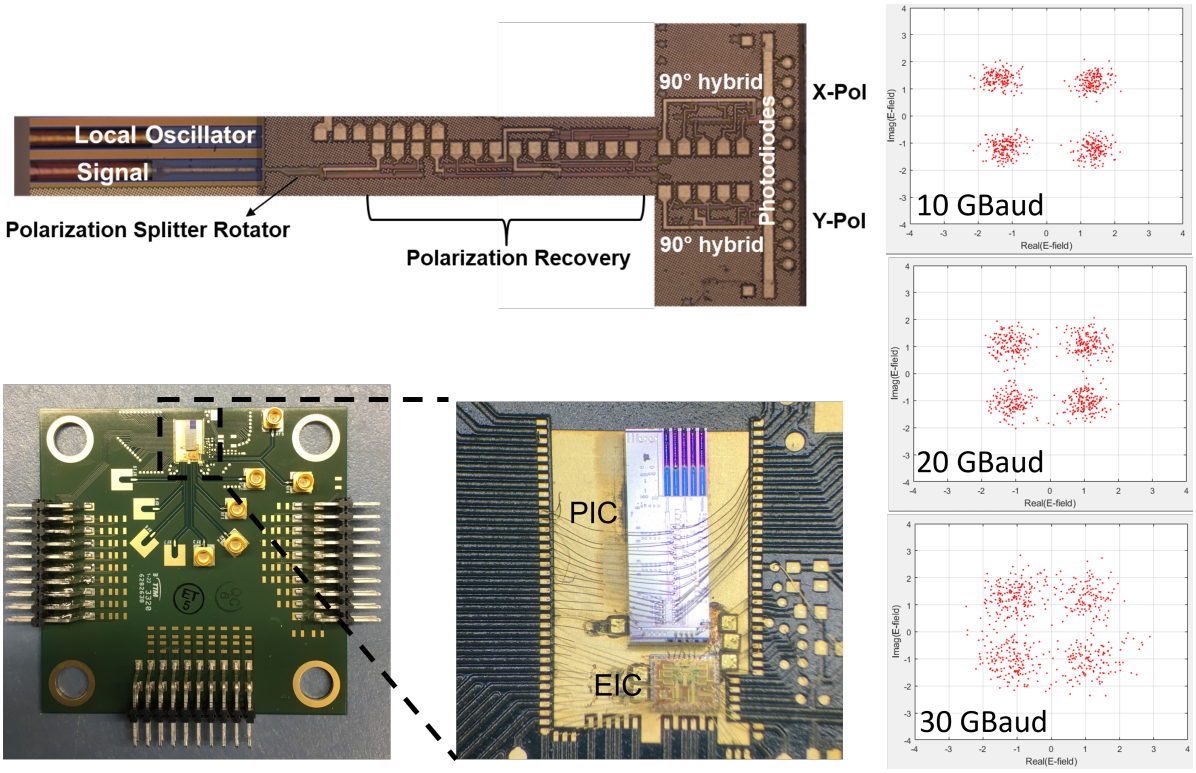

Figure 6.9: GlobalFoundries receiver with polarization recovery section

6.2.4 Optimization on EAM-based QPSK Modulator

Optimizing the Packaging for Higher Speed

From Section 5.5, it can be seen that longer wire bond length can significantly affect the bandwidth of the assembly. For this reason, the next generation of Rockley transmitter will be designed for flip-chip integration with the electronic chip. The flip-chip schematic for the transmitter is shown in Fig. 6.10. In addition, the EIC will be designed specifically for the EAM load, which will also improve the assembly performance.

Power Efficiency and Performance Optimization

Power efficiency optimization for Mach-Zehnder based QPSK modulators has been discussed in [5]. The MZM is biased at null point for phase modulated signal, and there

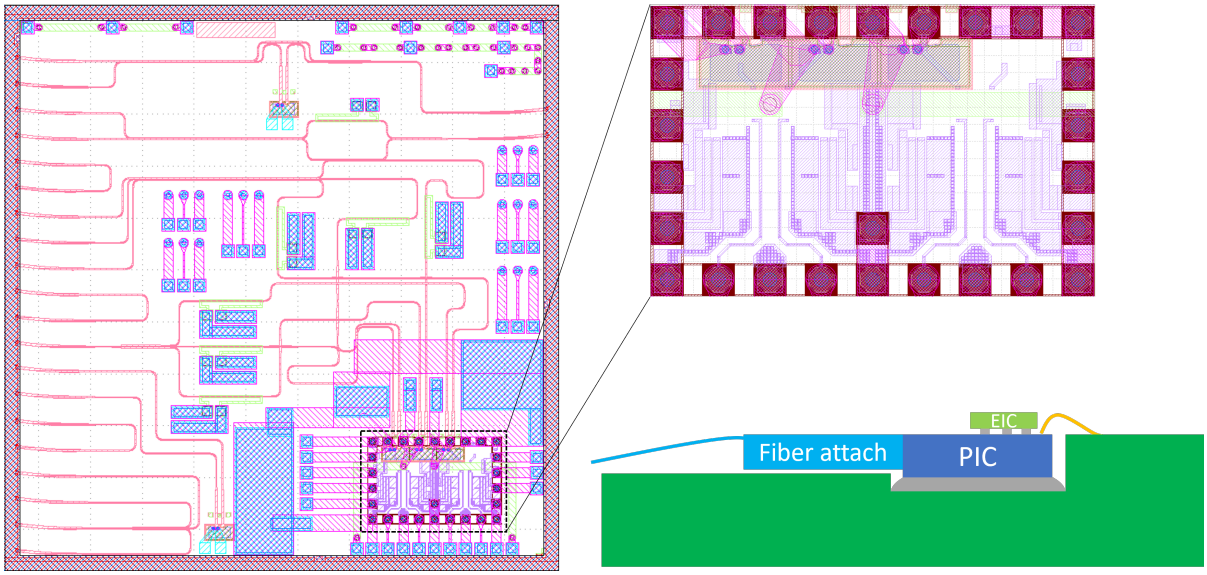

Figure 6.10: Flip-chip schematic of Rockley transmitter

is modulation loss when the modulation voltage swing is lower than $2V_\pi$. For Mach-Zehnder QPSK modulators with driver, there is a fundamental power consumption trade off: higher drive voltage reduces the modulation loss at the expense of higher driver power consumption; and lower drive voltage reduces the driver power consumption but leads to increased modulation loss which needs to be compensated for by higher laser power.

For the EAM-based transmitters, there is a similar power consumption trade off. But it is more complicated since the EAMs do not have a fixed biasing point for QPSK modulation, and the choice of biasing point may not be the same for the two RF EAMs as a result of device variation and coupling loss variation. Also, although increasing the drive voltage leads to lower optical loss, it may not be the best practice for performance optimization since higher drive voltage leads to more chirp. For all these reasons, power efficiency and performance optimization for the EAM-based QPSK transmitter has more factors that need to be considered, and is more complicated compared with that of Mach-Zehnder based QPSK modulator.

Polarization Management

The Rockley transmitter is composed of waveguides and MMIs in the multi-micron silicon photonics platform, and III-V EAMs. The silicon photonics part of the device is polarization independent; however, the EAMs are polarization dependent. This means the polarization of the light going into the device can affect its performance such as loss and modulation efficiency. The polarization status can also affect the modulation waveform and the constellation diagram, since it changes the power level in each path. However, since the PIC is composed of polarization independent waveguides, EAMs that absorb light, and power combining components whose output is subject to the phase offsets between the input paths, it is hard to determine the optimized polarization of the light by monitoring the output power level.

In addition, for the 3×3 MMI in the transmitter and 4×4 MMI in the receiver, their polarization dependence also needs to be considered. When doing the MMI designs, simulation needs to be done for both TE and TM input to minimize the variation of device performance for different polarizations, and to take advantage of the polarization independence property of the platform.

Operation Wavelength Optimization

As mentioned in Section 5.3.3, there is a trade off between EAM insertion loss and modulation swing at different wavelengths. This means there can be an optimized operation wavelength depending on how the link is set up and whether it is more sensitive to loss or modulation swing. In the measurements taken in this dissertation, there hasn't been a lot of efforts on operation wavelength optimization. However, this can be an interesting topic worth exploring, and can potentially lead to performance improvement.

Star Coupler

Although MMIs are chosen as power splitter and combiner for the transmitter, there is a star coupler test structure on the layout with edge couplers as input and output ports. As a result of some difficulties in measurement process, this test structure has not been characterized. Based on the theory proposed in [6], we were targeting $\sqrt{2}$:1:$\sqrt{2}$ power ratio in the three star coupler outputs to be utilized in the QPSK transmitter. Using Lumerical simulation, we were able to obtain 24%, 20% and 24% of power at the star coupler outputs. The simulation field profile is shown in Fig. 6.11. In addition to the three outputs needed for the transmitter structure, some dummy waveguides are also added to reduce interference and reflection. In the actual layout on the tapeout, all the dummy waveguides are terminated, and triangle shapes are added to the sidewalls to create some roughness and reduce reflection.

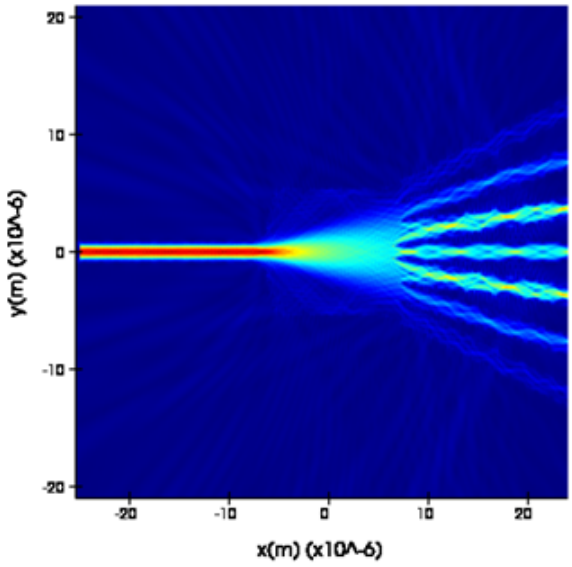

Figure 6.11: Simulation field profile of star coupler

However, from further examination of the device working principle of the QPSK transmitter, $\sqrt{2}$:1:$\sqrt{2}$ should have been the amplitude ratio, and the power ratio of the

outputs should have been 2:1:2. For this reason, we need to characterize the existing test structure to verify our simulation and design procedure; then in future tapeouts, we need to come up with star coupler designs which have power ratio closer to the theoretical value, and have the majority of the power concentrated in the three center outputs.

Bibliography

[1] C.-F. Liao and S.-I. Liu, *40 gb/s transimpedance-agc amplifier and cdr circuit for broadband data receivers in 90 nm cmos*, *IEEE Journal of Solid-State Circuits* **43** (2008), no. 3 642–655.

[2] N. Ben-Hamida, J. Sitch, P. Flemke, D. Pollex, P. Schvan, Y. Greshishchev, S.-C. Wang, and C. Falt, *Clock recovery for a 40 gb/s qpsk optical receiver*, in *2009 16th IEEE International Conference on Electronics, Circuits and Systems - (ICECS 2009)*, pp. 695–698, 2009.

[3] K. Kikuchi, *Fundamentals of coherent optical fiber communications*, *Journal of Lightwave Technology* **34** (2016), no. 1 157–179.

[4] J. K. Perin, A. Shastri, and J. M. Kahn, *Design of low-power dsp-free coherent receivers for data center links*, *Journal of Lightwave Technology* **35** (2017), no. 21 4650–4662.

[5] T. Hirokawa, S. Pinna, N. Hosseinzadeh, A. Maharry, H. Andrade, J. Liu, T. Meissner, S. Misak, G. Movaghar, L. A. Valenzuela, Y. Xia, S. Bhat, F. Gambini, J. Klamkin, A. A. M. Saleh, L. Coldren, J. F. Buckwalter, and C. L. Schow, *Analog coherent detection for energy efficient intra-data center links at 200 gbps per wavelength*, *Journal of Lightwave Technology* **39** (2021), no. 2 520–531.

[6] C. R. Doerr, L. Zhang, P. J. Winzer, J. H. Sinsky, A. L. Adamiecki, N. J. Sauer, and G. Raybon, *Compact high-speed inp dqpsk modulator*, *IEEE Photonics Technology Letters* **19** (2007), no. 15 1184–1186.